Solid Interfaces in Lithium Ion Batteries

Submitted in partial fulfillment of the requirements for

the degree of

Doctor of Philosophy

in

Mechanical Engineering

Victor Venturi

Bachelor of Science, Mechanical Engineering, Computer Science (Minor), Aerospace Engineering (Minor),
California Institute of Technology
Master of Science, Mechanical Engineering,
Carnegie Mellon University

Committee
Prof. Venkat Viswanathan, Carnegie Mellon University (Chair)
Prof. Shawn Litster, Carnegie Mellon University
Prof. Amit Acharya, Carnegie Mellon University
Prof. Donald Siegel, University of Texas at Austin

Carnegie Mellon University
Pittsburgh, PA
July 2022

Doctoral Committee
Prof. Venkat Viswanathan, Carnegie Mellon University (Chair)
Prof. Shawn Litster, Carnegie Mellon University
Prof. Amit Acharya, Carnegie Mellon University
Prof. Donald Siegel, University of Texas at Austin

Acknowledgments

The journey to and through a PhD program is not one to be tackled alone, as it is filled with challenges and hardships far too taxing for a single individual. I have been fortunate enough to have been graced with the best of company in my adventures, and this section is dedicated to some of those who have played more critical roles in shaping the scientist I am today. Firstly, I would like to thank God not only for giving me life, health, and wisdom — without which none of my achievements would have been possible, — but also for helping me see clearer when I felt surrounded by darkness, and for placing all these wonderful people in my path.

I am deeply indebted to my advisor, Prof. Venkatasubramanian Viswanathan, for trusting in my technical skills and for promoting unbounded intellectual freedom during my graduate career. I am honored to have been part of his group and to have been given such an incredible opportunity to conduct research under his guidance.

Additionally, I would like to express my gratitude to my thesis committee members, Prof. Shawn Litster, Prof. Amit Acharya, and Prof. Donald Siegel, for their valuable feedback on my work. I would also like to thank all my professors at Carnegie Mellon University, especially Prof. Alan McGaughey, Prof. Johnathan Malen, and Prof. David Laughlin, whose lectures always further stimulated my curiosity for materials sciences, as well as Prof. Reeja Jayan, Prof. Rahul Panat, and Prof. Paul Steif for helping me better contextualize the implications of my research in the beginning of my graduate education. Moreover, I would like to recognize the invaluable work done by Christopher Hertz and by the administration of the CMU Mechanical Engineering Department in creating an academic environment that nourishes interdisciplinary scientific discussions.

I have had the immense pleasure of working alongside talented collaborators, among which are Dr. Brett Helms, Dr. Peter Frischmann, Dr. Chengyin Fu, Dr. Jinsoo Kim, Dr. Chaochao Dun, Prof. Nagaphani Aetukuri, and Dr. Vikalp Raj. I would also like to acknowledge support from the Advanced Research Projects Agency-Energy (ARPA-E) through Grant DE-AR000077 and from the Richard King Mellon Foundation through a Presidential Fellowship in Energy at Carnegie Mellon University. I am grateful to the Extreme Science and Engineering Discovery Environment (XSEDE), supported by National Science Foundation Grant OCI-105357, for their tireless support and maintenance of the Bridges computer systems, hosted at the Pittsburgh Supercomputing Center (PSC).

I would also like to thank the Hirama family — Marlene, Morio, and Rafael Daigo — for their everlasting friendship and for their support in helping me realize my full potential as a student. Similarly, I am indebted to all the teachers I have had throughout my life, especially Edmilson Motta, Ivan Souza (*in memoriam*), and Pablo Ganassim, for always motivating me to never shy away from challenges, but to calmly and confidently face them. My sincere thanks also go to the staff and faculty of the California Institute of Technology (Caltech), my undergraduate institution, notably Prof. Austin Minnich, Prof.

Michael Mello, Prof. Guillaume Blanquart, and Prof. Melany Hunt, for continuously encouraging me to broaden my horizons and for serving as inspiration for my scientific undertakings.

I am extremely lucky to have made so many friends whose support helped me bear all the adversities of this arduous journey. In particular, I would like to thank Federico Presutti, Ross Koval, Julian Thomassie, Cauê Borlina, Matt Lim, Keegan Mendonca, Matt Edwards, Sid Murching, Bogdan Dimitriu, Kshit Grover, Connor Crowley, Carlos Gonzalez, Kim Liu, Chris McCarren, Kai Kirk, Harrison Jacobs, Gurjyot Sethi, Matthew Ho, Samuel Foley, Nishchay Suri, and Alejandro Sanchez. I would also like to highlight past and present group mates, who always assisted me in organizing and presenting my research results through in-depth discussions: Prof. Zijian Hong, Dr. Lei Zhang, Dr. Pinwen Guan, Dr. Emil Annavelink, Dr. Valentin Sulzer, Prof. Dong Zhang, Dr. Oleg Sapunkov, Dr. Dilip Krishnamurthy, Dr. Olga Vinogradova, Dr. Yumin Zhang, Dr. Shashank Sripad, Dr. Matthew Guttenberg, Vaidish Sumaria, Alec Bills, Varun Shankar, Venkatesh Krishnamurthy, Keith Puthi, Lance Kavalsky, Shang Zhu, Hongyi Lin, Archie Mingze Yao, Kian Pu, Lydia Tsiverioti, Alex Wadell, and Vedant Puri. Besides them, I am also extremely grateful to those friends whose invaluable insight has directly impacted the contents of this work: Prof. Zeeshan Ahmad, Prof. Rachel Kurchin, Holden Parks, Prof. Abhishek Khetan, Dr. Hasnain Hafiz, Dr. Vikram Pande, Dr. Gregory Houchins, Adarsh Dave, and Mohammad Babar.

Words cannot express my gratitude to the Carnahan family — Jim, Cathy, James, Terry, Marie-Andrée, and Janelle — who welcomed me into their family as one of their own, and who have helped me feel more at ease in a foreign land.

I could not have undertaken this journey without the boundless love and support of my fiancée, Caitlin Carnahan. During all these years, you have kept me sane and grounded more often than you think. Thank you for accompanying me in this crazy roller-coaster ride, for being by my side when I needed a shoulder to cry on, for commemorating my achievements even more than me, and for being such a thoughtful, caring, and loving partner. Every day, I feel blessed to have you in my life. Eu amo muito você!

Finally, this endeavor would not have been possible without generations of unconditional love, hard-work, and sacrifices made by my family, to whom I dedicate this Thesis. I hope my paternal grandparents, who I lovingly call *Nonno* and *Nonna*, are proudly watching me from the Heavens and feeling all the love and appreciation I have for everything they have done for me, from teaching me to enjoy both arts and sciences to laying the foundations and principles of my moral compass. I am also eternally thankful for my parents, whose love and support permeates every aspect of my life, and without whom this dream would have never become a reality. To my Mãe, thank you for being patient with me even when I did not deserve it, and for comforting me when failures knocked at my door. To my Pai, thank you for never hesitating in investing in my education, and for your tireless work in helping me navigate the tortuous paths that led me to where I am today. *Nonno* e *Nonna*, Pai e Mãe, eu amo muito vocês. É a vocês que dedico esta Tese.

Abstract

It is difficult to imagine modern life without batteries: they are present in our mobile phones, laptop computers, automotive vehicles, and even more vital devices, such as pacemakers. Most of these gadgets are powered by lithium (Li) ion batteries, in part due to their high voltage window and relative longevity. While this technology has had major successes, at the current rate of progress, it is unlikely to meet the mid-century global demands related to full de-carbonization and interruption of use of fossil fuels for transportation and energy generation. The replacement of currently used anodes by Li metal is one of the most promising puzzle pieces involved in the solution to this problem. However, a myriad of obstacles hinders its commercialization, many of which are related to phenomena happening at the interface between the anode and the electrolyte.

In this thesis, some of the interfaces present in Li-ion and Li-metal batteries are explored. From a purely mathematical standpoint, interfaces are simply two-dimensional (2D) constructs. However, in real materials, their properties are determined by the atomic structure in their vicinity, thus making them more akin to 2.5D systems. Given the high complexity of such interfacial structures, this thesis is organized in a bottom-up approach. First, we study the possibility of using twisted bilayer graphene, a novel material that, similar to interfaces, can be described as being 2.5D, for electrochemical applications, including Li-ion technologies. Next, some of the interface-related issues that plague Li-ion and Li-metal batteries are scrutinized. Among them, this work focuses on the formation and growth of dendrites, on the ionic conductivity of components of the solid electrolyte interphase (SEI), and on the development of surface voids and pits during the discharge process. Using a well-established electrodeposition model for solid electrolytes, a carefully engineered polymer composite separator is conceptualized to harness advantageous properties of its components at the interfaces between these materials. Battery cells with this composite are tested and revealed to fully prevent dendrite growth. The synergistic interaction between two of the most common SEI components is also probed, and the interface between them is shown to significantly enhance the conduction of charge carriers, thus opening pathways for further engineering of the SEI. By combining first-principles methods with thermodynamic modeling, the importance of considering explicit interfaces in *ab-initio* calculations is highlighted in the context of void and pit formation. Excellent agreement between our modeling techniques and experimental results was achieved in all-solid-state symmetric cells containing interlayer materials. We also investigate the importance of current collector selection for ensuring high-power outage from anode free batteries at low values of state-of-charge. Finally, the impacts that halogen doping can have on surface energy and particle shape of a promising material for alkaline batteries is inspected, and the effect that dopant choice and concentration can have on unstable decomposition is elucidated.

Contents

Acknowledgments iv

Abstract vii

List of Tables xii

List of Figures xiii

1 Introduction 1

1.1 Lithium Ion and Lithium Metal Batteries 2
1.2 Electrolytes in Lithium Ion Batteries 4
1.2.1 Electrolyte Classification 4
Organic Liquid Electrolytes 4
Inorganic Solid Electrolytes 4
Organic Solid Electrolytes (Polymers) 5
1.2.2 Electrolyte Decomposition 5
1.3 The Role of Interfaces 6

2 Lithium Intercalation in Bilayer Graphene 7

2.1 Thermodynamic Modeling 8
2.2 Intercalation Behavior 11
2.3 Summary and Conclusions 15

3 Impact of Interfaces on Ionic Mobility 16

3.1 Enabling Li-metal Anodes Via Electrolyte Engineering 17
3.1.1 Electrodeposition Modeling and Separator Design 17
3.1.2 Computational Chemomechanical Characterization of LiF@PIM Composite 18
Shear Modulus Calculation 18

Hopping Energy Barrier and Molar Volume Calculations . . . 19
3.1.3 LESA Performance . . . 21
3.2 Exploring the Role of Interfaces in Diffusion Dynamics . . . 22
3.2.1 Defect Formation Mechanism . . . 22
3.2.2 Dynamics of Interstitial Li-ion Motion . . . 23
3.3 Summary and Conclusions . . . 25

4 Thermodynamics of Void Formation 27
4.1 Need for a Fundamental Understanding of Void Formation . . . 27
4.1.1 Modeling Vacancy Solubility . . . 29
4.1.2 Void Behavior for Isolated Lithium Slabs . . . 33
4.1.3 Effects of Interfaces on Void Formation . . . 35
Li/SEI Interfaces . . . 35
Li/Interlayer Interfaces . . . 42
4.2 Summary and Conclusions . . . 46

5 Tuning of Reactions through Interface Design 47
5.1 Investigating Reaction Rates at Low State-of-Charge Anode-free Li-metal Batteries . . . 47
5.1.1 Modeling Electron Transfer Kinetics . . . 48
5.1.2 Computational Screening of Current Collectors . . . 49
5.2 Empowering Aqueous Alkaline Batteries Through Interface Design . . . 55
5.3 Summary and Conclusions . . . 57

6 Conclusion and Outlook 58
6.1 The Growing Role of Machine Learning in Materials Science . . . 58
6.1.1 Common Machine Learning Applications . . . 58
6.2 The Importance of Interfaces . . . 59
6.2.1 Grain Boundaries: A Challenging Mystery . . . 59
6.2.2 Dynamics of Point Defects . . . 60
6.3 Other Low Dimensional Structures . . . 60

A List of Publications 62

B Design Rules for Two-dimensional Materials 64
B.1 Machine Learning Methods . . . 66

B.1.1 Databases 66
B.1.2 Model Training 67
B.2 Results and Discussion 68
B.2.1 Structure Screening 68
B.2.2 Identification of Design Principles 69
B.2.3 Analysis of Uncovered Design Principles 72
B.3 Summary and Conclusions 74

C CGCNN Ensemble Performance **77**

D CGCNN Optimization **81**

E Graph Convolution Description **83**

F Understanding The Basics of Density Functional Theory (DFT) **84**
F.1 Multi-body Problem Setup 84
F.2 Kohn-Sham Equations 85
F.3 Exchange Correlation Functionals 87

G Introduction to The Nudged Elastic Band (NEB) Method **89**
G.1 Minimum Energy Pathway (MEP) and Saddle Point 89
G.2 Plain Elastic Band (PEB) Method 90
G.3 NEB Origins: "nudging" of forces 91
G.3.1 Naive NEB 91
G.3.2 Improved Nudged Elastic Band 93
G.3.3 System Evolution - velocity Verlet 93
G.4 Computational Details 94
G.5 Example with Analytical Functions 95

H Lithium Electrode Sub-Assembly Details **98**

I Impacts of the Space Charge Layer **102**
I.1 Theory of Heterojunctions 103
I.2 Impact of Charged Defects 104

J Li-ion Minimum Energy Pathway at LiF-Li_2CO_3 Interface **106**

K Finite Element Poisson Solver **107**

L Computational Parameter Estimation for Regular Solution Model **108**

Bibliography **110**

List of Tables

3.1 Mechanical properties of bulk PIM calculated with computational and experimental methods. Uncertainty in Poisson's ratio originates from the different measures in both x and y directions. . 19

3.2 Surface energies of LiF and Li_2CO_3. The slabs were generated using the pymatgen surface module [95, 96, 97] and the atomic simulation environment. [98] 22

4.1 Approximate surface energies, coordination numbers, interaction parameters, and critical temperatures for different surface facets. Given the relatively small difference in surface energies, it is fair to assume all facets are equally relevant. The strongest interactions in the (100) and (110) facets have very high critical temperatures for vacancy solubility (above 1000 K), meaning that, under standard operating conditions, vacancies will tend to phase separate and begin forming voids. That is not the case for the (111) surface, where vacancies are fully solvable and, under equilibrium conditions, should be uniformly distributed on the surface. [122] 34

4.2 Summary of computed thermodynamic and kinetic parameters for Al and W ILs. [110] 43

B.1 Materials with highest five c-values. For MXenes, '*' indicates a bond between a metallic atom and a termination. For the perovskites, the site occupations have been specified for clarity. Values reported are the mean of the ensemble predictions. 70

B.2 Design principles with five highest values of ratio $P_{DP|best}/P_{DP}$. The cutoff c-values used in computing values displayed for MXenes was $c_{cut} = 0.95$, and for both inorganic and organic perovskite cases, $c_{cut} = 0.80$. 73

C.1 Metrics for uncertainty quantification of model ensembles 78

List of Figures

1.1 Schematic of a typical Li-ion battery [13]. The cathode is separated from the anode by an electrolyte. During discharge, Li ions (Li^+) move from the anode to the cathode through the electrolyte, while electrons move in the same direction via the external circuit. During charging, Li ions move from the cathode to the anode through the electrolyte, with electrons moving in the same direction through the external circuit. 2

1.2 Diagram of issues associated with the use of Li metal anode with liquid electrolytes. [17] 4

1.3 Mosaid model of the SEI proposed by Peled et al. [49] The most common inorganic products of the electrolyte decomposition reactions are Li_2O, LiF, and Li_2CO_3 5

1.4 Summary of the various failure mechanisms that can occur in an inorganic-based all-solid-state Li metal battery (ASSLMB). [51] 6

2.1 Fit used for determining radius of AA regions as a function of bilayer twist angle. 10

2.2 AA prevalence as a function of twist angle. 10

2.3 **(a)** Contour plot of Δg with respect to total lithium loading x and lithium concentration in AA regions x_A at 300K for a twist angle of 1.1°. Notably, for total lithium concentrations greater than $x \approx 0.23$, no further intercalation can take place, and lithium plating starts happening. The optimal loadings in the AA and AB regions as a function of total loading x are shown in panels **(b)** and **(c)**, respectively. The red dots indicate the load distribution that corresponds to the global minimum of Δg. At a 0° twist angle, the structure is fully AA, and, thus, no intercalation can take place in AB. Since intercalation in AA is more favorable than in AB, this regime reaches the theoretical maximum total load of ~ 0.65. At different twist angles, the global minimum in Δg is achieved by keeping $x_A \sim 0.65$ and $x_B \sim 0.20$. 12

2.4 Maximum value of total lithium loading as a function of twist angle for temperatures ranging between 200 and 500 K. Note that, at twist angle of 0°, the twisted bilayer structure becomes fully AA, in which case the large enthalpic contributions enable a full loading of $x_{\mathrm{max}} \sim 0.65$. The temperature dependence of x_{max} is only appreciable for lower twist angles, for which the bilayer stacking is mostly AB, a regime where entropic and enthalpic contributions to Gibbs free energy are of the same order of magnitude. 12

2.5 Minimum value of $\Delta g(x)$ for different twist angles. While for all angles smaller than 2.5°, full intercalation is unstable against lithium plating, overpotentials smaller than 0.05 eV per lithium atom can nearly double the amount of intercalated lithium from the global minimum in Δg. . . 13

2.6 Voltage profile during lithium intercalation at a temperature of 300 K of twisted bilayer structures for several different initial twist angles. In all cases, a voltage difference of less than 0.7 V is observed through the intercalation process. 13

2.7 Contour plot of $\log_{10}\left({}^{x_A}/_{x_B}\right)$ as a function of twist angle and total lithium concentration. Due to the absence of AB regions at a 0° angle, values for un-twisted structures were omitted. While most of the phase space is dominated by ratio values in the range between 1 and 2.5, a wide array of possible values is attainable by careful control of both the twist angle and lithium concentration. 14

3.1 Chemomechanical model underlying the successes and failures of SICs in preventing instabilities at the anode surface during electrodeposition. SICs can access either dendrite-blocking character or dendrite-suppressing character, but not both. Prototypical SICs that serve as the battery's electrolyte are labelled in each region. [8] 18

3.2 **(a)** Energy landscape of Li^+ surface diffusion on LiF and bulk transport within LiF. Insets: different stages encountered during hopping from a Li site (encircled in solid grey) to a nearby vacant site. The experimentally determined activation barrier for Li^+ hopping further takes into account the influence of PIM-1, which results in an 80 meV increase above the calculated result for the LiF surface. **(b)** Summary of vacancy diffusion barriers and ion molar volume ratios in the presence of PIM-like adsorbates in LiF. Grey circles indicate the initial (pre-hop) vacancy site. The corresponding values without such molecules are 0.34 eV for the barrier and 0.21 for the molar volume ratio. [8] 20

3.3 Rate tolerance of Li–NMC-622 cells (30-μm-thick Li anode; cathode areal capacity of $1.44\mathrm{mAh} \cdot \mathrm{cm}^{-2}$) cycled at 20°C, configured with either LiF@PIM-1 SICs (LESA 3), Celgard (negative control) or PIM-1-coated Celgard (positive control). 21

3.4 Geometry of the coherent interface between (001) LiF surface and (001) Li_2CO_3 surface used in DFT calculations. (a) Front and (b) side views along with the axes orientation. The black line is the boundary of the interfacial unit cell used in the simulations with the z axis is perpendicular to the interface. 23

3.5 Energetics of minimum energy pathway of interstitial Li motion in Li_2CO_3 layer. Interstitial Li atoms are circled by a continuous blue line, while lattice Li atoms that partake in the motion are circled by a dashed blue line. The activation energy of Li hopping is reduced from 0.3 eV in bulk Li_2CO_3 to 0.10 or 0.22 eV in the interfacial structure considered, showing that the interface assists in Li diffusion. 24

3.6 MSD for Li ions in Li_2CO_3 vs time calculated layerwise at 800 K. Layer 1 is closest to the interface while layer 4 is the farthest. The layers closer to the interface have the highest MSD. The higher value for layer 4 compared to layer 3 may be due to its exposure to vacuum. 25

4.1 Images and depictions of the formation and evolution of pits, and migration of vacancies at and near interfaces of Li metal with other materials. **(a-c)** Optical images of evolution of a pit, with surface GBs outlined in black in panel **a**. **(d-e)** Polar plots of the distance between the edges and the center of the pit at times 240s, 430s, and 730s, respectively. Panel **g** shows the average distance between vacancies and anode surface as a function of number of kinetic Monte Carlo (KMC) steps taken. The initial configurations are displayed in panels **h** for Li/Li_2O and **i** for Li/LiF, while the configuration at 10^5 KMC steps are represented in panels **k** for Li/Li_2O and **l** for Li/LiF. It is evident that vacancies in Li metal are much more likely to diffuse into bulk when Li_2O is present at the interface, instead of LiF. Panel **m** is a schematic of one of the proposed hypothesis for pit formation: as voids are formed during stripping and then occluded during plating, they can merge with other voids on subsequent stripping processes and create large pits. Panels **(a-f)** are reproduced with permission from Ref. [112], **(g-l)** from Ref. [114], and **m** from Ref. [109]. 29

4.2 Diagram of relationship between ΔG and x_A for different temperatures. At temperatures higher than T_c (red line), Δg is convex everywhere in the domain, indicating $(\partial\mu/\partial x_i) > 0$ for all values of x_A; at the critical temperature T_c (yellow line), the double derivative of Δg with respect to x_A becomes zero at $x_A = 0.5$ and represents the onset of a phase transition; for temperature values lower than T_c (turquoise and blue lines), for some values of overall x_A, two phases, one with low characteristic x_A and one with high characteristic x_A, coexist, and correspond to the two minima in the Δg curve. 32

4.3 Top-view schematic of the different possible interactions considered for the **(a)** (100), **(b)** (110), and **(c)** (111) lithium surface facets. Purple circles denote lattice sites on the outer-most surface layer, and yellow orange circles denote sites on the second outer-most layer. In the (110) case (panel **(b)**), there are several different pair-wise interactions: red-purple, red-blue, red-yellow, and red-pink. In the other two cases, all purple-purple and orange-orange site interactions are equivalent. [122] 34

4.4 Side-view schematics of the expected behavior of **(a)** (100), **(b)** (110), and **(c)** (111) lithium surface facets during stripping, respectively. These diagrams neglect kinetic barriers associated with vacancy motion, and assume that, in all cases, vacancy diffusion along the surface planes is not a limiting factor. Note that these schematics solely portray predictions from our first-principles informed regular solution model for isolated Li-slabs; to the authors' knowledge, there has been no experimental evidence for these phenomena. The removal of atoms during discharge creates vacancies on the surface, denoted by circles. Purple circles represent vacancies on the surface-level Miller plane, and orange circles are vacancies on the second outer-most layer. Red arrows show the interactions between vacancies. In the (100) facet, vacancies will attract each other regardless of layer, and can thus form large (in an atomistic scale) valleys. The (110) surface exhibits a somewhat similar behavior, but, due to the inter-layer vacancy repulsion, vacancies would only congregate on the surface-level Miller plane. By doing so, they form steps that expose the underlying layer and creates a new surface for lithium extraction. In this case, valleys would be formed as a collection of terraces. The (111) facet shows the most promise: the strong inter-layer vacancy repulsion, coupled with the weak intra-layer attraction, will force vacancies to be uniformly distributed on the surface. In doing so, when enough lithium is stripped, a relatively flat surface will emerge. The light pink rectangle in panel **(c)** enclosed by the dashed line indicates the stripped layer. [122] 35

4.5 Schematic of a Li(110)/LiF(110) interface used in DFT simulations for estimation of regular solution parameters. [122] 36

4.6 Representation of values of $\Omega^{(11)}$ along the surfaces of Li slabs at the corresponding interfaces with SEI materials. The colored circles represent the location of atoms in the SEI material, and their opacity is inversely proportional to their distance from the interface: circles that are more translucent are further from the interface, and those that are more opaque are located closer to the Li surface. Dashed black lines indicate the limits of the super cell used in the simulation. [122] 37

4.7 Distribution of values of $\Omega^{(11)}$ and $\Omega^{(12)}$ along lithium surfaces of specified interfaces. Dotted lines indicate the corresponding values for a strained, isolated Li slab. LiF seems to have little to insignificant impact on $\Omega^{(11)}$ parameter, while, at the same time, increasing the value of $\Omega^{(12)}$ at its interfaces with Li(110) and Li(111). Interestingly, Li_2CO_3 decreases the values of both Ω parameters, and, in the case of the interface with Li(110), this SEI material is capable of lowering the critical temperature for vacancy solubility to 0 K, a very promising result that indicates a potential for this interface to prevent the formation of voids on the anode surface. [122] 38

4.8 Distribution of critical temperature T_c values for the different Li-SEI interfaces considered. Values of T_c are calculated from values of Ω in Figure 4.7 according to Equation 4.7. [122] 39

4.9 Relationship between thermodynamic parameters and distance to the closest atoms in the SEI material. The corresponding values of said parameters for the isolated unstrained and strained Li slabs are shown in green and orange, respectively. Due to the atomic structure of Li_2CO_3, distances to the closest cluster of 3 oxygen atoms were also taken into account. No obvious correlation can be found, with the exception of the Li(110)/LiF(001) interface. [122] 41

4.10 Plot of $\Omega^{(11)}$ and $\Omega^{(12)}$ as a function of the negative of the adhesion energy associated with the corresponding interface. This graph shows that lower adhesion energies yield lower values of Ω, and, thus, a Li surface that is more stable against void formation. 41

4.11 Comparison of j_c at temperatures of 25°C, 40°C, 60°C, and 70°C for cells with Al and W interlayers. [110] 43

4.12 Cross-sectional SEM images of symmetric cells with Al and W interlayers. In all images, the bottom, rock-like portion, is the solid electolyte (LLZTO), and the top material is the anode. Cells prior to cycling (as-prepared pristine) and those cycled at current densities of $^{j_c}/_3$ (of the respective IL) exhibit interfaces where the surfaces of anode and electrolyte are flush with each other. At current densities of $^{2j_c}/_3$, regions where the two materials are not in contact can be seen (black regions), indicating the existence of voids. For cells that were cycled until a short-circuit was detected, the interface is notably composed of large voids and dendritic structures. [110] . . 44

4.13 Al and W slabs used for computational calculations. Li monolayers on (100) surface facets of Al **(a, b)** and W **(c, d)**. Top views are shown in panels **(a)** and **(c)**, and side views are in panels **(b)** and **(d)**. 44

4.14 Wulff constructions of Al and W. In Al, nearly 70% of the surfaces are composed of (111) facets, while only 4% are composed of the desirable (110) facets. For W, however, nearly 80% of surfaces are (110) facets. 45

5.1 Schematic of structures used in DFT calculations of anode-free interfaces. Red circles denote current collector atoms, and blue circles correspond to Li atoms. In particular, the interfaces in this image represent lithium growth along the Li(100) direction on a Mo(111) substrate. 49

5.2 Representation of the PDOS from V(110)/Li(100) interface structure. Grey lines correspond to the PDOS of atoms on the top 2.5Å of the system. Dashed colored lines are the summation of the PDOS of Li atoms, and continuous colored lines are the summation of the PDOS of the CC atoms (V). Red lines correspond to the bare CC system, yellow, to that with a single Li monolayer, green, to a system with 2 Li layers, teal, to one with 3 Li layers, and blue, to one with 4 Li layers. 50

5.3 Ratio of $k_{net}^{\dagger}$ values calculated considering the PDOS of the top 2.5Å atoms and the summation of all PDOS for the V(110)/Li(100) interface. 51

5.4 Variation of $k_{net}^{\dagger}$ with overpotential for a Mo(110)/Li(110) interface. 51

5.5 Ratio $k_{net}^{\dagger}[\text{current system}]/k_{net}^{\dagger}[\text{4 Li layers}]$ for a V(110)/Li(110) interface. Due to the abundance of V states, the bare CC and Li monolayer curves are above that for a structure with 4 Li layers. In this case, there is not much variation between structures with 2, 3, or 4 Li layers. 52

5.6 Results for a Cu(100)/Li(100) interfacial system. **(a)** Ratio of $k_{net}^{\dagger}$ as a function of overpotential. **(b)** Sum of relevant PDOS near the Fermi level for structures with different numbers of Li layers. The relatively low PDOS for a bare Cu(100) facet is responsible for a decrease of $k_{net}^{\dagger}$ as de-lithiation occurs. 52

5.7 Distribution of $k_{net}^{\dagger}$ ratios compared to adsorption energy Δg_{ads} for several of the interfaces considered, for negative and positive values of the overpotential η. Positive η denotes a reaction dominated by oxidation, while negative η corresponds to a reduction-dominated reaction. 54

5.8 Schematic illustration for **(a)** the traditional and **(b)** the new-concept electrodes 55

5.9 Calculated surface energies of $NiF_x(OH)_{2-x}$ for the (001), (100), and (110) facets. 56

5.10 Decomposition enthalpies for halogen doped β-Ni(OH)$_2$ Low doping ratios correspond to $x = 1/12$, and high ratios correspond to $x = 2/3$. Units of ΔH reported in eV per Ni atom involved in the decomposition reaction. 56

B.1 Illustration of 2D materials applications: (a) 2D perovskites whose bandgaps can be the range of 1.5-3 eV have been demonstrating promise in the field of photovoltaics, ; (b) MXenes can be used in composites to increase their mechanical strength, here indicated by the material's response to an external mechanical stress (in grey). [141] 65

B.2 A simple representation of the CGCNN architecture. The atomic structure is first converted into its crystal graph representation. This graph is then passed as input for the convolutional layers, where the atomic feature vectors are updated based on neighbor information and bond lengths. Next, a pooling function is employed to produce an overall vector representation of the crystal, guaranteeing invariance with respect to number of primitive unit cells used in the creation of the original structure. Finally, a set of fully connected hidden layers maps the simplified vector-represented crystal structure to the property of interest. 67

B.3 Comparison of predicted and DFT-calculated (a) $\log(c_{11})$, (b) $\log(c_{11})$, (c) H_{form}, and (d) band gap on C2DB data. The predictions are made using an ensemble of 100 CGCNN models, each trained on randomly selected training data. 69

B.4 One of the top design principles for MXenes: hafnium (Hf) bonded with oxygen (O) termination, and with a fluorine (F) termination bonded to any other metal. The likelihood that any arbitrary model predicts that a random material satisfying this DP is a useful candidate is of $\sim 57\%$, as indicated by c_{DP}. Choosing $c_{cut} = 1.0$ shows that the chance of a structure satisfying the DP being among the best candidates is of nearly $c_{chanceDP} = P_{best|DP} \sim 20\%$, and these candiates contribute to approximately 30% of c_{DP}, as shown by $c_{contribDP}$. Note that, for this specific DP, $P_{DP|best}$ almost steadily increase with the value of c_{cut}, indicating that, the more confident we want to be in our set of useful candidates, in general, the more prevalent this DP becomes in this $\mathcal{B}$ set. 73

B.5 One of the top design principles for inorganic perovskites: A-site occupied by hafnium (Hf), with vanadium (V) in the B-site. The likelihood that any arbitrary model predicts a random material satisfying this DP is a useful candidate is of $\sim 29\%$, as indicated by c_{DP}. Choosing $c_{cut} = 0.80$ shows that the chance of a structure from set $\mathcal{D}_{DP}$ to be among the best candidates is of $c_{chanceDP} = P_{best|DP} = 14\%$, and these candidates contribute to approximately 50% of c_{DP}, as shown by $c_{contribDP}$. Additionally, for this specific DP, $P_{DP|best}$ almost steadily increases with the value of c_{cut}, indicating that, the more confident we want to be in our set of useful candidates, in general, the more prevalent this DP becomes in this $\mathcal{B}$ set. Finally, an examination of the behavior of c_{best} reveals that, for values of the cutoff $c_{cut} > 0.6$, all of the structures in set $\mathcal{B} \cap \mathcal{D}_{DP}$ have a c-value of nearly 1.0. 74

B.6 Top design principle for Khazana perovskites: A-site occupied by formamidinium ($HC(NH_2)_2$), with fluorine (F) in all X-sites. The likelihood that any arbitrary model predicts a random material satisfying this DP is a useful candidate is of $\sim$ 82%, as indicated by c_{DP}. Choosing $c_{cut} = 0.80$ shows that the chance of a structure from set $\mathcal{D}_{DP}$ to be among the best candidates is of $c_{chanceDP} = P_{best|DP} =\sim 65\%$, and these candidates contribute to approximately $\sim$ 70% of c_{DP}, as shown by $c_{contribDP}$. . . . 75

B.7 Summary of uncovered design rules for: (a) MXenes, where hafnium (Hf), zirconium (Zr), or titanium (Ti) must be bonded to an oxygen termination, regardless of the central X component or the metal M2 on the opposite side of the structure, which should have either an oxygen or a fluorine termination; (b) inorganic perovskites, in which the A-site must be occupied by scandium (Sc), zirconium (Zr), or hafnium (Hf), the B-site has to contain chromium (Cr), scandium (Sc), niobium (Nb), or vanadium (V), and, as discussed in the main text, all X-sites should be occupied by oxygen; (c) organic-inorganic hybrid perovskites, where all X-sites must be occupied by fluorine, the B-site can be occupied by either tin (Sn) or lead (Pb), and the A-site possibilities are formamidinium ($HC(NH_2)_2$), imidazolium ($C_3H_5N_2$), and azetidinium (C_3H_8N). Note: in the inorganic perovskite case, even though all X-site occupations should be the same, we represented them by different colors for completeness, since changing the value of c_{cut} used in the analysis allows for other possibilities where all three distinct types of X-sites can be populated by a different atom. . . . 76

C.1 Calibration plot [179, 180] of CGCNN ensemble CBM prediction. In general, the ensemble of model predictions captures the true values of CBM within one standard deviation. . . . 78

C.2 Histograms of errors on band gap prediction and of standard deviation of ensemble predictions. . 79

C.3 Distribution of C2DB structures by prototype for $\log(c_{11})$. All prototypes whose total representation accounts for less than 5% of the entire C2DB dataset are binned together under the label “Other”. . . . 80

C.4 Percentage of $\log(c_{11})$ outliers by prototype. For most mechanical properties, FeSe is the prototype with highest ratio of outliers. . . . 80

D.1 Mean square error (MAE) of H_{form} predictions during training for learning rates of (a) 0.1, (b) 0.01, (c) 0.001, and (d) 0.0001. The lowest errors are obtained with a learning rate of 0.01. . . . 82

D.2 Evaluation of how pooling functions, as well as number of neighbors used in convolution operations affect RMSE and MAE in $\log(c_{11})$ prediction. We also implemented higher order norm functions as pooling operators. Plots like these were used to evaluate the prediction performance of models using different number of convolution layers, hidden layers, epochs, number of neighbors used in convolution operations, pooling functions, among others. 82

G.1 Examples of corner cutting caused by PEB method when the spring constants are (a) too stiff, or (b) too soft. Since these are just toy examples, there is no meaning, nor units, associated with the axes [197]. 91

G.2 Examples of the (a) naive and (b) improved implementations of the NEB method. The new definition of $\hat{\tau}_i$ allows the NEB method to properly capture the MEP without kinks [197]. 92

G.3 The NEB method applied to a single particle diffusing on two different potential energy surfaces. The potential energy surfaces are represented with contour plots. Particle energy on the potential energy surface increases with brighter colors (e.g., yellow indicates higher energy than blue). . . . 96

H.1 Periodic image effects on activation energy of hopping on LiF surface. The NEB method is used to calculate the activation barrier along with the required number of supercells to achieve the desired Li vacancy concentrations of 4, 5, and 8%. The analysis shows that the activation energy is converged to within 10 meV at a Li vacancy concentration of 8%. 98

H.2 Probability distribution of the difference in activation energy of Li hopping between bulk and surface of LiF. The difference $\Delta E_a = E_a^{bulk} - E_a^{surf}$ is shown in a histogram corresponding to the calculation performed using an ensemble of exchange-correlation functionals. The ratio of ionic conductivity $R \approx \exp(\Delta E_a/k_B T)$ in each system at 300 K is also shown as a histogram. The values for specific exchange correlation functionals (PBE, revised PBE, and PBEsol) are marked with dashed lines. The figure shows bulk ionic conduction in LiF is insignificant compared to surface. 99

H.3 Effect of PIM-representative molecules on energy landscape of migrating Li^+ along LiF (100) surface facet. 100

H.4 Ion migration along LiF surface modeled by adsorbed $LiPF_6$. 100

H.5 Minimum energy pathways for Li^+ motion on both anion and cation-rich LiF surfaces obtained from nudged elastic band (NEB) simulations using the BEEF-vdW functional. The hopping barrier for the cation-rich system was calculated to be 0.14 ± 0.07 eV. 100

H.6 Visual representation of Bader charge isosurfaces of the cation-rich system. The total molar volume ratio calculated for this system was 0.18, placing it in the dendrite-suppressing stability regime . . . 101

I.1 Defect generation at the LiF/Li_2CO_3 interface. [93] . . . 103

J.1 Minimum energy pathway for lithium migration between two equivalent interstitial sites (stages 1 and 9) in Li_2CO_3 near its interface with LiF (red), and energy landscape for the corresponding motion in bulk Li_2CO_3 (blue). The net total Li^+ motion happens along the [010] direction. . . . 106

L.1 Top and side views of the structures used to calculate interaction parameters for the **(a)** (100), **(b)** (110), and **(c)** (111) surface facets. All structures had a minimum of 4 layers, and the bottom two layers of each structures were kept fixed to properly emulate bulk lithium. [122] . . . 108

Chapter 1

Introduction

Over the last three decades, batteries have become an essential component of daily life, from powering portable electronic devices, including mobile phones and laptop computers, to rising as the strongest contenders to replace internal combustion engines. Besides offering critical aid to the electrification of transportation, they provide further means to address climate change by enabling energy storage from intermittent renewable sources, such as solar or wind. In the last 150 years, the energy density of batteries has increased 6-fold [1], averaging an approximate 1.2% annual growth. More recently, thanks in part to heavy private and public investments in the field, this growth rate has reached values of 7-8% per year.

Despite such significant progress, at the current pace, energy storage technologies risk not being able to meet projected global demands at mid-century, a time stipulated by most nations to halt their use of fossil fuels for transportation and for energy generation. While being wide-spread and presenting several advantageous characteristics — including versatility and a large voltage window — current lithium (Li) ion battery technology is insufficient for the electrification of long-haul trucks, [2] vertical take-off and landing (eVTOL) aircraft, [3] and regional and narrow-body aircraft, [4, 5] all of which require a much higher specific energy, longer cycle lives, and lower costs. The use of lithium metal anodes is generally regarded as the most promising alternative to meet these targets, [6, 7, 8] but its commercialization remains impractical due to several technical hurdles, such as interfacial instability, limited Coulombic efficiency, and uncontrollable growth of dendrites and pits. Many of these issues stem from the myriad of processes that can take place at interfaces between different materials, especially at the anode surface and its vicinity. [9, 10, 11, 12] This Chapter summarizes the fundamentals of Li-ion and Li metal batteries, as well as some of their main components and limitations.

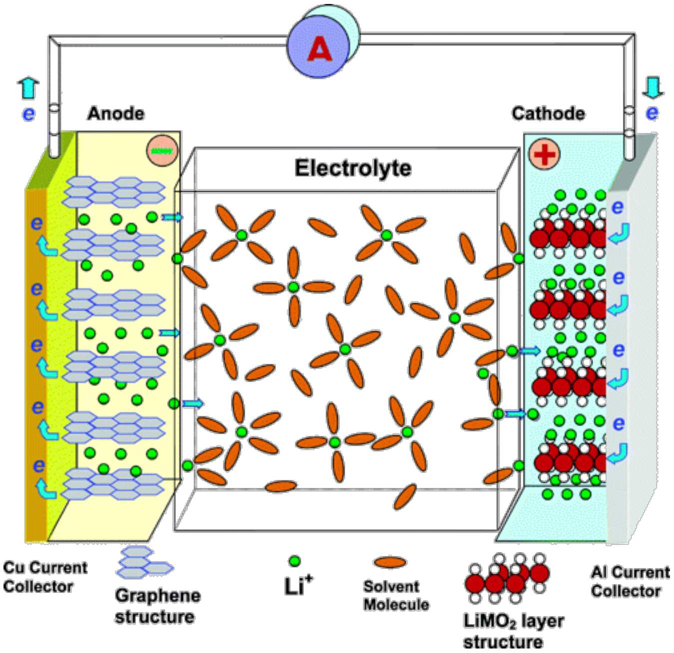

Figure 1.1: Schematic of a typical Li-ion battery [13]. The cathode is separated from the anode by an electrolyte. During discharge, Li ions (Li^+) move from the anode to the cathode through the electrolyte, while electrons move in the same direction via the external circuit. During charging, Li ions move from the cathode to the anode through the electrolyte, with electrons moving in the same direction through the external circuit.

1.1 Lithium Ion and Lithium Metal Batteries

Lithium ion (Li-ion) batteries consist of three main components: a positive electrode (cathode), usually a lithiated transition metal oxide, such as $LiCoO_2$ or $LiMnO_2$, a negative electrode (anode), commonly graphite, and and lithium-conducting electrolyte, which in most commercial applications consists of an organic liquid solution. A diagram of a typical Li-ion battery is shown in Figure 1.1. [13]

During operation, Li ions (Li^+) move from one electrode to the other via the electrolyte, while electrons go in the same direction, but through an external circuit. This direction of motion is from the anode to the cathode during discharge, and reversed during charging. Using a graphite anode as an example, the overall reactions occurring are:

$$x\mathrm{Li}^+ + x\mathrm{e}^- + \mathrm{Li}_{1-x}\mathrm{MO}_2 \rightleftharpoons \mathrm{LiMO}_2 \tag{1.1}$$

$$\mathrm{Li}_x\mathrm{C}_6 \rightleftharpoons x\mathrm{Li}^+ + x\mathrm{e}^- + \mathrm{C}_6, \tag{1.2}$$

where M indicates a transition metal and $0 \leq x \leq 1$. While discharging, x continuously decreases, and, while charging, the opposite happens.

Commercially employed Li-ion batteries have a gravimetric energy density of 250 Wh/kg and a volumetric energy density of 650 Wh/L, [14, 15] with a cycle life of around 1000 cycles. Current targets for electrification of transportation established by the United States Department of Energy are of batteries with 500 Wh/kg and 800 Wh/L for gravimetric and volumetric energy density respectively. While the overall energy density of Li-ion batteries has been increasing in the last few years, most of this progress is due to the development of high voltage cathodes, such as layered $\mathrm{Li\,Ni}_x\,\mathrm{Mn}_y\,\mathrm{Co}_z\,\mathrm{O}_2$ (NMC), which tend to present issues associated with electrolyte degradation, poor ionic and electronic conductivity, and dissolution of Ni and Mn. The anode of these new batteries, however, remains graphite in most cases.

Due to its advantageous properties, among which are high specific and volumetric capacity (372 mAh/g and 719 Ah/L respectively), good thermal stability, low irreversible capacity, low cost, high Coulombic efficiency, and low volume expansion during operation, graphite has become the established anode in Li-ion batteries. However, as discussed previously, graphite-based battery technology is unlikely to meet the high demands necessary for full electrification of transportation (particularly aviation), and its substitution by Li metal anodes seems the most promising option: Li metal anodes have a specific capacity of 3860 mAh/g, the highest among anode materials, as well as the lowest negative electrochemical potential (-3.04 V vs. standard hydrogen electrode) [6, 7, 8]. While they can be used in conjunction with current transition metal cathodes, additional gains in theoretical energy density (>1000 Wh/kg) can be achieved by coupling Li metal with other cathode materials based on sulfur (Li-S) or oxygen (Li-O_2).

Among the major factors that prevent widespread adoption and commercialization of Li metal batteries with current state-of-the-art liquid electrolytes is the inherent instability of the Li metal surface during charging leading to growth of dendrites [16, 17]. During charging, Li ions from the cathode migrate towards the anode and get electrodeposited (as opposed to intercalated in the case of graphite). This electrodeposition on Li metal is generally unstable against perturbations in the metallic surface, exacerbating any unevenness on it: surface peaks evolve into large fractal-like structures called dendrites, which can grow, penetrate, or infiltrate through the electrolyte and reach the cathode, causing an internal short circuit. Additionally, growth of dendrites increases the overall surface area of metallic Li exposed to electrolyte, which leads to further electrolyte decomposition and consumption of Li inventory, thus drastically impacting the battery's Coulombic efficiency. The dendrites can also break off from the anode and stop participating in cycling, a problem known as dead Li. Another issue involves the theoretically infinite volume expansion that Li metal anodes can present, which can cause particles on the anode surface to crack and further capacity loss. These issues are represented in Figure 1.2. [17]

Some of the alternatives currently being pursued to mitigate the dendritic growth on Li metal batteries involve the design of novel additives in liquid electrolytes [18, 19, 20, 21, 22, 23, 24], surface nanostructuring [25, 26], modified charging protocols [27, 28], artificial solid electrolyte interphase or protective coatings [29, 30, 31], polymers [32, 33, 34, 8] or inorganic solid electrolytes. [8, 35, 36, 37, 38]

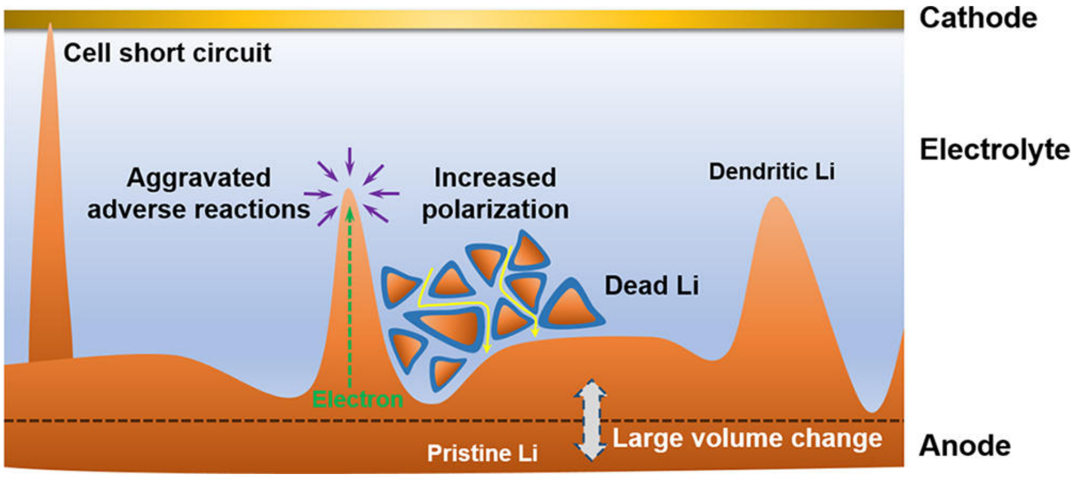

Figure 1.2: Diagram of issues associated with the use of Li metal anode with liquid electrolytes. [17]

1.2 Electrolytes in Lithium Ion Batteries

The electrolyte separates the anode from the cathode. The two main functions of an electrolyte material are transporting Li ions during battery operation, and preventing electron migration through the inside of the battery, forcing electrons to move through an external circuit. Thus, an electrolyte needs to have high ionic conductivity, while also being an electronic insulator. Besides these fundamental requirements, an electrolyte also needs to perform over a wide range of temperatures, and form a stable interface with the electrodes. Generally, electrolytes are classified into different categories, the most common ones being organic liquid electrolytes, inorganic solid electrolytes and organic solid electrolytes (polymers).

1.2.1 Electrolyte Classification

Organic Liquid Electrolytes

Usually a mixture of a carbonate, like ethylene carbonate, and a Li-based salt, such as $LiPF_6$, organic electrolytes have a high ionic conductivity and stability [13], making them the most commonly used type of electrolyte in Li-ion batteries. However, when paired with a Li metal anode, they are particular vulnerable to suffer from dendrite growth. While not the focus of this thesis, some of their decomposition products at the anode side will be discussed in Chapters 3 and 4.

Inorganic Solid Electrolytes

Unlike organic liquid electrolytes, solid electrolytes are not flammable, thus being less of a safety hazard. They also tend to have better electrochemical, mechanical, and thermal stability, allowing for longer cycle lives. [37] Their main drawback has been a subpar ionic conductivity, but, more recently, several classes of solid state superionic conductors like thiophosphates [39, 40], antiperovskites [41, 42] and garnets [43, 44] have been discovered. Solid electrolytes, due to their high mechanical strength, also present a possibility of preventing dendrite growth under certain conditions. [8, 45]

Organic Solid Electrolytes (Polymers)

Some of the most commonly studied polymers include PEO, PEG, PS, PAN, which, due to their high shear modulus, have dendrite suppressing capabilities. [46] However, similar to inorganic solid electrolytes, but to a higher extent, organic solid electrolytes suffer from poor ionic conductivity.

1.2.2 Electrolyte Decomposition

Generally, liquid and solid electrolytes tend to be unstable against the reducing potential of Li battery anodes, regardless of whether the anode material is graphite or metallic lithium. [12, 47] Therefore, upon contact with the negative electrode, electrolytes undergo redox reactions. The products of these reactions compose the solid electrolyte interphase (SEI), a non-homogenous, multicomponent, passivating thin film that prevents further electrolyte decomposition. [12, 48] The SEI is generally regarded as a "mosaic" of materials, [49] as shown in Figure 1.3. Because of its Li-ion conducting and electronically insulating nature, the SEI does not hinder normal battery operation, instead behaving akin to a solid electrolyte. Despite the irreversible capacity loss associated with its formation and the impacts it can have on critical aspects like safety, efficiency, and cycle life of battery cells, [48] the SEI remains, in the words of Dr. Martin Winter, "one of the most important, yet least understood," battery components. [50]

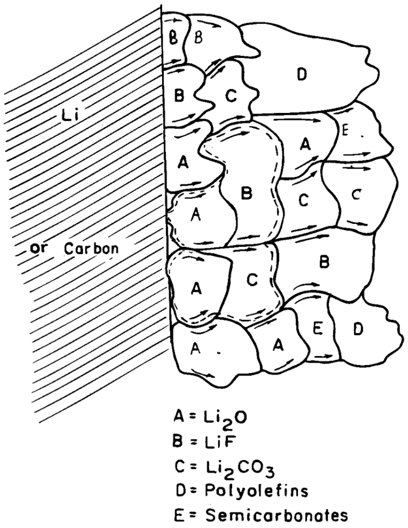

Figure 1.3: Mosaid model of the SEI proposed by Peled et al. [49] The most common inorganic products of the electrolyte decomposition reactions are Li_2O, LiF, and Li_2CO_3

1.3 The Role of Interfaces

As discussed in the previous sections, the use of Li metal anodes is paramount for achieving the demands of several critical sectors, including ground and aerial transportation. With current liquid electrolytes, the main issue plaguing the use of metallic Li as anode is the formation and growth of dendrites. Inorganic solid state electrolytes are the most promising alternative to solving this problem, but they also have shortcomings that need to be addressed, some of which are summarized in Figure 1.4 [51] and will be elaborated further in Chapters 3 and 4.

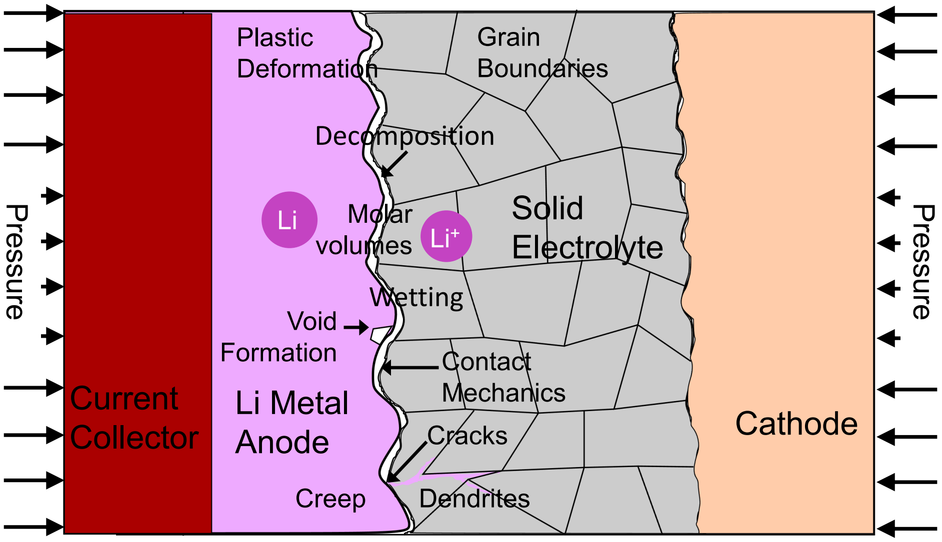

Figure 1.4: Summary of the various failure mechanisms that can occur in an inorganic-based all-solid-state Li metal battery (ASSLMB). [51]

While some of these failure mechanisms are not exclusive to all-solid-state Li metal batteries (ASSLMB), they all happen at the anode-electrolyte interface, or in its vicinity. These solid-solid interfaces are the focus of this work. Note that interfaces between three-dimensional (3D) materials are neither fully 3D nor just two-dimensional (2D), but rather something in between, colloquially referred to as 2.5D. Therefore, in order to properly understand them, this thesis examines a first-principles informed analysis of twisted bilayer graphene, a 2.5D material (Chapter 2), and then covers different interfaces in Li-ion and Li metal batteries (Chapters 3, 4, and 5). At the end, the focus is shifted to ways in which the knowledge gained in these past studies can be applied in future research projects involving solid-solid interfaces for battery technologies (Chapter 6).

Chapter 2

Lithium Intercalation in Bilayer Graphene

When atomically-thin two-dimensional (2D) layers of materials, similar to the ones covered in Appendix B, are stacked on top of one another and held together by weak van der Waals interactions, they can give rise to a slew of new properties [52, 53, 54, 55, 56, 57]. These aptly named van der Waals structures can form bulk three-dimensional (3D) structures, such as graphite, but, if the number of stacked layers is relatively small, they can be considered as 2.5D, a hybrid between 3D and 2D. Ion intercalation between the stacks of atomic-layers in van der Waals structures was one of the pioneering discoveries by M. Stanley Whittingham that enabled the rechargeable Li-ion battery revolution, [58] and granted him, John B. Goodenough, and Akira Yoshino the 2019 Nobel Prize in Chemistry.

The layers in van der Waals structures can be rotated with regards to one another and form Moiré superlattices, [59, 60, 61, 62] whose periodicity scales in an inversely proportional manner to the rotation, or twist, angle. Additional alluring properties can develop from the variation of local atomic environments present in such Moiré lattices, such as the emergence of flat bands and superconductivity in magic-angle graphene. [63, 64]

Small atoms and molecules can be employed to investigate the energy landscape of these structures. [65, 66, 67] Of particular relevance is lithium intercalation in graphene layers, given its importance in current state-of-the-art battery anodes. [68, 69] Larson et al. [70] have already probed the energetics of lithium intercalation in high-angle ($\gtrsim 2.5°$) twisted bilayer graphene. However, the large size of the Moiré unit cells at smaller angles makes the computational cost of similar first-principles investigations in these structures prohibitive, and alternative approaches are needed. In this Chapter, a thermodynamic model is developed to study intercalation in low-angle twisted bilayers, based on values obtained with first-principles predictions from DFT. It is used to evaluate the maximum lithium loading in such materials, as well as the ‘equilibrium’ voltage profile during cycling. The dependence between twist angle, total lithium concentration, and the distribution of lithium over different stacking regimes is also examined.

2.1 Thermodynamic Modeling

When two AA stacked graphene layers are twisted, they naturally undergo local strain to form low energy regions of AA and AB stacking [71]. Assuming that the twist angle is held fixed such that lithium insertion between the two layers is unlikely to induce further structural deformations, it is expected that intercalation will yield an non-uniform lithium distribution across the bilayer.

First, note that, while in lithiated graphite $\mathrm{Li}_x\mathrm{C}_6$, maximum lithium loading happens when $x = 1$, a fully loaded bilayer system will have composition LiC_{12}, or, equivalently, $\mathrm{Li}_{0.5}\mathrm{C}_6$. However, given the symmetry of the bilayer system, only one of the layers needs to be considered. In this case, the maximum loading composition would once again be LiC_6.

It is then necessary to predict what the relative lithium fractions in the AA and AB regions, x_A and x_B, respectively, would be for a given a total intercalation content of x ($\mathrm{Li}_x\mathrm{C}_6$) in a monolayer. For that purpose, suppose that each layer has a total of N carbon atoms, of which N_A are in regions of AA stacking, and N_B are regions of AB stacking. Since it is assumed that no lithium intercalation takes place in the high energy AA-to-AB and AB-to-BA transition regions, we have $N = N_A + N_B$. For simplicity, denote $\alpha = N_A/N$ the fraction of the carbon atoms that are in AA regions of the bilayer.

Let Δh_A and Δh_B be the per lithium atom intercalation energy in AA and AB regions, respectively. The reference states for this calculation are metallic lithium and a pristine twisted bilayer structure. Therefore, under the dilute limit assumption, in which the lithium atoms do not interact with each other, the values of Δh_A and Δh_B can be calculated, for each of AA and AB regions, by the following simple relation [68]:

$$x_i \Delta h_{i,\ \mathrm{intercalation}} = h_{\mathrm{Li}_{x_i}\mathrm{C}_6} - h_{\mathrm{C}_6} - x_i h_{\mathrm{Li}} \tag{2.1}$$

Owing to the negligible contributions of pressure and volume to these enthalpy values [72], they can be equated to the corresponding internal energy values, which are be obtained from DFT. The projector augmented wave (PAW) method as implemented in the GPAW [73] Python package, coupled with the Bayesian error estimation functional (BEEF-vdW) [74], which accounts for van der Waals interactions, was used to obtain the values of $\Delta h_A = -0.217$ eV and $\Delta h_B = -0.017$ eV. As expected, AA intercalation is more favorable than AB [75, 76] by approximately 0.2 eV per atom. An important consideration is that the intercalation energies in AA and AB regions were calculated under the assumption that the local environment in the neighborhood of the intercalation site is exactly equivalent to that of a un-twisted bilayer system with the corresponding stacking regime.

As stated above, these enthalpy change values are valid in the dilute case, where interaction between lithium atoms is negligible. However, as more intercalation happens, sites with lithium start to interact in an electrostatic manner. [68] Using a mean-field, regular solution based approach to account for that, the enthalpy change for an occupied site becomes

$$\Delta h_i = \Delta h_{i,\text{ intercalation}} + \frac{z}{2} x_i \Delta h_{i,\text{ interaction}}, \tag{2.2}$$

where $z = 6$ is total number of neighboring sites, x_i is the filling fraction of the region, and $\Delta h_{i,\text{ interaction}}$ is the interaction energy. The factor of 2 in the denominator comes from the assumption that the interaction energy is equally shared between occupied sites. Values of $\Delta h_{A,\text{interaction}} = \Delta h_{B,\text{interaction}} = 0.05$ eV are within an acceptable range. [68]

From this, we can calculate the total enthalpy change for a specific configuration as

$$\begin{aligned} \Delta H(x_A, x_B) &= \frac{N_A}{6} x_A \Delta h_A + \frac{N_B}{6} x_B \Delta h_B \\ \Delta H(x_A, x_B) &= \frac{N}{6}\Big[\alpha x_A \Big(\Delta h_{A,\text{intercalation}} + \frac{z}{2} x_A \Delta h_{A,\text{interaction}}\Big) + \\ &\quad + (1-\alpha) x_B \Big(\Delta h_{B,\text{intercalation}} + \frac{z}{2} x_B \Delta h_{B,\text{interaction}}\Big)\Big] \end{aligned} \tag{2.3}$$

Normalizing this enthalpy by the total number of carbon atoms in a layer N gives

$$\begin{aligned} \Delta h(x_A, x_B) &= \frac{1}{6}\Big[\alpha x_A \Big(\Delta h_{A,\text{intercalation}} + \frac{z}{2} x_A \Delta h_{A,\text{interaction}}\Big) + \\ &\quad + (1-\alpha) x_B \Big(\Delta h_{B,\text{intercalation}} + \frac{z}{2} x_B \Delta h_{B,\text{interaction}}\Big)\Big] \end{aligned} \tag{2.4}$$

Besides enthalpy, entropic contributions are also needed in order to fully account for the change in Gibbs free energy related to intercalation. Since it is assumed that no major structural change takes place upon lithiation, it is valid consider only configurational entropy, given by $S = k_B \log(\Omega)$, where k_B is the Boltzmann constant and Ω is the number of microstates. For a given pair of intercalation loadings x_A and x_B,

$$\Omega(x_A, x_B) = \binom{\frac{N_A}{6}}{\frac{N_A x_A}{6}} \times \binom{\frac{N_B}{6}}{\frac{N_B x_B}{6}} \tag{2.5}$$

Using Stirling's approximation [$\ln(N!) \approx N\ln(N) - N$], the entropy change can be rewritten as:

$$\begin{aligned} \Delta S(x_A, x_B) &= k_B \left(\log\left[\binom{\frac{N_A}{6}}{\frac{N_A x_A}{6}}\right] + \log\left[\binom{\frac{N_B}{6}}{\frac{N_B x_B}{6}}\right]\right) \\ &= -k_B \frac{N}{6}\{\alpha\,[x_A \log(x_A) + (1-x_A)\log(1-x_A)] + \\ &\qquad (1-\alpha)\,[x_B \log(x_B) + (1-x_B)\log(1-x_B)]\} \end{aligned} \tag{2.6}$$

After a simple normalization by the total number of carbon atoms in a layer $s(x_A, x_B) = S(x_A, x_B)/N$, the change in specific Gibbs free energy is simply

$$\Delta g(x_A, x_B) = \Delta h(x_A, x_B) - T\Delta s(x_A, x_B) \tag{2.7}$$

In this manner, it becomes trivial to find, for a given value of total lithium content x, what pair of values x_A and x_B minimizes Δg, under the constraint that $Nx = N_A x_A + N_B x_B$.

Applying the hyperbolic tangent based fit show in Figure 2.1 to the data from Figure 4b in Zhang and Tadmor [71] and Table 1 in Larson et al. [70], it is possible to estimate the diameter of the AA zones as a function of the initial twist angle of the structures. The distance between the centers of said regions is given by [59, 71, 77]:

$$L(\theta) = \frac{\sqrt{3}a}{2\sin(\theta/2)} \approx \frac{\sqrt{3}a}{\theta}, \tag{2.8}$$

where $a = 1.42$ Å is the graphene bond length and θ is the twist angle. Denoting the diameter of the AA regions by $d_{AA}(\theta)$, and recalling that the Moiré lattice of the twisted bilayer is hexagonal, we can obtain the fraction of the bilayer made up of AA stacking regions, shown in Figure 2.2, using

$$\alpha(\theta) = \frac{\pi}{2\sqrt{3}} \cdot \left[\frac{d_{AA}(\theta)}{L(\theta)}\right]^2 \tag{2.9}$$

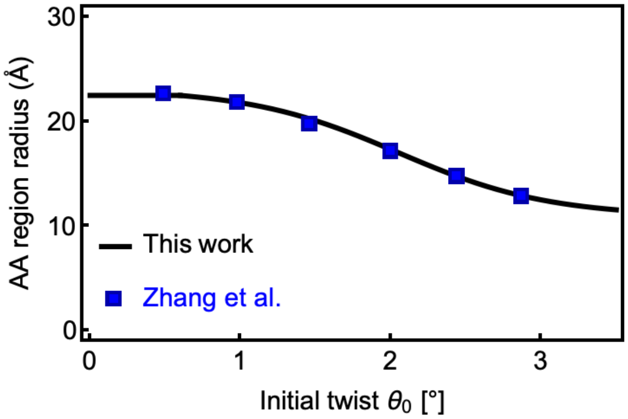

Figure 2.1: Fit used for determining radius of AA regions as a function of bilayer twist angle.

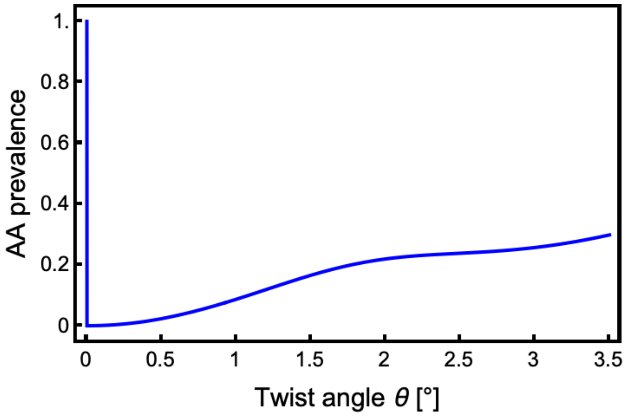

Figure 2.2: AA prevalence as a function of twist angle.

After calculating the Gibbs free energy as a function of twist angle and lithium concentration, it is possible to compute the variation in the potential profile during intercalation and deintercalation from [68]:

$$V = -\frac{\Delta G(\mathrm{Li}_{x_1}\mathrm{C}_{12}) - \Delta G(\mathrm{Li}_{x_0}\mathrm{C}_{12})}{x_1 - x_0} = -6\frac{\partial}{\partial x}(\Delta g)_{min} \tag{2.10}$$

Note that, here, a factor of 6 needs to be introduced because Δg calculated as in Equation 2.7 is normalized by the total number of carbon atoms N, while x is normalized by $N/6$. Additionally, the derivative on Equation 2.10 needs to be taken along the path that minimizes $(\Delta g)_{min}$.

2.2 Intercalation Behavior

For a twist angle of $\theta = 1.1°$ and temperature of 300 K, the contour plot of Δg is shown in Figure 2.3(a) as a function of the total lithium loading fraction, x, and the loading in the AA regions, x_A. The blue line indicates the optimal loading distribution, which minimizes the value of Δg for a given total loading x. The red dot corresponds to the global minimum of Δg: the maximum value of x which makes intercalation favorable; any attempts at further lithium intercalation without any applied overpotential will result in lithium plating rather than intercalation. Figures 2.3(b) and (c) show the optimal intercalation in AA and AB regions as a function of total lithium loading x for different values of twist angle. Note that, for a twist angle of $\theta = 0°$, the structure becomes fully AA stacked, and, thus, no intercalation can take place in AB. Additionally, since AA and AB regions are treated independently, it is clear that the values of x_A and x_B that yield a global minimum in Δg are fixed at ~ 0.65 and ~ 0.20, respectively. However, the rate at which this minimum is attained as a function of the total loading is related to the fraction of carbon atoms in AA regions, $\alpha(\theta)$, and, thus, dependent on the twist angle.

As intercalation begins, and regardless of twist angle, the AA regions of the bilayer system will always be more loaded than the AB regions, a similar prediction to that by Larson et al. [70]. This is to be expected, since $\Delta h_{A,\text{intercalation}} < \Delta h_{B,\text{intercalation}}$ and $\Delta h_{A,\text{interaction}} = \Delta h_{B,\text{interaction}}$. The maximum loading value $x_{\max}$ at which lithium plating becomes favorable, however, is strongly dependent on the twist angle, and, to a lower extent, operational temperature, as shown in Figure 2.4. This quantity is positively correlated with the ratio between the area of the AA zones and the total area of the bilayer. The temperature dependence is only significant for lower twist angles, for which most of the Moiré lattice is AB stacked. This happens because, for this stacking regime, competition between intercalation and interaction is in the same order of magnitude as entropic contributions to the Gibbs free energy.

Note, however, that the Gibbs free energy landscape around the maximum loading point is relatively flat, meaning that small overpotentials ($\lesssim 0.05$ eV per lithium atom) could effectively double the lithium content inside the double layer without inducing lithium plating, as shown in Figure 2.5. For twist angles where AA

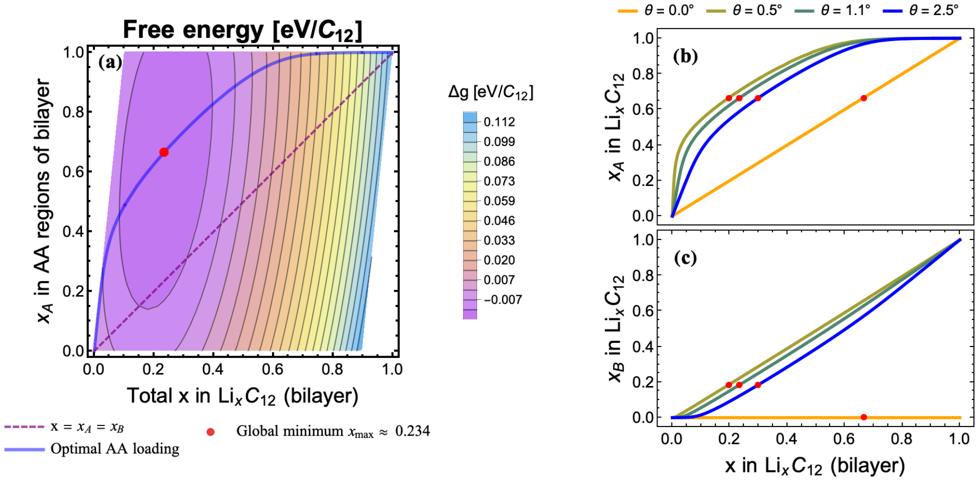

Figure 2.3: **(a)** Contour plot of Δg with respect to total lithium loading x and lithium concentration in AA regions x_A at 300K for a twist angle of 1.1°. Notably, for total lithium concentrations greater than $x \approx 0.23$, no further intercalation can take place, and lithium plating starts happening. The optimal loadings in the AA and AB regions as a function of total loading x are shown in panels **(b)** and **(c)**, respectively. The red dots indicate the load distribution that corresponds to the global minimum of Δg. At a 0° twist angle, the structure is fully AA, and, thus, no intercalation can take place in AB. Since intercalation in AA is more favorable than in AB, this regime reaches the theoretical maximum total load of ~ 0.65. At different twist angles, the global minimum in Δg is achieved by keeping $x_A \sim 0.65$ and $x_B \sim 0.20$.

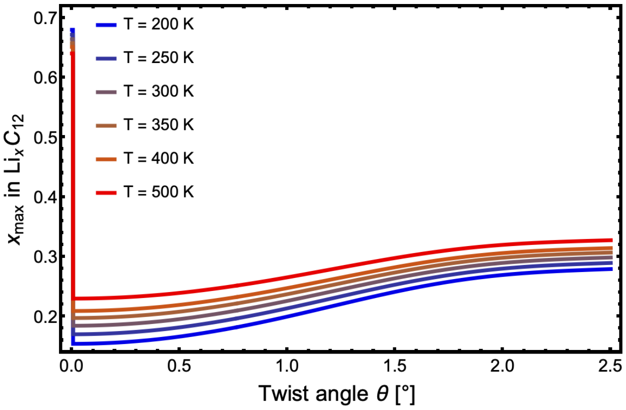

Figure 2.4: Maximum value of total lithium loading as a function of twist angle for temperatures ranging between 200 and 500 K. Note that, at twist angle of 0°, the twisted bilayer structure becomes fully AA, in which case the large enthalpic contributions enable a full loading of $x_{\max} \sim 0.65$. The temperature dependence of $x_{\max}$ is only appreciable for lower twist angles, for which the bilayer stacking is mostly AB, a regime where entropic and enthalpic contributions to Gibbs free energy are of the same order of magnitude.

prevalence is appreciable ($\alpha(\theta) \gtrsim 0.3$), such overpotentials could even lead to a fully loaded bilayer but for twist angles smaller than 2.5°, total loading is unstable against lithium plating.

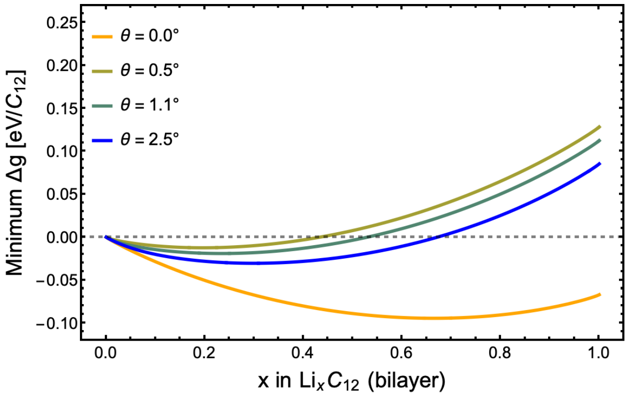

Figure 2.5: Minimum value of $\Delta g(x)$ for different twist angles. While for all angles smaller than 2.5°, full intercalation is unstable against lithium plating, overpotentials smaller than 0.05 eV per lithium atom can nearly double the amount of intercalated lithium from the global minimum in Δg.

The voltage profile during the intercalation process for different twist angles was also investigated, as shown in Figure 2.6. In the general vicinities of $x_{\max}$, where the voltage crosses the x-axis, the values of the derivative of the Gibbs free energy remain within 0.1 V of 0, an additional indication of the somewhat flat Δg landscape at its minimum. This voltage profile during intercalation in twisted bilayer structures varies slightly less than the one shown in first-principles based computational studies of standard graphite anodes, [68, 78, 79, 80] where changes of up to 1 V have been reported [68], due in part to lithium staging at different loading levels [68, 78, 79, 80]. Ignoring the spiking behavior at $x = 0$ and $x = 1$, which can be attributed to the divergence in the entropic terms in the Gibbs free energy expression, a voltage drop of no more than ~ 0.7 V is observed in twisted bilayer structures over the entire intercalation window.

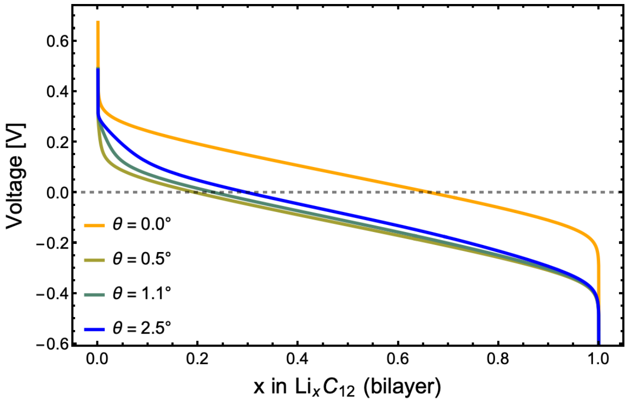

Figure 2.6: Voltage profile during lithium intercalation at a temperature of 300 K of twisted bilayer structures for several different initial twist angles. In all cases, a voltage difference of less than 0.7 V is observed through the intercalation process.

Charge transfer between lithium atoms and twisted bilayer graphene can have a significant impact on the band structure. [70] These effects can differ between AA and AB intercalation; thus, it is of paramount importance to predict the lithium distribution on these regions. Figure 2.7 shows a contour plot of the logarithm of the loadings in the AA and AB regions, $\log_{10}\left({}^{x_A}\!/_{x_B}\right)$, as a function of total lithium concentration and twist angle. Generally, the larger the twist angle, the larger the ${}^{x_A}\!/_{x_B}$ ratio. This happens because, at such angles, AA zones are more prevalent, and, therefore, AA intercalation contributes more to Δg, up to $x_A \approx 0.65$ at 300 K. At the top-left green zone in Figure 2.7, where the ${}^{x_A}\!/_{x_B}$ ratio attains a maximum, there is virtually no lithium loading in AB regions. As further lithium loading happens, the lithium repulsion in the AA regions starts to be relevant, such that entropic contributions from intercalation in AB become on par with enthalpic gains from intercalating in AA, and thus AB loading commences. This in turn lowers the value of ${}^{x_A}\!/_{x_B}$ as the total lithium loading becomes larger, but not significantly. Finally, while for the majority of lithium loading values and low twist angles, the ratio between lithium concentration remains between 1 and 2.5, Figure 2.7 demonstrates that a wide range of ratios are attainable. Thus, the pairing between total intercalation and rotation angle can provide a tuning knob for spatial control of twisted bilayer structures.

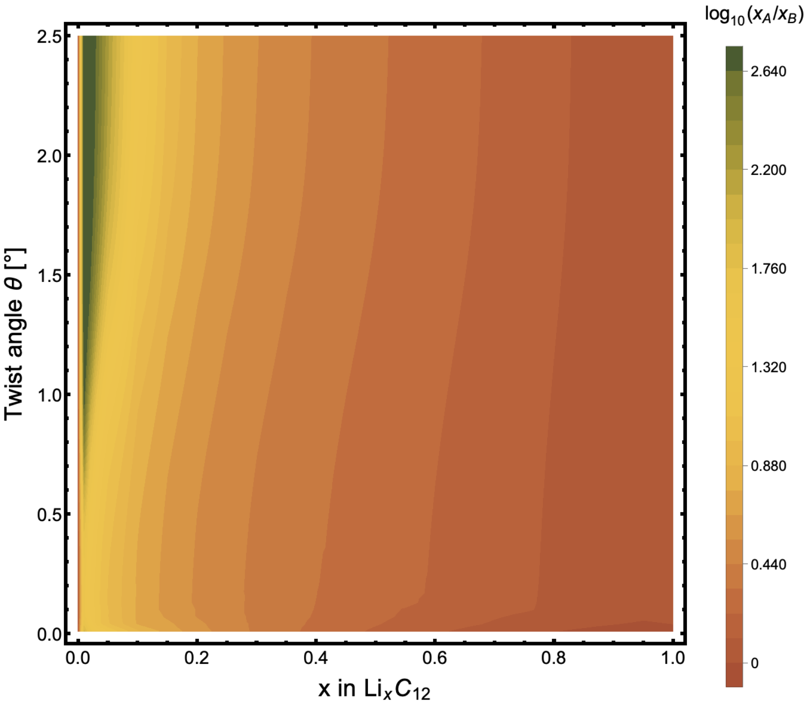

Figure 2.7: Contour plot of $\log_{10}\left({}^{x_A}\!/_{x_B}\right)$ as a function of twist angle and total lithium concentration. Due to the absence of AB regions at a 0° angle, values for un-twisted structures were omitted. While most of the phase space is dominated by ratio values in the range between 1 and 2.5, a wide array of possible values is attainable by careful control of both the twist angle and lithium concentration.

2.3 Summary and Conclusions

A first-principles informed, mean-field based thermodynamic model was developed and employed to estimate the behavior of lithium intercalation in low-angle twisted bilayer graphene. The results show that, for small-twist angles and due to strong lithium-lithium repulsion, lithium plating can begin at a relatively low theoretical maximum limit of $x_{\mathrm{max}} \approx 0.3$. However, it is also demonstrated that overpotentials of less than 0.05 eV per intercalant atom can revert this situation, and effectively double this limit. The voltage profile during intercalation/de-intercalation reveals that twisted bilayer anodes may present voltage windows slightly stabler than their standard graphite counterparts. For very low total loading x in $\mathrm{Li}_x\mathrm{C}_{12}$, lithium atoms will mostly cluster in the AA regions of the Moiré pattern. Nevertheless, repulsion between lithium atoms in this region soon becomes non-negligible, and opens a path for the onset of AB intercalation. Finally, it is shown that the twist angle and intercalation can be used as tuning knobs for control of intercalant distribution in twisted structures.

Chapter 3

Impact of Interfaces on Ionic Mobility

Not unlike what happens with graphene when two monolayers are twisted with respect to one another and form regions with distinct stacking regimes, many materials exhibit exciting new properties due to the presence of local crystalline imperfections, or defects. To name a few commonplace applications only made possible by such imperfections, transistors present in electronic gadgets and light emitting diodes (LED) in our modern television sets all rely on doping, a process that introduces point defects in a material; steel used in civil and naval engineering industries is made stronger due to the large density of (pinned) dislocations — a type of line defect — caused by martensitic phase transformations; through a similar mechanism, grain boundaries, a type of surface defect, can improve the yield stress of many metals by imposing barriers to dislocation slip.

Solid materials used in electrochemical applications are no different. Crystal imperfections can significantly aid the use of solid electrolytes in batteries, such as in the case of inorganic solid ion conductors (SIC), where vacancies and interstitial sites are the major Li-ion carriers. However, these defects, especially interfaces, can also have major drawbacks, as exemplified in Figure 1.4. Due to the relative infancy of the field, solutions that allow using these defects exclusively to our advantage are still under active investigation. For comparison, steel was first created in 1800 B.C. [81], but steel production only began to be perfected in the middle ages, [81] after nearly three millennia of trial and error; one of the first batteries in history was invented by Alessandro Volta in 1799, just over two centuries ago, and batteries are already a highly-efficient, critical component of our society. The following three Chapters cover examples of how modern advanced approaches, such as thermodynamic modeling and first-principles density functional theory (DFT), are used to continue facilitating such rapid progress.

3.1 Enabling Li-metal Anodes Via Electrolyte Engineering

As discussed in Chapter 1, the use of Li-metal anodes is a promising solution to increase the energy density of batteries. However, morphological instabilities at the anode-eletrolyte interface generated by electrodeposition, the main process that occurs during charging, constitute a major safety concern. Recent studies [82, 83, 45] show that solid electrolytes can offer a potential avenue for solving this issue.

3.1.1 Electrodeposition Modeling and Separator Design

The work by Monroe and Newman [82, 83] indicates that solid ion conductors with high enough shear modulus can block dendrite growth. Yet, this prediction has had limited success, as dendrite formation and growth remains an open problem in Li-metal batteries: ceramic materials with sufficient shear modulus, single-crystal glass electrolytes, and even soft separators fail to stop dendrite penetration. A recent study by Ahmad and Viswanathan [45] offers an explanation. The morphological evolution of the metallic surface is directly related to the charge density at the anode-electrolyte interfaces. This current density can be described with the Butler-Volmer model: [83]

$$\frac{i_{\text{deformed}}}{i_{\text{undeformed}}} = \exp\left(\frac{(1-\alpha)\Delta\mu_{e^-}}{RT}\right), \tag{3.1}$$

where i is the current density at either a deformed on undeformed surface, α is the anodic charge transfer coefficient, R is the universal gas constant, T is the temperature, and $\Delta\mu_{e^-}$ is the change in electrochemical potential of the electron due to the surface deformation, which is governed by interfacial tension (γ) and deviatoric (τ) and hydrostatic (p) stresses: [45]

$$\Delta\mu_{e^-} = -\frac{1}{2\text{z}}\left(V_{\text{M}} + V_{\text{M}^{\text{z}+}}\right)\left(-\gamma\kappa + \mathbf{e_n}\cdot[(\boldsymbol{\tau_d^{Li}} - \boldsymbol{\tau_d^{SIC}})\mathbf{e_n}]\right) + \frac{1}{2\text{z}}\left(V_{\text{M}} - V_{\text{M}^{\text{z}+}}\right)\left(\Delta p^{Li} + \Delta p^{SIC}\right) \tag{3.2}$$

Here, z is the number of electrons involved in the electrodeposition process, $V_{\text{M}^{\text{z}+}}$ is the molar volume of $\text{M}^{\text{z}+}$ in the solid electrolyte, and κ is the mean curvature at the interface. Stable electrodeposition occurs if i_{deformed} is lower than $i_{\text{undeformed}}$ at the dendritic tips and higher at the valleys. In order for this to happen, $\Delta\mu_{e^-}$ needs to be negative. [82, 83, 45] Since γ is negligible and the deviatoric term is always de-stabilizing, the hydrostatic stresses dictate the plating behavior, and a stability diagram can be constructed (Figure 3.1). [45, 8, 51]

The sign of the hydrostatic term is dependent on the molar volume ratio, $v = {}^{V_{\text{Li}^+}}/_{V_{\text{Li}}}$: when $v > 1$, $\Delta\mu_{e^-}$ only becomes negative if the shear modulus of the electrolyte is more than twice as large as that of the metal anode, $G^{SIC} > 2.2G^{Li}$, a prediction in agreement with that from Monroe and Newman [82, 83]; for $v < 1$, however, a "soft" SIC ($G^{SIC} < 0.7G^{Li}$) is required for stable plating.

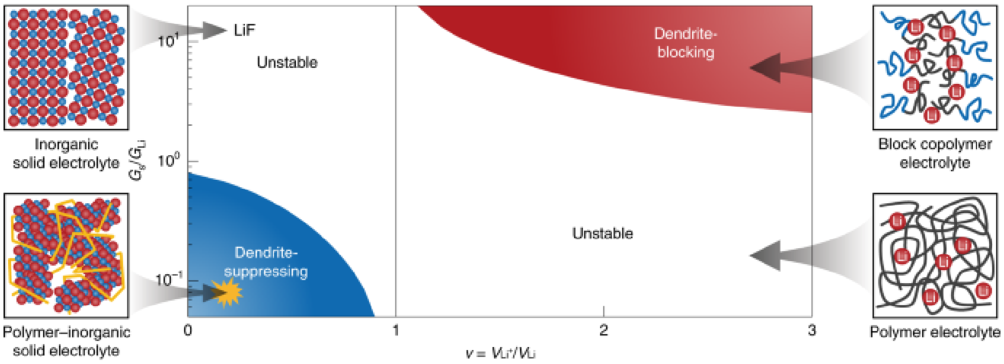

Figure 3.1: Chemomechanical model underlying the successes and failures of SICs in preventing instabilities at the anode surface during electrodeposition. SICs can access either dendrite-blocking character or dendrite-suppressing character, but not both. Prototypical SICs that serve as the battery's electrolyte are labelled in each region. [8]

These results explain why high-shear-modulus SICs with minimally reconfigurable ion-conducting domains ($v < 1$), such as ceramics, fall outside the stable deposition regime. Similarly, known "soft" electrolytes, particularly polymers, which typically undergo large volume changes as Li^+ exits transiently formed solvation "cages" ($v > 1$), also fail in preventing dendrite growth. [8] The only option for achieving stability requires employing a material with either (1) highly reconfigurable ion-conduction channels ($v > 1$) embedded in rigid host matrix ($G^{SIC} >> G^{Li}$), as is the case with block-copolymers, [84] or (2) ceremic-like ion-conducting channels ($v < 1$) in a low-shear modulus matrix ($G^{SIC} < 0.7G^{Li}$). [8] Block-copolymers have shortcomings [84] outside the scope of this work, which focuses on the design of a potential solution that fits the second case.

The best candidates for the ion-conducting inorganic phase are lithium halides (LiX, where X^-=F^-,Cl^-,Br^-, or I^-), since they present good ionic conductivity [85, 86] and are reductively stable on Li metal. Among these options, LiF was chosen as the inorganic phase due to it being oxidatively stable against high-voltage NMC-622 cathodes. Experimental constraints for *in situ* preparation of the composite required the use of a polymer of intrinsic microporosity (PIM), which allowed for homogeneous cation metathesis and LiF formation. The simplicity of the *in situ* process for composite creation inspired its name: a lithium electrode sub-assembly (LESA). [8]

3.1.2 Computational Chemomechanical Characterization of LiF@PIM Composite

Shear Modulus Calculation

Computational characterization of the PIM matrix was performed with molecular dynamics (MD) simulations, conducted on the Large-scale Atomic/Molecular Massively Parallel Simulator (LAMMPS) [87] software. A Dreiding [88] force field was used to simulate atomic interactions due to its capability of correctly predicting pore size and diffusion coefficient in the same class of polymers. The simulations included nearly 46,000 atoms, originally arranged in an amorphous collection of randomly ordered PIM tetramer chains. After 500 steps of conjugate gradient minimization, a NVT ensemble was performed at 350 K for 0.1 ns, followed by a total of 10 NVT annealing cycles between 350 and 700 K, at intervals of 35 K each, and for 2.5 ps at each temperature value. Post annealing, the overall density of the simulation box was too low compared to the bulk PIM density, so additional 4ns of NPT simulations at 300 K were run to recover the correct PIM density of $\sim$ 1g/cm^3. After these equilibration steps, a set of mechanical characterization simulations is performed. In order to retrieve the elastic moduli of PIM, the system was kept at a constant pressure of 1 atm in two directions (x and y), while the pressure along the z-axis was changed in steps from 1 to 9 atm. At each pressure value, the dimensions and associated strains of the simulation box were measured, allowing for calculation of all mechanical properties. Results from these MD simulations are in great agreement with experimental measures, as show in Table 3.1. While the presence and content of LiF can alter the mechanical response of the composite material, the maximum attained value of shear modulus is of $G = 376$ MPa, [8] keeping the ratio $^{G^{SIC}}/_{G^{Li}}$ at 0.023, significantly below the 0.7 limit for stability.

Property	MD	Experimental
Young's modulus (MPa)	469.6	438.9
Poisson's ratio	0.37 ± 0.08	0.33
Shear modulus (MPa)	171.4	165.0

Table 3.1: Mechanical properties of bulk PIM calculated with computational and experimental methods. Uncertainty in Poisson's ratio originates from the different measures in both x and y directions.

Hopping Energy Barrier and Molar Volume Calculations

The ratio between molar volume of Li and Li$^+$ determines the overall sign of the hydrostaic terms in the $\Delta\mu_{e^-}$ expression. The molar volume of Li$^+$ in the electrolyte is hard to determine by direct measurement, thus requiring other, theoretical and computational based techniques. While the Newman-Chapman relationship establishes an inverse relation between ion molar volume and transference number in binary electrolytes, [89] it cannot be applied for organic-inorganic composite systems. Therefore, V_{Li^+} was determined with computational first-principles DFT calculations.

Since the PIM polymer matrix does not have particularly good ion-conducting capabilities, the network of interconnected LiF particles provides the channels for Li$^+$ conduction. Given the small size of LiF particles, [8] LiF surface diffusion pathways are as numerous as the ones present in bulk. The main mechanism for ion conduction in LiF is through vacancy hopping. Using the nudged elastic band (NEB) method (further detailed in Appendix G), [90] it is possible to compare the energy barrier for vacancy hopping on bulk LiF with that on a (100) surface facet. The vacancy hopping pathway was computed in the projector augmented wave (PAW) code GPAW [73] with the Bayesian error estimation exchange correlation functional (BEEF-vdW), [74] which includes non-local van der Waals correlation and has been shown to perform better in accuracy than other functionals for the calculation of barrier heights. [91] The results of this analysis, shown in Figure 3.2a, [8] indicate that surface diffusion is significantly more favorable than ion motion in bulk: the surface activation energy is of $E_a = 0.34 \pm 0.13$ eV, while, for bulk, it is of $E_a = 0.62 \pm 0.17$ eV. The uncertainty estimate for E_a was carried out by utilizing the built-in error estimation capabilities within the BEEF-vdW exchange correlation functional, which bounds the barriers obtained using other generalized gradient approximation (GGA)-level exchange correlation functionals, [74] as demonstrated in Figure H.2. For comparison, the value of E_a calculated experimentally through the Arrhenius relation was of 0.42 eV, in great agreement with the computational predictions.

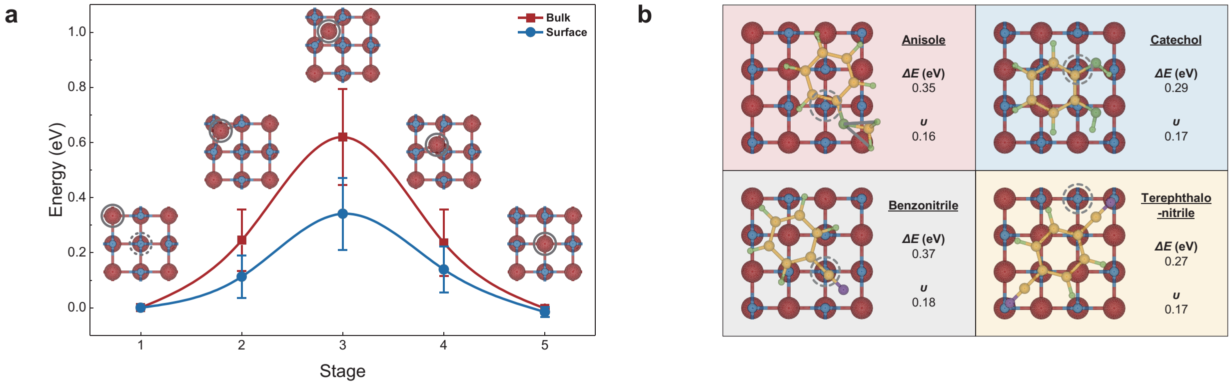

Figure 3.2: **(a)** Energy landscape of Li^+ surface diffusion on LiF and bulk transport within LiF. Insets: different stages encountered during hopping from a Li site (encircled in solid grey) to a nearby vacant site. The experimentally determined activation barrier for Li^+ hopping further takes into account the influence of PIM-1, which results in an 80 meV increase above the calculated result for the LiF surface. **(b)** Summary of vacancy diffusion barriers and ion molar volume ratios in the presence of PIM-like adsorbates in LiF. Grey circles indicate the initial (pre-hop) vacancy site. The corresponding values without such molecules are 0.34 eV for the barrier and 0.21 for the molar volume ratio. [8]

In order to determine the volume of the mobile ion, Bader charge analysis [92] was employed on all the different stages of hopping, yielding an average value of $v = {}^{V_{\mathrm{Li}^+}}/_{V_{\mathrm{Li}}} = 0.21$, further indicating LESA's capability of accessing in the dendrite-suppressing stability regime.

The presence of the polymer in the vicinity of the inorganic phase may influence the Bader volume, but this effect is expected to be small due to the absence of highly electronegative species that can bind to the LiF surface, so that v should remain less than 1. To validate this hypothesis, additional simulations were conducted, in which the polymer was modeled as selection of adsorbed molecular fragments representing the backbone or chain ends: namely, anisole, catechol, benzonitrile and terephthalonitrile. These adsorbates were placed parallel to the LiF (100) slab and at a distance of 2 Å. Given the polymer's three-dimensional (3D) contorted structure, it is unlikely that PIM chains would be completely flush with the LiF surfaces. Therefore, the imposed configurations correspond to worst-case scenarios for the impact these molecules would have on the energetics. As predicted, the influence of these molecules on both the energy barrier and the computed molar volume ratio is either favourable for electrodeposition stability, negligible or undetectable given the natural uncertainty of these properties, as shown in Figure 3.2b and Figure H.3. Differentiated energy landscapes for ion transport for either anion-rich or cation-rich LiF–polymer interfaces were also investigated (Figures H.4 and H.5), and the molar volume ratio for the cation-rich surface was calculated to be 0.18 (Figure H.6). Therefore, the dominant transport mechanism is expected to happen along LiF–polymer interfaces, where the presence of the PIM does not significantly affect E_a. Molar volume ratios for such composites may vary by surface structure or specific hopping trajectories, but over a decidedly narrow range ($0.16 \leq \upsilon \leq 0.21$).

3.1.3 LESA Performance

Performance testing of this innovative solid composite separator was done with high-voltage Li–NMC-622 cells, containing the optimized LESA formulation, a 30-μm-thick Li anodes and $1.44\text{mAh} \cdot \text{cm}^{-2}$ NMC-622 cathodes (Figure 3.3). During galvanostatic cycling at $1\text{mA} \cdot \text{cm}^{-2}$ at 20°C, the capacity faded at a rate of 0.07% per cycle, while the Coulombic efficiency was >99%. After having reached an initial capacity of $\sim 135\text{mAh} \cdot \text{g}^{-1}$, 80% was retained after $\sim$ 300 cycles. These data compare quite favourably against those for Celgard-only (negative control) and PIM-1-coated Celgard (positive control) (Figure 3.3), where cells reached 70% of their initial capacity after 130 and 100 cycles, respectively. This results in rates of capacity fade of 0.23% per cycle for Celgard-based cells and 0.3% per cycle for PIM-1-on-Celgard-based cells.

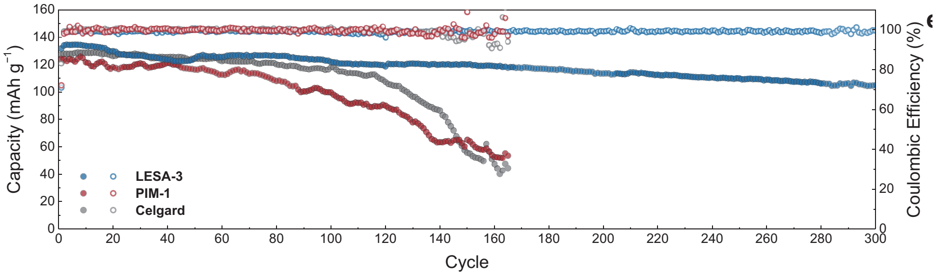

Figure 3.3: Rate tolerance of Li–NMC-622 cells (30-μm-thick Li anode; cathode areal capacity of $1.44\text{mAh} \cdot \text{cm}^{-2}$) cycled at 20°C, configured with either LiF@PIM-1 SICs (LESA 3), Celgard (negative control) or PIM-1-coated Celgard (positive control).

Surface Facets	Surface Energy (J/m^2)
LiF (001)	0.30
LiF (110)	0.74
LiF (111)	3.76
Li_2CO_3 (100)	0.62
Li_2CO_3 (001)	0.17
Li_2CO_3 (110)	0.51
Li_2CO_3 (101)	0.76

Table 3.2: Surface energies of LiF and Li_2CO_3. The slabs were generated using the pymatgen surface module [95, 96, 97] and the atomic simulation environment. [98]

3.2 Exploring the Role of Interfaces in Diffusion Dynamics

Understanding Li-ion transport through the solid electrolyte interphase (SEI) is crucial for improving the power capability of batteries. In the case of organic liquid electrolytes, two of the most common materials in the inner SEI layers are lithium fluoride (LiF) and lithium carbonate (Li_2CO_3). The presence of these two phases has been argued to promote the formation of Frenkel pairs, with an interstitial Li^+ in Li_2CO_3, and a negatively charged vacancy in LiF, which enhance Li^+ conduction though the SEI. [93] These results were based on calculations of defect formation energies on the bulk phases of LiF and Li_2CO_3, but the effect of the interface between these materials in ion transport is still under investigation.

3.2.1 Defect Formation Mechanism

DFT calculations performed with the Perdew, Burke, and Ernzerhof (PBE) exchange correlation functional [94] indicated that the most stable interface between LiF and Li_2CO_3 is composed of the facets LiF (001) and Li_2CO_3 (001), as seen in Table 3.2. Interfaces were constructed by placing slabs of both these surface facets parallel to one another. Considerations of coherency strain minimization and computational tractability led to the following multiplicities of the conventional unit cell lattice vectors: (1, 4, 2) for Li_2CO_3 and (2,5,1) for LiF. These supercells resulted in a coherency strain of 1.4 % (x axis) and 3% (y axis) on LiF, and -1.4 % (x axis) and -1.7% (y axis) on Li_2CO_3. A schematic of this system is shown in Figure 3.4. Single point calculations performed at discrete values of material separation yielded an optimal interfacial distance of ~ 3.44Å.

The interface between LiF and Li_2CO_3 in the SEI consists of undercoordinated atoms and hence, may be expected to host more defects than the bulk. It is proposed that Li-ion conductivity can be enhanced thanks to the following defect exchange reaction at the interface of the two materials: [93]

$$\mathrm{Li_{Li}(LiF)} \rightleftharpoons \mathrm{Li}_i^{\bullet}\,(\mathrm{Li_2CO_3}) + \mathrm{V_{Li}}'(\mathrm{LiF}),$$

where, $\mathrm{Li_{Li}}$(LiF) refers to a Li atom in a Li site in LiF, $\mathrm{Li}_i^{\bullet}$ (Li_2CO_3) refers to a Li interstitial defect in

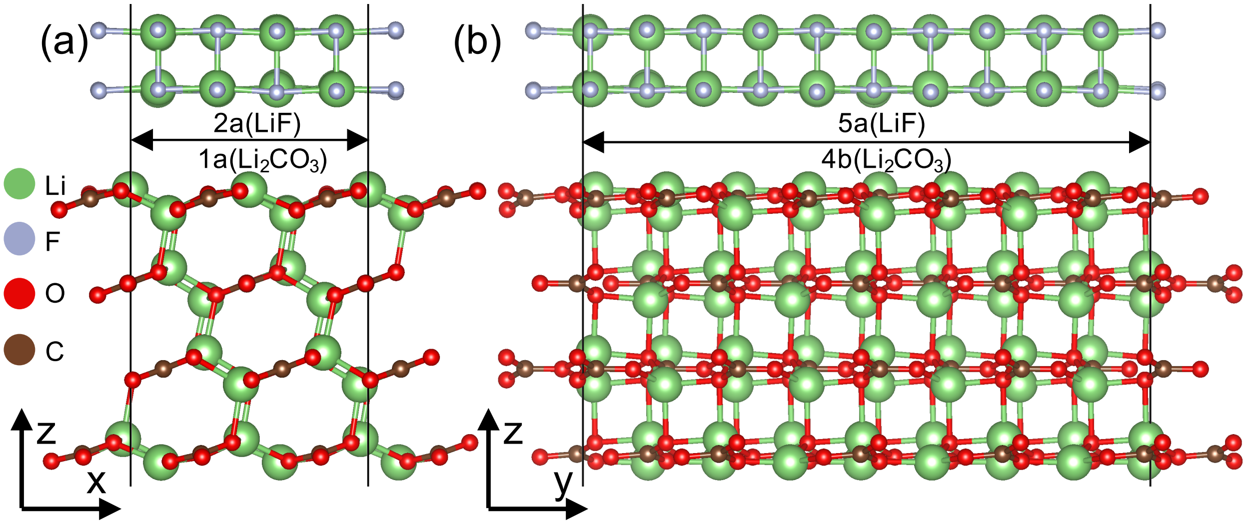

Figure 3.4: Geometry of the coherent interface between (001) LiF surface and (001) Li_2CO_3 surface used in DFT calculations. (a) Front and (b) side views along with the axes orientation. The black line is the boundary of the interfacial unit cell used in the simulations with the z axis is perpendicular to the interface.

Li_2CO_3 and V_{Li}'(LiF) refers to a Li vacancy in LiF. Studies based on bulk defect formation energies report an enthalpy change of 0.86 eV associated with this reaction, [99] but the explicit interface model predicts a value of 1.05 eV for the formation of this Frenkel pair. [100] However, this defect exchange reaction is still favorable with a free energy change of -0.76 eV when including the configurational entropy terms associated with the defects. [99]

3.2.2 Dynamics of Interstitial Li-ion Motion

Various mechanisms of Li hopping in SEI components have been proposed. An exhaustive study of the possible point defects and transport mechanisms in Li_2CO_3 found that Li interstitials have the lowest formation energy and are responsible for transport, especially at the anode side [101]. The most favorable pathway for ionic motion in this system is by the *knock-off* or "interstitialcy" mechanism, a form of indirect motion in which an interstitial atom displaces an atom in a lattice site into a neighboring interstitial site, and occupies the now vacant lattice site. By maintaining a high cation-anion coordination number through all stages of motion, the knock-off mechanism lowers the barrier associated with ion transport when compared to a direct interstitial-interstitial pathway. [101] Using the NEB method, [90] the minimum energy pathway shown in Figure 3.5 was obtained. Note that the first and the final hopping stages are not equivalent: given that the intended Li motion happens along the [011] direction, the initial interstitial atom has to be placed further from the interface than in the final configuration, as shown in the insets of Figure 3.5. This phenomenon can be partially explained by the space-charge effect, discussed in detail in Appendix I. The activation energy required to move an atom from one of these interstitial sites to another is thus dependent on the original site, and can be either 0.10 or 0.22 eV (a diagram of the net interstitial motion is represented in Figure J.1 in Appendix J). Therefore, the average hopping barrier associated with a net motion pathway parallel to the LiF-Li_2CO_3 interface is of ∼ 0.16 eV. The same knock-off mechanism in bulk Li_2CO_3 has an activation energy of 0.3 eV [101], further reinforcing the hypothesis that Li transport is enhanced at the interface of LiF and Li_2CO_3. The activation energy is also lower than that for Li hopping at the surface of LiF (0.34 eV). [8]

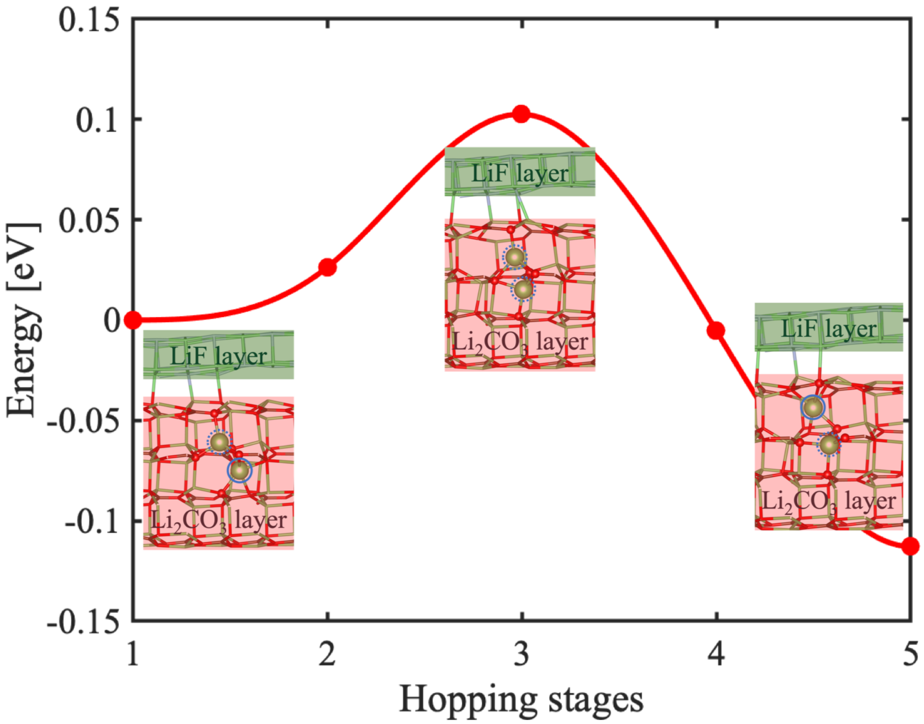

Figure 3.5: Energetics of minimum energy pathway of interstitial Li motion in Li_2CO_3 layer. Interstitial Li atoms are circled by a continuous blue line, while lattice Li atoms that partake in the motion are circled by a dashed blue line. The activation energy of Li hopping is reduced from 0.3 eV in bulk Li_2CO_3 to 0.10 or 0.22 eV in the interfacial structure considered, showing that the interface assists in Li diffusion.

Ab-initio MD simulations of this explicit interface further corroborate the hypothesis that the LiF-Li_2CO_3 facilitations Li-ion transport. The diffusion coefficient D can be calculated using a linear fit of the mean squared displacement (MSD) of Li ions as a function of time t:

$$D = \frac{1}{2dt}\langle \Delta R(t)^2 \rangle \tag{3.3}$$

where d is the dimension ($d = 3$ for a three-dimensional simulation) and ΔR is the ionic displacement. It is clear from the results that the Li atoms in layers closer to the interface have the highest diffusion coefficients, as shown in Figure 3.6

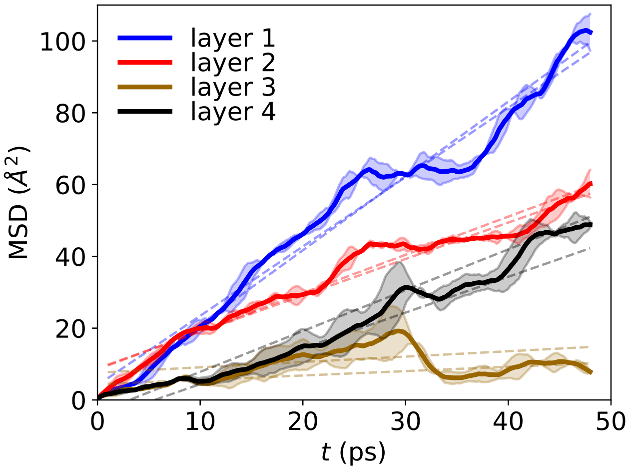

Figure 3.6: MSD for Li ions in Li_2CO_3 vs time calculated layerwise at 800 K. Layer 1 is closest to the interface while layer 4 is the farthest. The layers closer to the interface have the highest MSD. The higher value for layer 4 compared to layer 3 may be due to its exposure to vacuum.

The overall activation energy for Li diffusion in Li_2CO_3 is 0.51 eV. Since the MD simulations are run at high temperatures (600-900 K), the pathways with higher activation barriers become accessible, resulting in a high overall activation energy. An overall activation energy is obtained by averaging over the different pathways for Li hopping and hence is not solely determined by the pathway of least activation energy. Since the magnitude of mean squared displacement at 800 K is significant along the [100] direction, the one with highest activation energy, the overall activation energy includes contributions along that pathway and is thus much higher than that obtained by considering only the knockoff mechanism. The activation energy for diffusion along the [010] direction is 0.36 eV and is the lowest due to low activation energy pathways along this direction. Note that this value of self-diffusion is on par with the activation barrier of 0.31 eV [102] for the optimal ionic motion pathway in bulk Li_2CO_3 and close to 0.28 eV obtained by Iddir and Curtiss [103] considering motion along [010] open channels, further indicating that, on average, interfacial Li diffusion (whether mediated by interstitial atoms or otherwise) is faster than in the bulk. This analysis shows that it is beneficial to have the plane of the lattice matched interface between LiF and Li_2CO_3 perpendicular to the electrode-electrolyte interface to benefit from fast ion conduction along [010] direction.

3.3 Summary and Conclusions

This Chapter displays a few of the most interesting impacts that interfaces can have on battery materials, as well as ways to effectively use them while avoiding their drawbacks. Clever design of a solid polymer-inorganic composite separator shows how to harness the advantageous characteristics of both constituent materials to do something neither one of them can do on its own: suppress dendrite growth in Li metal batteries. The interface between LiF and Li_2CO_3, one of the most common in SEI structures, is shown to significantly enhance Li-ion mobility, especially along the Li_2CO_3 [010] direction, thus providing a design rule for further electrolyte engineering: electrolytes which, when in contact with the anode, decompose primarily into lithium fluorite and lithium carbonate are more suited for use in high-power battery cells. The contents of this Chapter highlight the undeniably integral role that interface engineering will continue to play in the development of next-generation all-solid-state Li-metal batteries.

Chapter 4

Thermodynamics of Void Formation

The topics covered in Chapter 3, while extremely relevant, are but a small sample of the abundant interface phenomena pertinent to Li-ion battery technology. It is also important to note that most of the work done in this area is somewhat new, with the majority of findings having been reached over the last decade. As illustrated by Figure 1.4, much remains to be discovered about solid-solid interfaces, keeping the field of all-solid-state lithium metal batteries (ASSLMB) far from mature. For example, electric aircraft applications, in particular, eVTOL, require high discharge power, and this can cause new failure mechanisms during the lithium stripping process: the formation of voids and pits on the surface of the anode. [104, 105, 106, 107, 108] Since the morphology of the surface of the lithium anode post-discharge can heavily impact the deposition process in subsequent cycles [46, 45, 109], it is essential to develop a fundamental understanding of void and pit formation associated with lithium stripping.

4.1 Need for a Fundamental Understanding of Void Formation

The pitting critical current density is lower than the plating one [104, 109, 110] but also with a greater dependence on the applied stack pressure [109]. Therefore, one potential avenue for preventing this issue would be application of stack pressure, which could raise the pitting critical current density by a factor of 5 from 3 to 7 MPa [109]. However, with current technology, an infeasible pressure would be needed for a Li metal battery to output the power performance required by electric aircraft. In order for more attainable mitigation strategies to be proposed, an understanding of the underlying process of void and pit formation is needed.

Various hypothesis have been formulated to explain the origin of this pitting behavior. Fundamentally, stripping involves transport of Li ions from the electrode to the solid electrolyte, resulting in Li vacancies in the electrode close to the interface which then diffuse into the bulk. If the stripping process is too fast, multiple vacancies can be generated close to the interface without being replenished with Li atoms due to vacancy diffusion, resulting in formation of voids. Krauskopf et al. [111] obtained a fundamental limit on the current density at the Li metal anode limited by vacancy diffusion equal to 0.1 mA/cm^2. This value is quite low to enable fast charging applications with planar Li metal electrode. Some studies suggest that the electrode microstructure plays an important role in the growth of voids, and demonstrate that pit nucleation and growth happens preferentially along surface GBs [112, 113], as shown in Figure 4.1a-f. Others suggest that some of the voids formed during stripping do not get filled in the plating process due to the lack of contact with the electrolyte [109], and, therefore, cause current to concentrate at the void edges. Besides aiding dendrite formation, this current focusing can occlude the void beneath the anode surface [109]. During following stripping cycles, these occluded voids can merge with other voids (occluded or new) and form pits. This process is exemplified in Figure 4.1m.

In other previous studies, [114, 115, 116] kinetic analyses of this phenomenon have been conducted at several length scales, ranging from atomistic [114] to nanometric [114, 115] to the meso-scale. [116] Combining density functional theory (DFT) with kinetic Monte Carlo (KMC) simulations of Li vacancy diffusion from surface to bulk (Figure 4.1g-l), Yang and Qi [114] demonstrated that the lithiophobicity/lithiophilicity nature of the interface between metallic anode and solid electrolyte governs pitting behavior. Similar conclusions were reached by Yang and Mo [115], who used *ab-initio* molecular dynamics (AIMD) simulations to show that, at incoherent interfaces between Li and solid electrolytes (SE), there exists a correlation between Li-SE lattice mismatch and pore size. Interestingly, both studies suggest that a Li/Li$_2$O interface (the one with highest values of work of adhesion among all interfaces considered in both studies) could withstand current densities many orders of magnitude above those observed experimentally: Yang and Qi [114] claim the Li/Li$_2$O interface can tolerate current densities of up to $\sim$100 A/cm^2 and Yang and Mo [115] show the critical current density for void formation on this interface to be of at least 1.6 nA/nm$^2 = 1.6 \times 10^5$ A/cm^2. However, lithium supplies used in most battery cell assemblies, in either academic or industrial settings, are almost invariably fully coated by Li$_2$O and generally do not undergo neither mechanical nor chemical cleaning processes prior to integration in the battery cell, indicating a discrepancy between these theoretical investigations and experimental observations. This inconsistency with experimental results is elucidated by Yan *et al.* [116], who argue that, for flat, defect-free Li/SE interfaces, vacancy diffusion from a Li surface to bulk Li is much faster than vacancy creation during stripping, and, thus, cannot fully explain pitting. Using meso-scale finite element modeling techniques, they show, however, that pre-existing defects – such as pores or voids – on the anode surface limit vacancy diffusion to bulk in such a way that only creep-induced currents are capable of competing with more realistic stripping current densities of 2-3$\times 10^{-3}$ A/cm^2, and at applied pressures higher than 12 MPa. However, Yan *et al.* [116] do not provide a possible origin for such pre-existing defects.

These studies indicate that the most promising direction to tackle the pitting problem is to better comprehend the formation of voids, which are simply an agglomeration of Li vacancies at the anode surface. Stable (void-free) electropolishing (stripping) can only be achieved if vacancies are soluble among the occupied Li sites at the anode surface. This thermodynamics-focused understanding of the overall pitting process can aid in finding mitigation routes for Li metal SSBs.

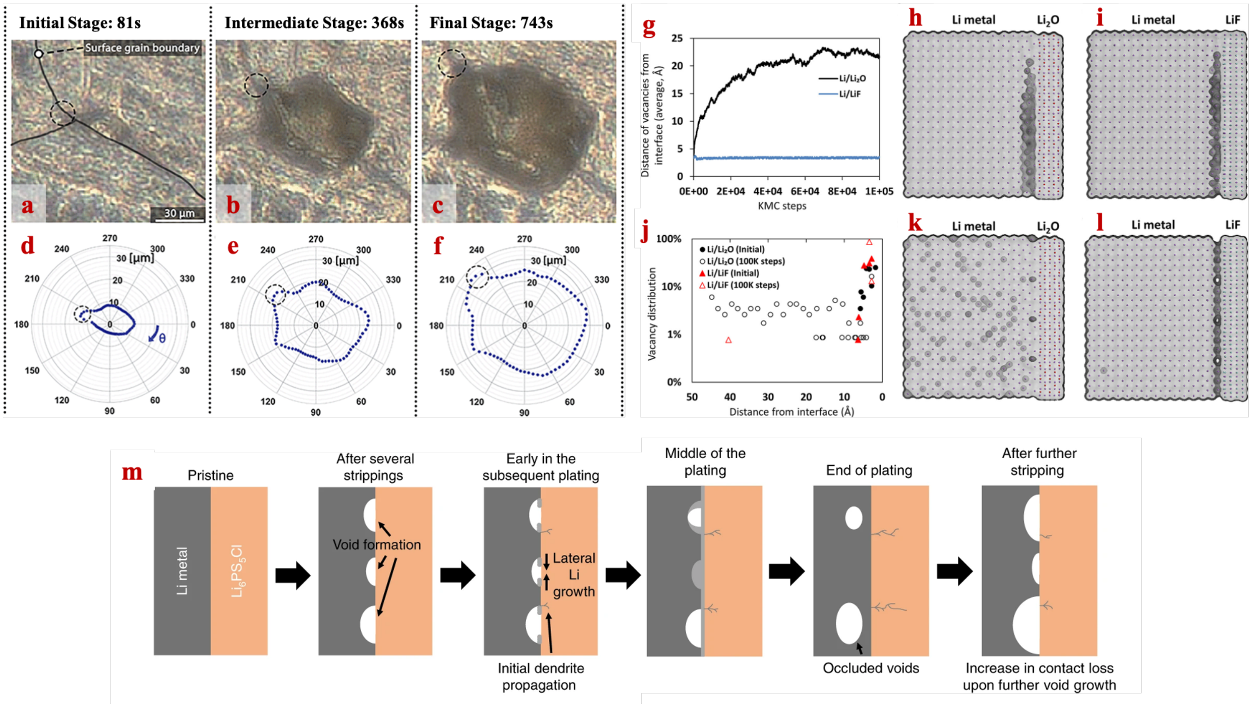

Figure 4.1: Images and depictions of the formation and evolution of pits, and migration of vacancies at and near interfaces of Li metal with other materials. **(a-c)** Optical images of evolution of a pit, with surface GBs outlined in black in panel **a**. **(d-e)** Polar plots of the distance between the edges and the center of the pit at times 240s, 430s, and 730s, respectively. Panel **g** shows the average distance between vacancies and anode surface as a function of number of kinetic Monte Carlo (KMC) steps taken. The initial configurations are displayed in panels **h** for Li/Li_2O and **i** for Li/LiF, while the configuration at 10^5 KMC steps are represented in panels **k** for Li/Li_2O and **l** for Li/LiF. It is evident that vacancies in Li metal are much more likely to diffuse into bulk when Li_2O is present at the interface, instead of LiF. Panel **m** is a schematic of one of the proposed hypothesis for pit formation: as voids are formed during stripping and then occluded during plating, they can merge with other voids on subsequent stripping processes and create large pits. Panels **(a-f)** are reproduced with permission from Ref. [112], **(g-l)** from Ref. [114], and **m** from Ref. [109].

4.1.1 Modeling Vacancy Solubility

Regular solution models have been used to study a myriad of mixture systems, ranging from binary [117] to high-entropy alloys. [118] They have also been successfully employed to describe the behavior of two-dimensional systems, such as surfaces and interfaces, in contexts ranging from adsorption [119, 120] to grain boundary phase transitions. [121] They are thus one of the most successful universal theories to describe solutions, solid or liquid, and are also very similar to the theory described in Chapter 2. The regular solution model compares the Gibbs free energy (G) of the solution of species A and B with that of the mechanical mixture (isolated non-interacting materials) of the two species. Assuming the solution contains a total of N_A atoms of type A, and N_B of type B, the Gibbs free energy of the mechanical mixture is given by:

$$G_{mech} = N_A \mu_A + N_B \mu_B, \tag{4.1}$$

where μ represents the chemical potential of the species in their pure form. Note that, since the reference state is pure A and pure B species, their entropy is zero, and only enthalpic terms contribute to μ_A and μ_B. Assuming that, in solution, the atoms are uniformly distributed, the change in configurational entropy is given by the Boltzmann's entropy formulation:

$$\Delta S = k_B \ln(W), \tag{4.2}$$

where k_B is Boltzmann's constant and W is the number of microstates the system can exhibit. Here, W can be calculated with simple combinatorics. Using $N = N_A + N_B$,

$$W = \binom{N}{N_A}$$

Therefore,

$$\begin{aligned}\frac{\Delta S}{k_B} &= \ln\left[\binom{N}{N_A}\right]\\ &= \ln\left[\frac{N!}{(N-N_A)!N_A!}\right]\\ &= \ln(N!) - \log[(N-N_A)!] - \ln(N_A!)\end{aligned}$$

Using Stirling's approximation ($\log(n!) \approx n\log(n) - n$) and the fact that $N - N_A = N_B$ yields:

$$\begin{aligned}\frac{\Delta S}{k_B} &\approx N\ln(N) - N - (N-N_A)\ln(N-N_A) + (N-N_A) - N_A\ln(N_A) + N_A\\ &= (N_A+N_B)\ln(N) - N_A\ln(N_A) - N_B\ln(N_B)\\ &= N_A\ln\left[\frac{N}{N_A}\right] + N_B\ln\left[\frac{N}{N_B}\right]\end{aligned}$$

Let $x_A = {}^{N_A}/_{N}$ and $x_B = {}^{N_B}/_{N}$ such that $x_A + x_B = 1$. Normalizing the entropy gives

$$\Delta s = \frac{\Delta S}{N} = -k_B\left[x_A\ln(x_A) + x_B\ln(x_B)\right] \tag{4.3}$$

The calculation of the enthalpy of mixing assumes that the general structure of both pure A and B materials, as well as the solution, is the same, that is, all atoms interact with z total neighbors. An additional assumption, akin to mean-field methods, is also needed: the average neighborhood of each atom follows the same distribution as the overall solution, meaning that each atom interacts with zx_A atoms of type A and zx_B atoms of type B. Using the index IJ to denote interactions between atoms of types I and J, one can express the enthalpy of the mechanical mixture as:

$$H_{mech} = \frac{z}{2}(N_A\epsilon_{AA} + N_B\epsilon_{BB}),$$

where ϵ denotes the total interaction enthalpy, and the factor of 2 in the denominator comes from the assumption that interaction energies are shared equally between atoms. For the actual solution, the enthalpy can be written as:

$$\begin{aligned} H_{sol} &= \frac{z}{2}[N_A(x_A\epsilon_{AA} + x_B\epsilon_{AB}) + N_B(x_A\epsilon_{AB} + x_B\epsilon_{BB})] \\ &= \frac{Nz}{2}(2x_Ax_B\epsilon_{AB} + x_A^2\epsilon_{AA} + x_B^2\epsilon_{BB}) \end{aligned}$$

The enthalpy difference between mechanical mixture and solution, normalized by the total number of atoms, becomes:

$$\Delta h = \frac{z}{2}[2x_Ax_B\epsilon_{AB} + x_A(x_A - 1)\epsilon_{AA} + x_B(x_B - 1)\epsilon_{BB}] \tag{4.4}$$

Since $x_A + x_B = 1$, the previous expression can be simplified:

$$\Delta h = \frac{z}{2}x_Ax_B(2\epsilon_{AB} - \epsilon_{AA} - \epsilon_{BB}) \tag{4.5}$$

Using the changes in entropy and enthalpy from Equations 4.3 and 4.5, the change in Gibbs free energy, normalized by N, is calculated from $\Delta g = \Delta h - T\Delta s$ (where T is the system temperature), giving:

$$\Delta g = x_Ax_B\Omega + k_BT[x_A\ln(x_A) + x_B\ln(x_B)], \tag{4.6}$$

where $\Omega = (z/2)\,(2\epsilon_{AB} - \epsilon_{AA} - \epsilon_{BB})$. The chemical potential of either species (relative to their pure structure in the mechanical mixture) can be obtained by taking the derivative of Δg from Equation 4.6 with respect to the species molar fraction, x_i. The stability criteria against spontaneous flow of species demands that

$$\left(\frac{\partial \mu_i}{\partial x_i}\right)_{T,V} > 0$$

If this condition is not met, a phase transition occurs, and a miscibility gap is formed. In the case of the regular solution model,

$$\begin{aligned} \left(\frac{\partial \mu_i}{\partial x_i}\right)_{T,V} = \left(\frac{\partial^2}{\partial x_i^2}\Delta g\right)_{T,V} = -2\Omega + \frac{k_BT}{x_i(1 - x_i)} > 0 \Rightarrow \\ \Rightarrow T > \frac{2\Omega}{k_B}x_i(1 - x_i) \quad \forall x_i \in [0, 1] \end{aligned}$$

From this, and given that $x_i(1-x_i)$ attains a maximum value of $1/4$ for $x_i = 0.5$, it becomes clear that this system has a critical temperature of

$$T_c = \frac{\Omega}{2k_B} \tag{4.7}$$

For temperatures above T_c, the two species A and B are perfectly soluble in one another, but, for temperature values below T_c, a miscibility gap is formed. This can be seen in Figure 4.2: at temperatures higher than T_c (red line), Δg is convex everywhere in the domain, indicating $(\partial\mu/\partial x_i) > 0$ for all values of x_A; at the critical temperature T_c (yellow line), the double derivative of Δg with respect to x_A becomes zero at $x_A = 0.5$ and represents the onset of a phase transition; for temperature values lower than T_c (turquoise and blue lines), for some values of overall x_A, two phases, one with low characteristic x_A and one with high characteristic x_A, coexist, and correspond to the two minima in the Δg curve.

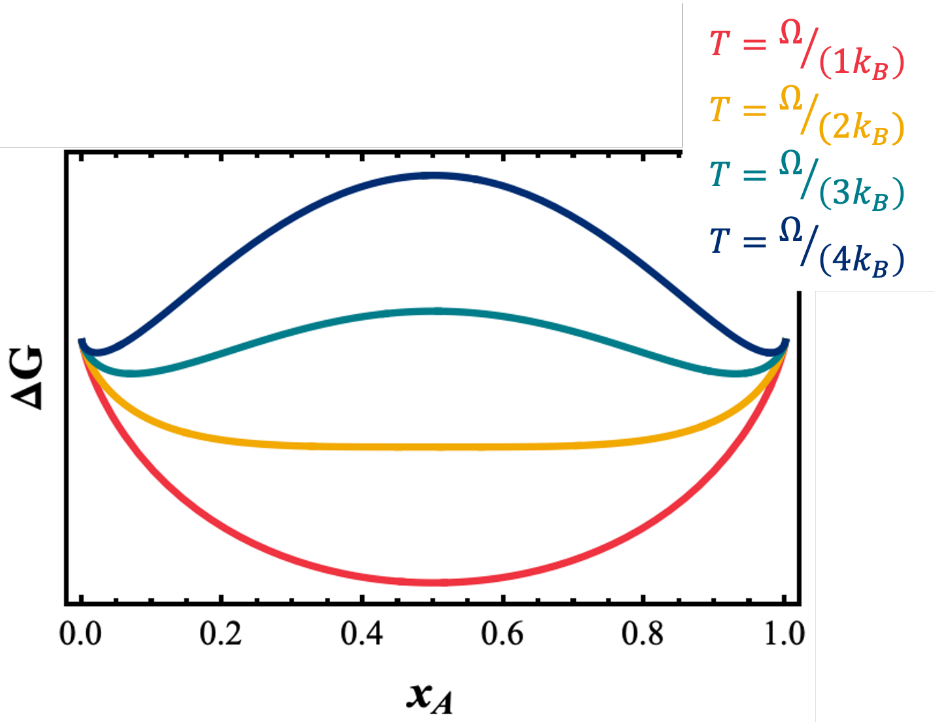

Figure 4.2: Diagram of relationship between ΔG and x_A for different temperatures. At temperatures higher than T_c (red line), Δg is convex everywhere in the domain, indicating $(\partial\mu/\partial x_i) > 0$ for all values of x_A; at the critical temperature T_c (yellow line), the double derivative of Δg with respect to x_A becomes zero at $x_A = 0.5$ and represents the onset of a phase transition; for temperature values lower than T_c (turquoise and blue lines), for some values of overall x_A, two phases, one with low characteristic x_A and one with high characteristic x_A, coexist, and correspond to the two minima in the Δg curve.

By considering vacant and occupied sites in the surface of Li metal as different species (A and B), it is possible to apply the regular solution model to the problem of void and pitting formation. [122] In this formalism, the existence of a phase with vacancy concentration higher than that of the overall system corresponds to the onset of void formation. Owing to the fact that vacant and occupied sites always occupy the exact same lattice sites (meaning there are no interstitial atoms or other defects), their respective reference states have equal coordination numbers, making this a perfect case study for the regular solution model. Furthermore, the lack of long range interactions makes the inclusion of only nearest-neighbor bonds sufficient to capture the thermodynamics of this system. Finally, since we employ first-principles calculations of actual mixture systems to extract the required model parameters, explicit considerations of vacancy reference states are circumvented.

4.1.2 Void Behavior for Isolated Lithium Slabs

The relevant parameters for the regular solution-based analysis, namely, Ω, ϵ_{LL}, ϵ_{VV} and ϵ_{VL} (where the index V corresponds to a vacant site, and L, to an occupied site) were estimated by using first-principles DFT with the Perdew, Burke, and Ernzerhof (PBE) exchange correlation functional [94] in the projector augmented wave (PAW) code GPAW [73] implemented in the Atomic Simulation Environment (ASE) [98]. Details on how to extract these parameters from DFT calculations can be found in Appendix L.

Three low Miller index surface facets were considered for Li metal: (100), (110), and (111). A schematic of the different surface interactions considered is shown in Figure 4.3. For each facet, two possible interactions were examined: one between vacancies which are both located on the top-most Miller plane on the surface (shown in purple), and another between vacancies that are located on different Miller planes, where one is at the surface, and another is right below it (shown in orange). For simplicity, superscripts 1 and 2 are used to denote the surface-level Miller plane and the plane immediately under it, respectively. For example, $\Omega^{(11)}$ denotes the interaction parameter on the surface plane (intra-plane), while $\Omega^{(12)}$ corresponds to the interaction parameter between the two different Miller planes mentioned (inter-plane). Note that, for the (110) facet, further distinctions have to be made: there are two different intra-plane interactions, one with four neighbors, and one with two neighbors, as well as two different inter-plane interactions, both with only two neighbors, as represented in Figure 4.3. Due to the limitations of the regular solution model, it is infeasible to take into account all these different possibilities separately. Furthermore, evaluating the differences in interaction energies for all these cases shows that the standard deviation of these values represents $\lesssim 8\%$ of the corresponding energies. Therefore, in the case of the (110) surface, we incorporate these distinct interactions by averaging them together, in proportion to the number of neighbors involved. The results of the DFT predictions for an isolated Li-metal slab are shown in Table 4.1, which also includes the average distances, denoted by $d^{(11)}$ and $d^{(12)}$, between a lithium atom in the surface-level Miller plane

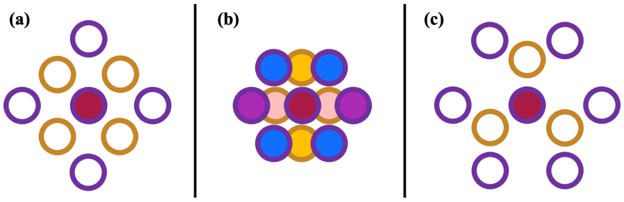

Figure 4.3: Top-view schematic of the different possible interactions considered for the **(a)** (100), **(b)** (110), and **(c)** (111) lithium surface facets. Purple circles denote lattice sites on the outer-most surface layer, and yellow orange circles denote sites on the second outer-most layer. In the (110) case (panel **(b)**), there are several different pair-wise interactions: red-purple, red-blue, red-yellow, and red-pink. In the other two cases, all purple-purple and orange-orange site interactions are equivalent. [122]

and a neighboring lattice site, in either the same plane or in the one below.

Facet	(100)	(110)	(111)
$z^{(11)}$	4	6	6
$z^{(12)}$	4	4	3
γ [eV/Å^2]	$\sim$ 0.030	$\sim$ 0.031	$\sim$ 0.034
$\langle d^{(11)} \rangle$ [Å]	3.44	3.13	4.86
$\langle d^{(12)} \rangle$ [Å]	3.03	3.17	3.05
$\Omega^{(11)}$ [eV]	0.331	0.269	0.016
$\Omega^{(12)}$ [eV]	0.223	0.012	-0.194
$T_c^{(11)}$ [K]	$\sim$ 1980	$\sim$ 1600	$\sim$ 100
$T_c^{(12)}$ [K]	$\sim$ 1340	$\sim$ 70	0

Table 4.1: Approximate surface energies, coordination numbers, interaction parameters, and critical temperatures for different surface facets. Given the relatively small difference in surface energies, it is fair to assume all facets are equally relevant. The strongest interactions in the (100) and (110) facets have very high critical temperatures for vacancy solubility (above 1000 K), meaning that, under standard operating conditions, vacancies will tend to phase separate and begin forming voids. That is not the case for the (111) surface, where vacancies are fully solvable and, under equilibrium conditions, should be uniformly distributed on the surface. [122]

These estimates indicate that all three facets have similar surface energy and hence, could all be formed during the electrodeposition process. Control of crystallographic grain growth direction in Li metal batteries has been demonstrated in the context of lithium electrodeposition. [123] Vacancy-vacancy interactions are highly favorable in the (100) facet, regardless of the Miller planes of the vacancies, but their attraction is stronger when they are both on the top plane. This implies that the critical temperature for vacancy solubility in this surface is extremely high, above 1300 K, and that, under equilibrium conditions, vacancies will tend to phase separate and, thus, initiate the formation of large voids. Similar to the (100) facet, the strongest interactions in the (110) facet are also intra-plane; however, in this case, the inter-plane interactions are much weaker, and entropic contributions push vacancies in different planes apart even at low temperatures. Therefore, in this case, vacancies are expected to congregate on the top Miller plane, and, in doing so, form steps on the surface, which can lead to increased surface roughness and facilitates void and pit formation.

Interestingly, the (111) facet exhibits the opposite behavior: the intra-plane interactions, albeit attractive, are relatively weak, while the inter-plane ones are stronger, but highly repulsive. This suggests that, under equilibrium and at normal operating conditions, the (111) surface, by having perfect vacancy solubility, is the most likely to prevent the issue of void formation and pitting. [122] The expected behavior of these surfaces, assuming vacancy diffusion to be fast enough as to not constitute a limiting factor for vacancy accumulation, is shown in Figure 4.4.

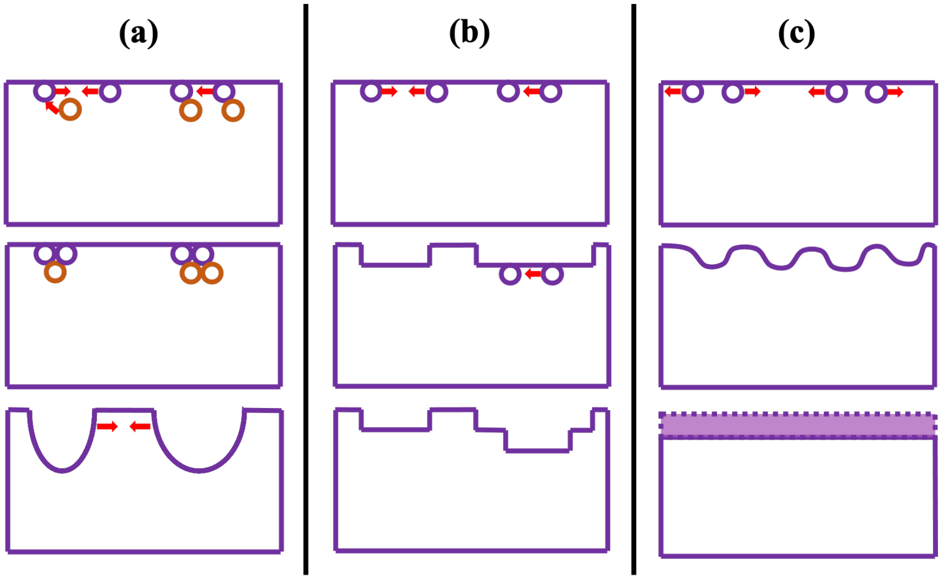

Figure 4.4: Side-view schematics of the expected behavior of **(a)** (100), **(b)** (110), and **(c)** (111) lithium surface facets during stripping, respectively. These diagrams neglect kinetic barriers associated with vacancy motion, and assume that, in all cases, vacancy diffusion along the surface planes is not a limiting factor. Note that these schematics solely portray predictions from our first-principles informed regular solution model for isolated Li-slabs; to the authors' knowledge, there has been no experimental evidence for these phenomena. The removal of atoms during discharge creates vacancies on the surface, denoted by circles. Purple circles represent vacancies on the surface-level Miller plane, and orange circles are vacancies on the second outer-most layer. Red arrows show the interactions between vacancies. In the (100) facet, vacancies will attract each other regardless of layer, and can thus form large (in an atomistic scale) valleys. The (110) surface exhibits a somewhat similar behavior, but, due to the inter-layer vacancy repulsion, vacancies would only congregate on the surface-level Miller plane. By doing so, they form steps that expose the underlying layer and creates a new surface for lithium extraction. In this case, valleys would be formed as a collection of terraces. The (111) facet shows the most promise: the strong inter-layer vacancy repulsion, coupled with the weak intra-layer attraction, will force vacancies to be uniformly distributed on the surface. In doing so, when enough lithium is stripped, a relatively flat surface will emerge. The light pink rectangle in panel **(c)** enclosed by the dashed line indicates the stripped layer. [122]

4.1.3 Effects of Interfaces on Void Formation

Li/SEI Interfaces

The analysis in the previous section was performed considering solely a Li-slab, surrounded by vacuum, as described in Appendix L. However, in practical battery applications, the surface of the anode is always either coated by a film, whether an oxide layer of a solid electrolyte interphase (SEI), or in direct contact with the surface of a solid electrolyte. In order to better capture a more realistic behavior of void formation in lithium metal batteries, similar DFT simulations were carried out in interfaces between the same lithium slabs and surface facets of two common SEI materials: LiF(001), LiF(110), and Li_2CO_3(001). These particular facets were chosen due to their low surface energies, as well as ease to computationally integrate into interface structures. [100] Such interfacial structures were built in a coherent manner [100] such that normal strains on the lithium slabs never exceeded 7.5%, and were limited to 4.2% on the SEI materials. [122] This lower threshold comes from the fact that most SEI materials tend to be brittle; in most interfaces, including all of the Li/Li_2CO_3 systems, normal strain on SEI materials remained at 0%. A coherent, low strain, computationally tractable interface between Li(111) and Li_2CO_3(001) was not feasible. For each interface, the distance between anode and SEI surfaces was optimized, as well as the relative in-plane shift between them. An example of such interfaces can be seen in Figure 4.5.

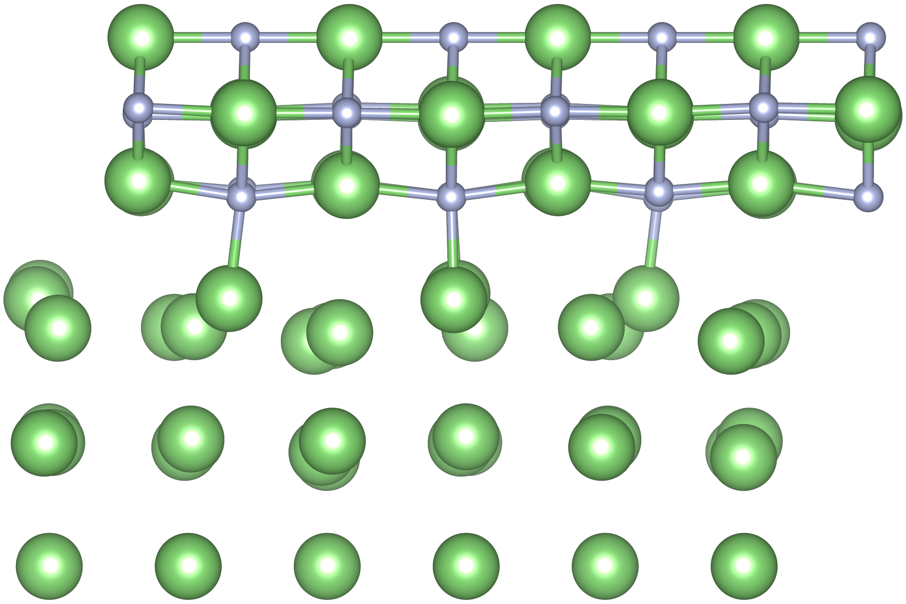

Figure 4.5: Schematic of a Li(110)/LiF(110) interface used in DFT simulations for estimation of regular solution parameters. [122]

Due to local inhomogeneities, the values of $\Omega^{(11)}$ and $\Omega^{(12)}$ vary spatially along the Li surface, as shown in Figure 4.6, where the atoms from the SEI material are represented as circles, and their proximity to the

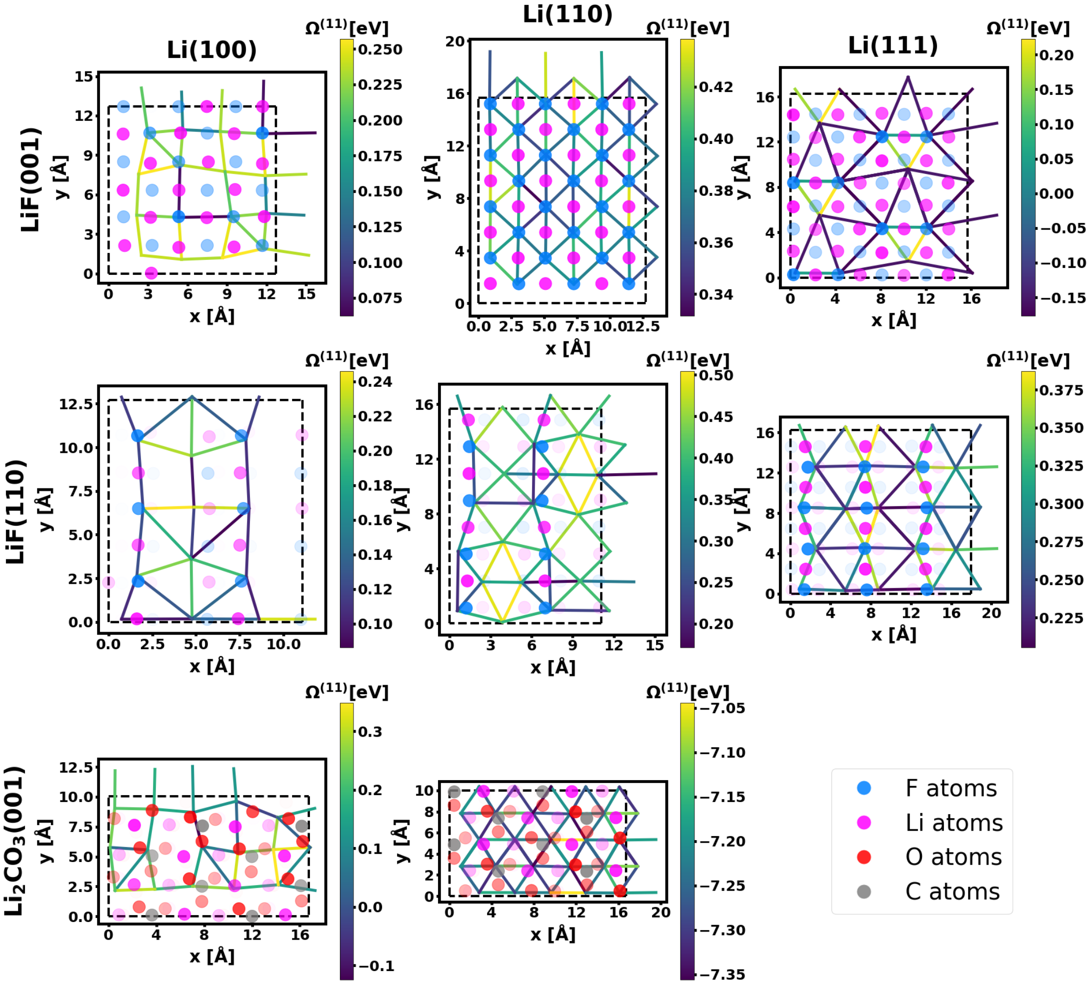

Figure 4.6: Representation of values of $\Omega^{(11)}$ along the surfaces of Li slabs at the corresponding interfaces with SEI materials. The colored circles represent the location of atoms in the SEI material, and their opacity is inversely proportional to their distance from the interface: circles that are more translucent are further from the interface, and those that are more opaque are located closer to the Li surface. Dashed black lines indicate the limits of the super cell used in the simulation. [122]

surface of lithium is directly related to their opacity level. For each of the different values of Ω, a critical temperature can be calculated, and its distribution plotted, as illustrated in Figures 4.7 and 4.8. Interestingly, the presence of these SEI materials has diverse effects on the regular solution model parameters. For example, the LiF(001) facet can at the same time lower the critical temperature of the Li(100) surface, but raise that of the Li(110) surface; the Li(111) interfaces are no longer stable during stripping; and Li_2CO_3 is capable of preventing vacancy clustering in a Li(110) interface. The relative inconsistency in behavior of this vacant-occupied sites solution serves as further indication of the need for a more in-depth understanding of the mechanisms behind void and pit formation in Li-metal batteries.

The relationship between the main thermodynamic parameters ($\epsilon_{VL}, \epsilon_{VV}, \epsilon_{LL}$, and Ω) and their local chemical environment was evaluated by comparing the values of said parameters and the distance to the closest Li, F, C, or O atoms in the SEI material, as represented in Figures 4.6 and 4.9. Given the atomic structure of Li_2CO_3, distances to the closest cluster of 3 oxygen atoms were also considered. As shown in Figure 4.9, there is no clear correlation between these parameters and the distance to atoms in the SEI material, with exception of the Li(110)/LiF(001) interface, where there is a high penalty to removing a Li atom from the Li slab at a distance of ~ 2.2Å to the closest F atom in the LiF slab. This happens because the average value of the Li-F bond length in the strained LiF material is approximately 2.2Å as well. Curiously, Figure 4.9 also shows that, in the case of the Li(110)/Li_2CO_3(001) interface, the beneficial effects due to the presence of unstrained Li_2CO_3 outweigh those due to the strain in the anode surface: the values of the relevant parameters for the interfacial system differ from those of the isolated unstrained Li slab system (green line in the plots) significantly more than the difference in the same values between strained (orange line in the plots) and unstrained Li slabs.

To better unravel the effect of SEI materials on the likelihood of vacancy congregation, an analysis of the adhesion energy associated with each interface was performed. The adhesion energy can be calculated as follows: [100]

$$E_{\text{adhesion}} = \frac{1}{A}\left[E_{\text{interface}} - (E_{\text{Li,slab}} + E_{\text{SEI,slab}})\right], \tag{4.8}$$

where E_{adhesion} is the adhesion energy, A in the interfacial area, $E_{\text{interface}}$ is the energy of the interfacial structure, and $E_{\text{Li,slab}}$ and $E_{\text{SEI,slab}}$ are the energies of isolated strained Li and SEI slabs, respectively. According to Equation 4.8, lower adhesion energies indicate a more energetically favorable interface. Our results, shown in Figure 4.10, indicate that higher values of adhesion energy are associated with higher values of Ω, while lower adhesion energy yields lower Ω values. [122] As illustrated in Figure 4.4, as vacancies congregate in the surface of the metallic anode, they form voids, making the anode surface not be in direct contact with the SEI nor the solid electrolyte. Therefore, when the adhesion energy between lithium and

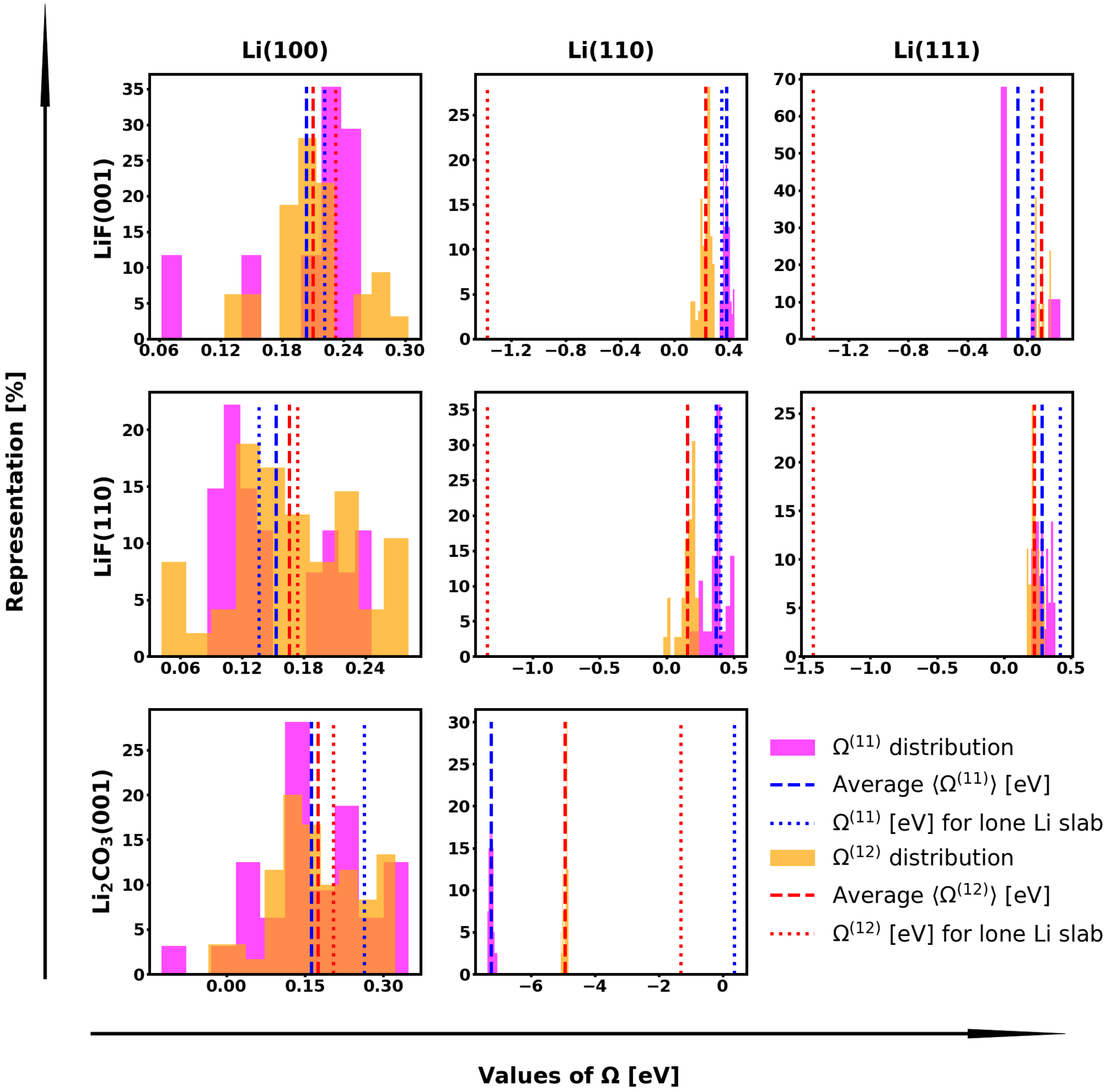

Figure 4.7: Distribution of values of $\Omega^{(11)}$ and $\Omega^{(12)}$ along lithium surfaces of specified interfaces. Dotted lines indicate the corresponding values for a strained, isolated Li slab. LiF seems to have little to insignificant impact on $\Omega^{(11)}$ parameter, while, at the same time, increasing the value of $\Omega^{(12)}$ at its interfaces with Li(110) and Li(111). Interestingly, Li_2CO_3 decreases the values of both Ω parameters, and, in the case of the interface with Li(110), this SEI material is capable of lowering the critical temperature for vacancy solubility to 0 K, a very promising result that indicates a potential for this interface to prevent the formation of voids on the anode surface. [122]

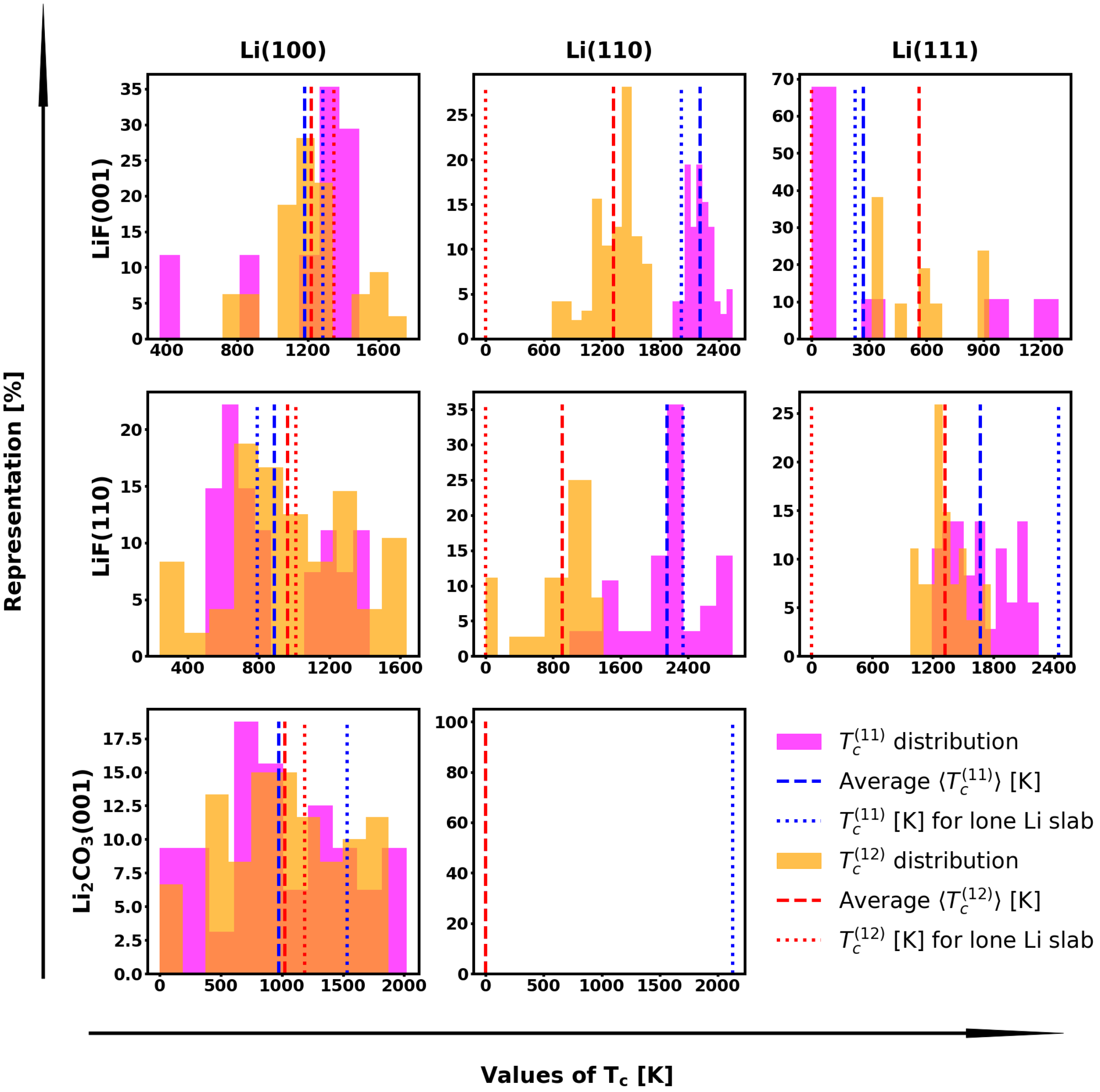

Figure 4.8: Distribution of critical temperature T_c values for the different Li-SEI interfaces considered. Values of T_c are calculated from values of Ω in Figure 4.7 according to Equation 4.7. [122]

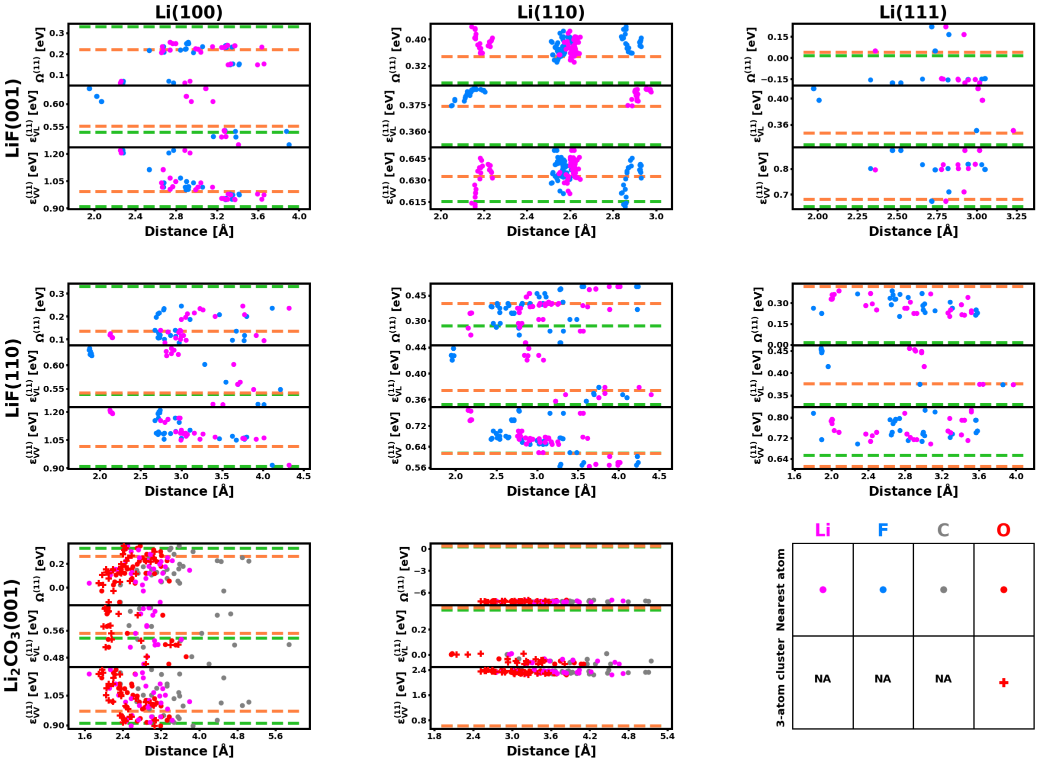

Figure 4.9: Relationship between thermodynamic parameters and distance to the closest atoms in the SEI material. The corresponding values of said parameters for the isolated unstrained and strained Li slabs are shown in green and orange, respectively. Due to the atomic structure of Li_2CO_3, distances to the closest cluster of 3 oxygen atoms were also taken into account. No obvious correlation can be found, with the exception of the Li(110)/LiF(001) interface. [122]

SEI (or solid electrolyte) is low, there is a thermodynamic driving force that pushes vacancies on the lithium surface away from one another, as to prevent them from gathering and creating facets that do not interact as strongly with the SEI. In cases where the adhesion energy is high, there is little external influence on the behavior of vacancy congregation. This reveals a potential design rule for filtering candidate materials for use in artificial SEI or solid electrolytes coupled with a metallic lithium anode, and is in accordance with previous studies that focused on kinetics. [114, 115]

The analysis above identifies that an isolated, unstrained, (111) Li surface facet could help mitigate this issue under equilibrium conditions. However, further investigations show that anode strain and the presence of SEI materials in proximity to the anode surface can have significant impacts in the thermodynamics of vacancy congregation, thus reinforcing that simulations of isolated slabs are not an appropriate surrogate to material interfaces. As represented in Figure 4.7, in some cases, such as that for the Li(100)/LiF(110)

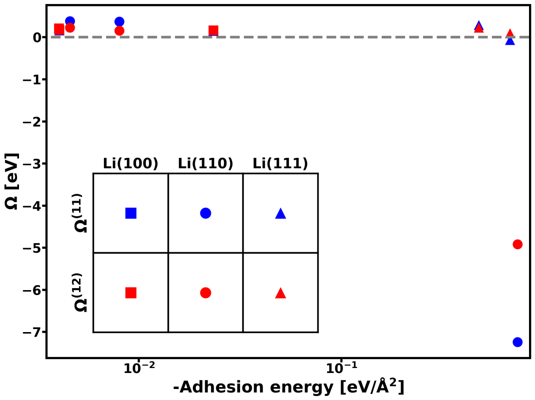

Figure 4.10: Plot of $\Omega^{(11)}$ and $\Omega^{(12)}$ as a function of the negative of the adhesion energy associated with the corresponding interface. This graph shows that lower adhesion energies yield lower values of Ω, and, thus, a Li surface that is more stable against void formation.

interface, the impact of anode strain on thermodynamic parameters outweighs that of interactions between the constituent (strained) materials; nevertheless, in most cases shown, including the Li(110)/Li_2CO_3(001) and Li(100)/Li_2CO_3(001) interfaces, the influence of interfacial effects exceeds that of anode strain. Among all the anode/SEI interfaces considered, the Li(110)/Li_2CO_3(001) seems to be have the highest likelihood of hindering the initial step required by void formation. There is some evidence that this phenomenon is in part explained by the low adhesion energy of this interface, which hinders vacancies from accumulating and reducing the interaction strength between the surface of Li and the SEI component. While the high strain employed in our simulations renders some of the obtained values of adhesion energy unrealistic, our analysis shows that this parameter appears to be a valuable metric for material selection for Li metal batteries, in accordance with previous work. [114, 115] However, since anode/SEI interfaces in real batteries are not necessarily coherent and tend to experience values of strain significantly lower than the ones employed here, further investigations of the impact of adhesion energy and void formation behavior are needed. For instance, combining the thermodynamic analysis presented here with previously studied kinetics models [114, 115, 116] can provide a deeper, more holistic comprehension of the mechanism of void and pit formation at anode/SEI and anode/solid electrolyte interfaces: integrating our methodology to nudged elastic band (NEB) calculations of concentration-dependent Li vacancy hopping barriers along and away from such interfaces [114], as well as to interfacial structure considerations [115], can allow for more accurate, first-principles informed continuum scale modeling of void formation, akin to that of Yan *et al.* [116]. For example, this could facilitate further studies of the effect of SEI layer thickness and composition on pitting behavior, as well as the potential impacts of other materials, such as lithium alkyl carbonates – which represent a major part of the SEI – and sulfide-based electrolytes.

Li/Interlayer Interfaces

As illustrated in Figure 1.3, the structure of the SEI film is complex, making it a challenge to properly engineer this critical component of a lithium battery. Therefore, solutions to the void formation issue that rely on SEI engineering are not immediately applicable, and more pragmatic alternatives need to be found. The application of stack pressure during battery operation has demonstrated promising results, but the required pressure values of 10-40 MPa [116, 110] also render it impractical.

A different option is using thin metallic interlayers (ILs) at the interface between the anode and the solid electrolyte, [110, 124, 125, 126, 127] which are known to reduce interfacial impedance and thus raise the critical current density (j_c) associated with dendrite formation in Li metal batteries. Symmetric Li/IL/LLZTO/IL/Li cells with aluminum (Al) and tungsten (W) serving as metallic ILs were shown to share a common mechanism for dendrite growth: both exhibit the same exponential dependence of j_c with the inverse of temperature $^1/_T$, as shown in Figure 4.11. [110] Such exponential relationship has been proposed to indicate dendrite growth stemming from voids. [104, 111] Furthermore, for both Al and W ILs, voids were observed at current densities of approximately $(^2/_3)\, j_c$, as shown in the cross-sectional scanning electron microscopy (SEM) images in Figure 4.12. The main difference between IL behavior is that W can withstand higher current densities than Al: at room temperature, cells with W have $j_c \approx 540\mu\text{A/cm}^2$, while cells with Al IL show $j_c \approx 300\mu\text{A/cm}^2$. This observation remains valid across the temperature range in experiments conducted by Raj *et al.* [110].

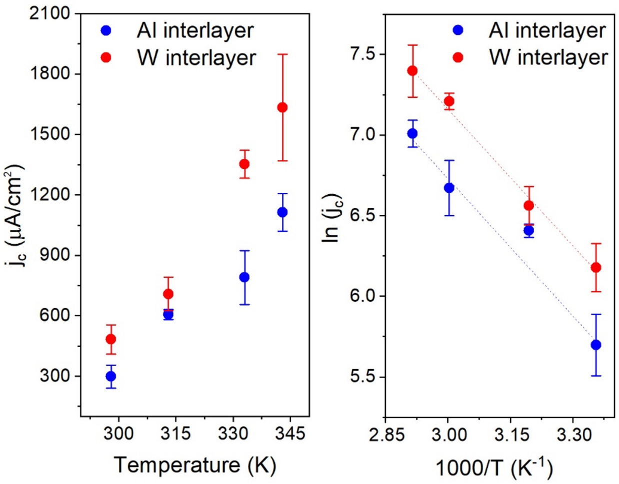

Figure 4.11: Comparison of j_c at temperatures of 25°C, 40°C, 60°C, and 70°C for cells with Al and W interlayers. [110]

The regular solution formalism developed in previous sections can in part help explain why W ILs are more resistant to voids than Al ones. Approximating Li/IL interfaces by Li-monolayers adsorbed on surfaces of W and Al, as represented in Figure 4.13, the thermodynamic parameters can be estimated with DFT

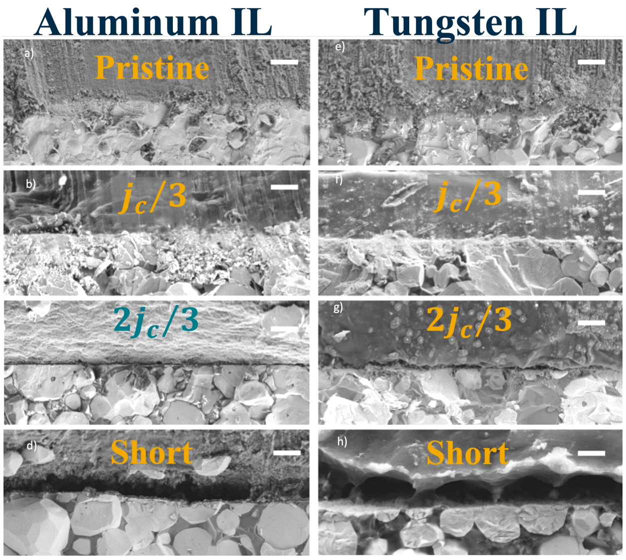

Figure 4.12: Cross-sectional SEM images of symmetric cells with Al and W interlayers. In all images, the bottom, rock-like portion, is the solid electrolyte (LLZTO), and the top material is the anode. Cells prior to cycling (as-prepared pristine) and those cycled at current densities of $j_c/3$ (of the respective IL) exhibit interfaces where the surfaces of anode and electrolyte are flush with each other. At current densities of $2j_c/3$, regions where the two materials are not in contact can be seen (black regions), indicating the existence of voids. For cells that were cycled until a short-circuit was detected, the interface is notably composed of large voids and dendritic structures. [110]

calculations. The results of this analysis are reported in Table 4.2. [110]

Facet		Surface energy [eV/Å^2]	Surface prevalence [%]	Phase-transition temperature [K]	Vacancy hopping barrier [eV]
Al	(100)	0.056	27.1	3,556	0.194
	(110)	0.061	3.9	0	0.168
	(111)	0.051	69.0	2,557	0.107
W	(100)	0.255	3.6	124	0.262
	(110)	0.203	78.2	0	0.190
	(111)	0.210	18.2	$> 10^5$	0.533

Table 4.2: Summary of computed thermodynamic and kinetic parameters for Al and W ILs. [110]

For both Al and W ILs, void formation is favorable in the (111) facet and unfavorable in the (110) facet. However, a thermodynamic driving force for vacancy congregation is present in the Al(100) facet, but not in W(100), for which $T_c \approx 120$K. Furthermore, the surface energies of these facets reveal another critical detail: the Al(110) facet, the only one capable of thermodynamically preventing voids in this IL material, has the highest surface energy and is thus expected to be the least common. In contrast, the W(110) facet has the lowest surface energy, and consequently is the most prevalent, as shown in the Wulff constructions displayed in Figure 4.14. These results are in accord with previous studies. [128, 129] However, as noted earlier, the W(110) facet does not favor vacancy congregation. Therefore, from a thermodynamic perspective, most Al

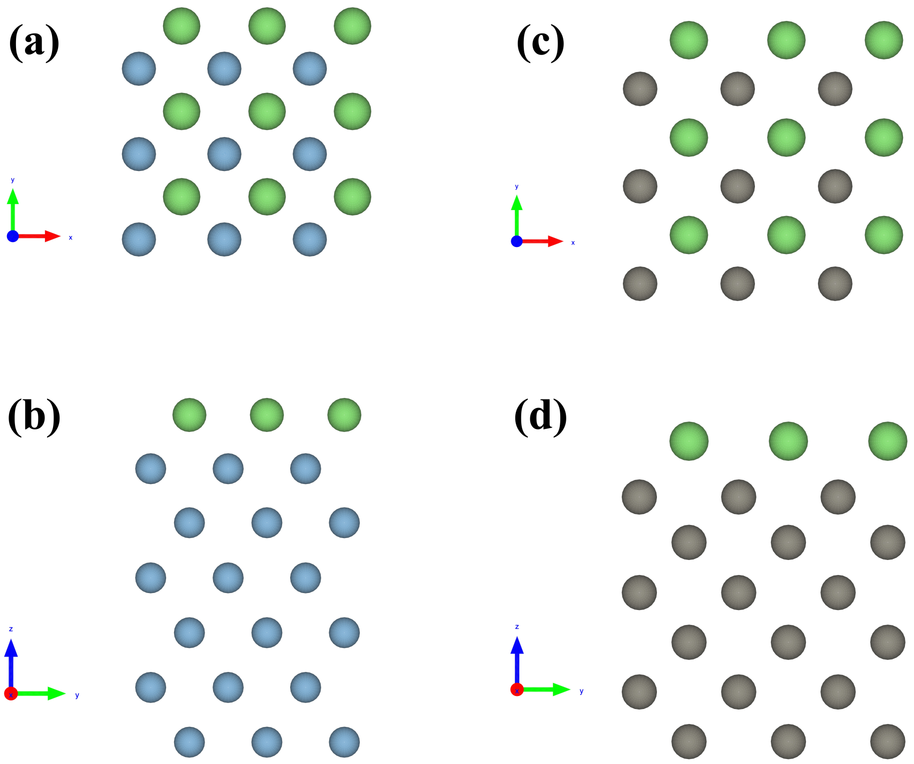

Figure 4.13: Al and W slabs used for computational calculations. Li monolayers on (100) surface facets of Al **(a, b)** and W **(c, d)**. Top views are shown in panels **(a)** and **(c)**, and side views are in panels **(b)** and **(d)**.

surface facets have a tendency towards void formation, whereas for W, most surface facets favor vacancy solubility.

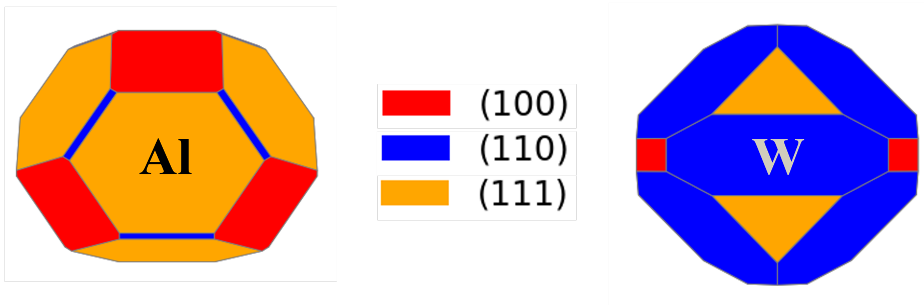

Figure 4.14: Wulff constructions of Al and W. In Al, nearly 70% of the surfaces are composed of (111) facets, while only 4% are composed of the desirable (110) facets. For W, however, nearly 80% of surfaces are (110) facets.

For a more holistic understanding of the void formation phenomenon, kinetic factors also need to be considered. Using the NEB algorithm, it is possible to compute the energetic barriers associated with Li vacancy hopping along the Li monolayer on the surfaces of IL materials (Table 4.2). For Al, the activation energy needed for vacancy motion is less than 0.2 eV for all facets, being as low as 0.1 eV for the (111) facet, which thermodynamically favors void formation. However, the (111) facet of W, which is the only facet in which void formation is thermodynamically favorable, has the highest vacancy hopping barrier of all facets, reaching a value of over 0.5 eV. Thus, for this facet, even though vacancy congregation is thermodynamically favorable, kinetic limitations on vacancy motion and the low surface prevalence potentially delay or even prevent void formation. [110]

In short, this theoretical and computational analysis demonstrates that, from both thermodynamic and kinetic perspectives, Al-based ILs have a higher likelihood of void nucleation and growth: the most common Al surface facets have a thermodynamic driving force that favors vacancy congregation. They also have a relatively low energetic barrier for vacancy motion. By contrast, the most prevalent W surface facet thermodynamically favors vacancy solubility, and the only facet with a thermodynamic tendency to form voids has the highest vacancy hopping barrier. Therefore, void formation on W surfaces is both thermodynamically and kinetically limited.

Interestingly, cells using Cr [130] and Mo [110] as IL materials have also demonstrated enhanced j_c values. Notably, Cr, Mo, and W are all group 6 metals with a body-centred cubic structure and low solubility for Li. This suggests a common mechanism that limits Li vacancy congregation on surfaces of these materials. The results in this section imply interface engineering with IL materials can enhance the stability of solid electrolytes against shorting due to dendrite growth, as void formation acts as a precursor for dendrite nucleation. [105, 131] Therefore, mitigating void growth could determine the success of Li plating in solid-state Li-ion batteries.

4.2 Summary and Conclusions

In this Chapter, we identify the need for a fundamental understanding of the void formation phenomena that is based on thermodynamics, rather than just kinetics. The regular solution model, a well-established thermodynamic modeling technique, is shown to provide valuable insight in studying the tendency for lithium vacancies to accumulate on the surface of lithium metal, at its interface with other materials. The importance of modeling explicit interfaces is also discussed in this Chapter: under a regular solution formalism, the interface between Li(110) and Li_2CO_3(001) is shown to be thermodynamically stable against the formation of voids, the main culprits behind dendrite nucleation. The same model is also shown to accurately capture experimental behavior of interlayer materials, which are easier to design than artificial SEIs. Such remarkable agreement between theoretical predictions and experimental results indicates that the methods developed within this Chapter can serve as a promising tool for the design of interfaces and interlayers of next-generation battery materials, allowing for faster computational screening of candidate materials.

Chapter 5

Tuning of Reactions through Interface Design

In Chapters 3 and 4, the impacts of interfaces on ionic transport phenomena and on the void formation mechanism were thoroughly investigated. Another critical process in batteries are reactions, of both electrochemical and chemical natures. Electrochemical reactions are the "driving force" of batteries: at every cycle, they happen on both electrodes. During discharge, they allow for electrons to perform useful work on an external circuit; during the charging process, they allow for storage of energy for use at a later point in time. Chemical reactions also play an important, though indirect role, in battery applications: the products of decomposition reactions can influence both performance as well as longevity of battery cells. In this Chapter, we study the effects of interfaces on reactions for two different battery applications, namely, anode-free lithium metal and next-generation alkaline batteries.

5.1 Investigating Reaction Rates at Low State-of-Charge Anode-free Li-metal Batteries

The maximum theoretical energy density of Li-metal batteries can only be reached in cases where there is no excess lithium. Battery cells that have no lithium in excess are called anode-free (AF) cells: they are assembled with a pre-lithiated cathode and without a Li-metal anode, which is fully formed in the first charging process. During discharge, anode-free Li-metal batteries (AFLMB) consume the entirety of their anode, leaving the current collector (CC) in direct contact with the electrolyte. AFLMBs are especially important for aviation applications, where reduction in total battery weight is crucial. [132, 3] However, for these applications, a high-power and a high-current outputs are required from the battery cells near the end of their discharge cycle, at a low state-of-charge (SOC). [3] At such low values of SOC, the Li-metal anode is almost completely consumed, and, thus, its interface with the CC material can have significant impacts on the rate of electrochemical reactions happening on the other side of the anode, at the Li-metal/eletrolyte interface. Computational screenings for CC materials have been performed with a focus on dendrite formation, [133] but it is also important to consider their effect on current output.

5.1.1 Modeling Electron Transfer Kinetics

The current output of a battery cell is directly related to the net redox reaction rate happening at the interfaces between electrodes and electrolyte. Since this reaction, shown in Expression 5.1, involves electron transfer between species, it is best modeled though a Marcus-Hush-Chidsey (MHC) based formalism. [134, 135]

$$\mathrm{Li_{(sol)}}^{+} + \mathrm{e}^{-} \underset{\mathrm{k_{ox}}}{\overset{\mathrm{k_{red}}}{\rightleftharpoons}} \mathrm{Li}^{0} \tag{5.1}$$

It has already been shown that the density of states (DOS) of the electrons at the electrode is important when considering the oxidation and reduction rates: [134, 135]

$$k_{ox}(\eta) \propto \frac{2\pi|H_{ox}|^2}{\hbar} \cdot \frac{\Delta z}{\sqrt{4\pi k_B T\lambda}} \int_{-\infty}^{\infty} \exp\left\{-\frac{\left[\lambda - |e|\eta + (E-\epsilon_F)\right]^2}{4k_B T\lambda}\right\} \left[1 - f_{FD}\left(E, \epsilon_F\right)\right] \mathrm{DOS}(E) dE \tag{5.2}$$

$$k_{red}(\eta) \propto \frac{2\pi|H_{red}|^2}{\hbar} \cdot \frac{\Delta z}{\sqrt{4\pi k_B T\lambda}} \int_{-\infty}^{\infty} \exp\left\{-\frac{\left[\lambda + |e|\eta - (E-\epsilon_F)\right]^2}{4k_B T\lambda}\right\} f_{FD}\left(E, \epsilon_F\right) \mathrm{DOS}(E) dE \tag{5.3}$$

Here, H is the electronic coupling element, which is assumed independent of the energy (but need not be, and can be incorporated into the integral term). The temperature is denoted by T, $\hbar$ is Planck's constant divided by 2π, k_B is Boltzmann's constant, Δz is the maximum distance from the surface of the electrode within which reactions are assumed to happen, λ is the Marcus' reorganization energy, η is the overpotential applied (defined as the difference between electrode and electrolyte potential), ϵ_F is the electrode Fermi level (assumed to be a metal), f_{FD} is the Fermi-Dirac distribution, and DOS represents the density of states. Assuming that, upon de-lithiation, the change in the Δz and $|H|^2$ terms are negligible (an assumption that may only break down when a bare CC is considered), we can focus on the simpler terms $k_{ox}^{\dagger}$ and $k_{red}^{\dagger}$:

$$k_{ox}^{\dagger}(\eta) = \frac{1}{\sqrt{4\pi k_B T\lambda}} \int_{-\infty}^{\infty} \exp\left\{-\frac{\left[\lambda - |e|\eta + (E-\epsilon_F)\right]^2}{4k_B T\lambda}\right\} \left[1 - f_{FD}\left(E, \epsilon_F\right)\right] \mathrm{DOS}(E) dE \tag{5.4}$$

$$k_{red}^{\dagger}(\eta) = \frac{1}{\sqrt{4\pi k_B T\lambda}} \int_{-\infty}^{\infty} \exp\left\{-\frac{\left[\lambda + |e|\eta - (E-\epsilon_F)\right]^2}{4k_B T\lambda}\right\} f_{FD}\left(E, \epsilon_F\right) \mathrm{DOS}(E) dE \tag{5.5}$$

An implicit assumption of the MHC model is that, at the reference steady-state conditions, the concentrations of reactants and products are equal. This means that, at $\eta = 0$, $k_{ox} = k_{red}$. Therefore, the net reaction rate can be easily computed as

$$k_{net}^{\dagger} = \left|k_{ox}^{\dagger} - k_{red}^{\dagger}\right| \tag{5.6}$$

5.1.2 Computational Screening of Current Collectors

Using previously defined criteria to select promising CC materials, [133] we considered a variety of CC candidates: chromium(Cr), copper (Cu), molybdenum (Mo), nickel (Ni), titanium (Ti), vanadium (V), tungsten (W), and zirconium (Zr). For each CC material, several low Miller index surface slabs were created. For each of these slab systems, lithium growth along different lithium crystallographic directions was simulated by sequential addition of lithium monolayers, from zero (0) to four (4) total Li layers, as illustrated in Figure 5.1. In all calculations, a reorganization energy value of $\lambda = 0.216$ V was used, in accordance with previous studies that compared MHC model predictions to experimental data. [134] The DOS of each interfacial structure was computed with DFT, using the BEEF-vdW functional. [74] However, since the redox reactions are taking place only at the interface between the Li-metal and the electrolyte, it would be incorrect to consider the total DOS (TDOS) of the system modeled. Here, we take a more conservative approach, and considered the DOS projected on atoms that are within the top 2.5Å of the interfacial system. This means we assume that, in general, only atoms in the top-most two layers can participate in the electron transfer reaction. This difference in projected DOS (PDOS) used for rate calculations can be seen in Figure 5.2.

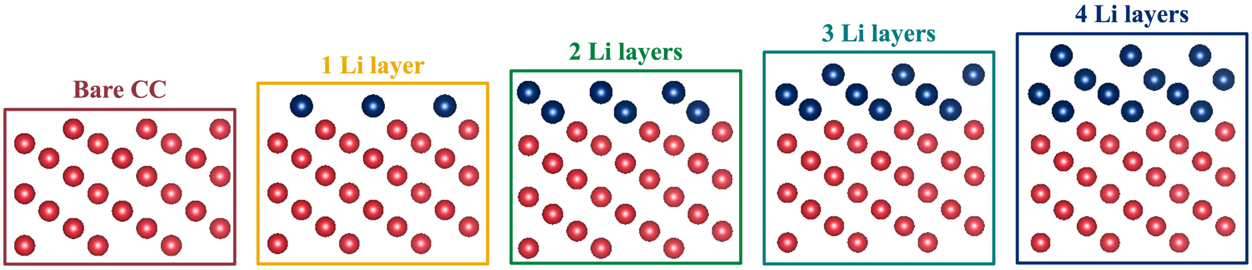

Figure 5.1: Schematic of structures used in DFT calculations of anode-free interfaces. Red circles denote current collector atoms, and blue circles correspond to Li atoms. In particular, the interfaces in this image represent lithium growth along the Li(100) direction on a Mo(111) substrate.

Since the metallic constituents of the CC material generally have more states (both occupied and unoccupied), this distinction can have appreciable impacts on the calculation of the total net reaction rate. Figure 5.3 shows the ratio between $k^{\dagger}_{net}$ computed with the top 2.5Å atoms' PDOS and that computed with the summation of the PDOS for all atoms in the V(110)/Li(100) system. For the bare CC system, there is no significant variation in this ratio, as the relevant PDOS has approximately the same profile as the TDOS. However, as more and more Li layers are introduced, the more the shape of the relevant PDOS changes compared to that of the TDOS, thus yielding considerable variations in the ratio of $k^{\dagger}_{net}$ values. For the V(110)/Li(100) interfaces with at least 2 Li layers, there is a spike in this ratio at an overpotential of about 1.25 V, which corresponds to a value of about 1 eV above the Fermi level, where there is a relative

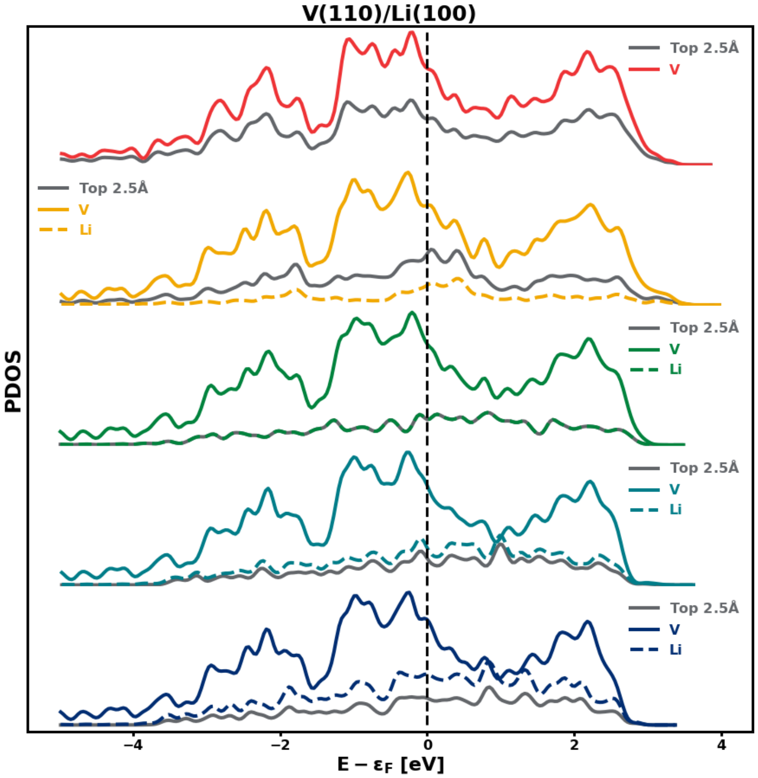

Figure 5.2: Representation of the PDOS from V(110)/Li(100) interface structure. Grey lines correspond to the PDOS of atoms on the top 2.5Å of the system. Dashed colored lines are the summation of the PDOS of Li atoms, and continuous colored lines are the summation of the PDOS of the CC atoms (V). Red lines correspond to the bare CC system, yellow, to that with a single Li monolayer, green, to a system with 2 Li layers, teal, to one with 3 Li layers, and blue, to one with 4 Li layers.

abundance of Li states but a depletion of V states.

The net reaction rates using the PDOS of the relevant atoms can then be calculated for every system. A diagram of how they vary with overpotential for a Mo(110)/Li(110) interface is displayed in Figure 5.4. Since we do not have access to parameters like $|H|$, it is more valuable to understand how $k^{\dagger}_{net}$ varies as a function of SOC. In order to do so, for each interface and for each value of overpotential η, the ratio $k^{\dagger}_{net}[\text{current system}]/k^{\dagger}_{net}[\text{4 Li layers}]$ is computed. Figure 5.5 displays how this ratio varies with overpotential for a V(110)/Li(110) interface.

In order to maintain high-current outages at low SOC during discharge, when the overpotential is positive ($\eta > 0$), it is necessary for the values of $k^{\dagger}_{net}$ to stay the same or increase as the number of Li layers decreases: as more Li atoms dissolve into the electrolyte as cations, it is needed to at least maintain the same rate of electron transfer. In this regard, Figure 5.5 demonstrates that V(110) is a good candidate: for relatively

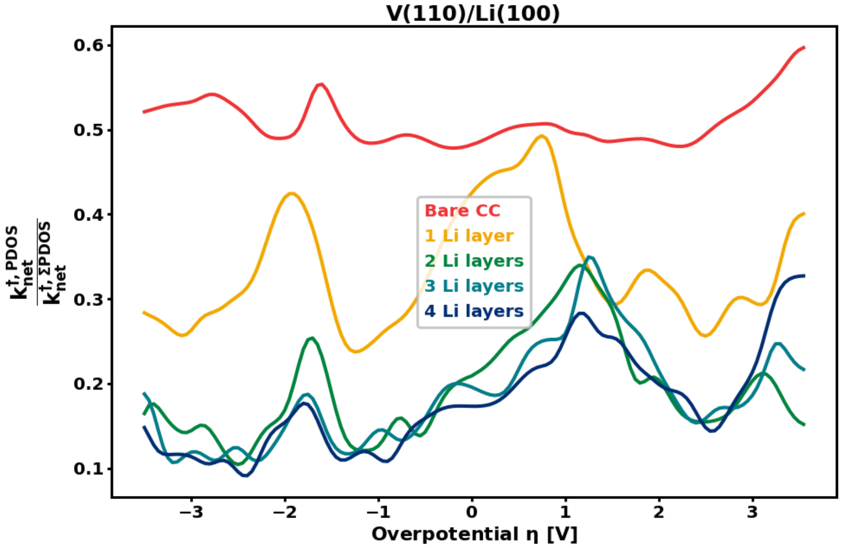

Figure 5.3: Ratio of $k_{net}^{\dagger}$ values calculated considering the PDOS of the top 2.5Å atoms and the summation of all PDOS for the V(110)/Li(100) interface.

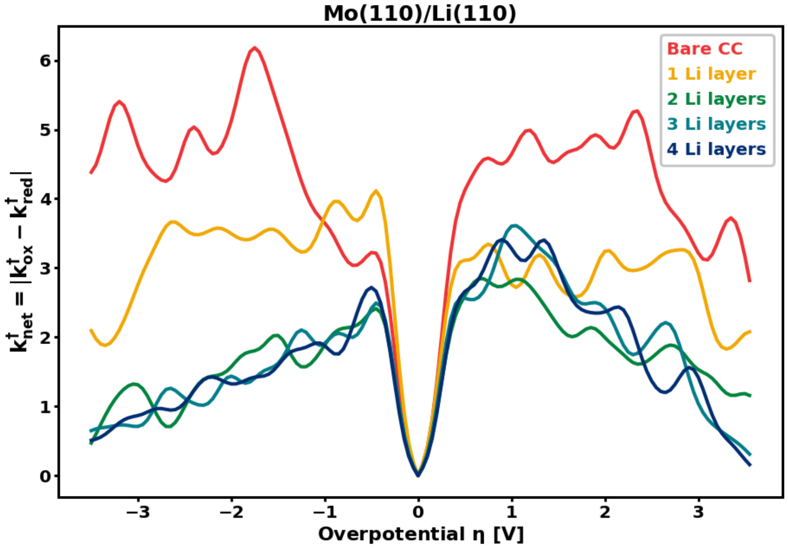

Figure 5.4: Variation of $k_{net}^{\dagger}$ with overpotential for a Mo(110)/Li(110) interface.

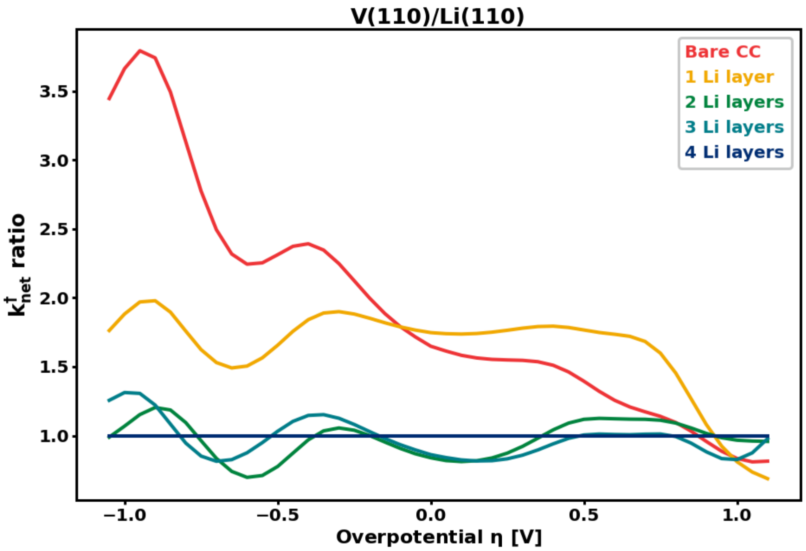

Figure 5.5: Ratio $k^{\dagger}_{net}[\text{current system}]/k^{\dagger}_{net}[\text{4 Li layers}]$ for a V(110)/Li(110) interface. Due to the abundance of V states, the bare CC and Li monolayer curves are above that for a structure with 4 Li layers. In this case, there is not much variation between structures with 2, 3, or 4 Li layers.

small positive $\eta \in [0, 0.85]$ V, the condition mentioned above is maintained — structures with at least 2 Li layers have similar $k^{\dagger}_{net}$, and structures with less than 2 Li layers have higher $k^{\dagger}_{net}$ values. This is not the case for all metals, however. As Figure 5.6(a) shows, for Cu, there is a reduction in $k^{\dagger}_{net}$ as more de-lithiation occurs. This can be explained by the fact that, near the Fermi level, the PDOS of the Cu(100) surface is relatively low, as shown in Figure 5.6(b).

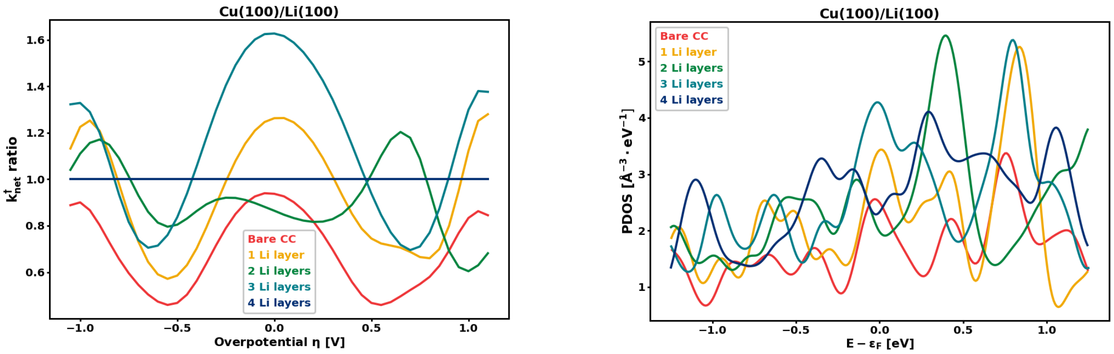

(a) Ratio of $k^{\dagger}_{net}$ values.

(b) PDOS near Fermi level.

Figure 5.6: Results for a Cu(100)/Li(100) interfacial system. **(a)** Ratio of $k^{\dagger}_{net}$ as a function of overpotential. **(b)** Sum of relevant PDOS near the Fermi level for structures with different numbers of Li layers. The relatively low PDOS for a bare Cu(100) facet is responsible for a decrease of $k^{\dagger}_{net}$ as de-lithiation occurs.

Besides electron transfer, another important part of the de-lithiation process is the lithium desorption from the surface of the electrode. To investigate possible relationships between these two processes, we can calculate the layer adsorption energy per Li atom for the interfacial structures with less than 4 Li layers as follows:

$$\Delta g_{ads}^{(n)} = \frac{E^{(n+1)} - E^{(n)}}{N_{[\mathrm{Li}]}^{(n+1)} - N_{[\mathrm{Li}]}^{(n)}} - \mu_{\mathrm{Li}}, \tag{5.7}$$

where n is the number of Li layers, $E^{(n)}$ is the energy of a system with n Li layers, $N_{[\mathrm{Li}]}^{(n)}$ is the number of lithium atoms in a structure with n Li layers, and μ_{Li} is the Li reference energy. With this, we can evaluate any possible correlation between Δg_{ads} and the ratio of $k_{net}^{\dagger}$ values, as shown in Figure 5.7.

Under this formalism, a negative value of Δg_{ads} indicates that, relative to a bulk Li reservoir, the interface has a lower chemical potential for Li. Therefore, negative values of Δg_{ads} correspond to a thermodynamic driving force for lithium deposition, while positive values denote a thermodynamic driving force for lithium stripping. As made clear by all plots in Figure 5.7, in general, bare CC surfaces favor lithium plating. As more layers are added, this effect diminishes, and, in some cases, might even switch signs and favor (though very slightly) lithium electropolishing instead. The results presented in Figures 5.7(a), 5.7(c), and 5.7(e) show that, for $\eta \leq 0$, reduction becomes more favorable as SOC values go down from both a thermodynamic and an electrochemical kinetic perspectives. However, for high-power output applications, the focus is on oxidation, which happens when $\eta \geq 0$. For oxidation-dominated cases, a trade-off between thermodynamics and kinetic can appear, not too dissimilar from a previous study on CC screening. [133] In a W(111)/Li(100) interface, as the number of Li layers in the structure goes down, $k_{net}^{\dagger}$ does not change considerably, but the values of Δg_{ads} decrease, reaching values of -1 eV per atom, as shown in Figure 5.7(d). Therefore, for this system, adsorption can lead to slow reactions. In this aspect, the V(110)/Li(110) interface (Figure 5.7(d)) appears more promising: although the values of the ratio between $k_{net}^{\dagger}$ are moderate, the associated adsorption energies are much closer to 0, reaching a minimum of -0.25 eV per Li atom. Therefore, while similarly to the W(111)/Li(100) case, there is not much difference in the electron transfer kinetics as SOC lowers, the V(110)/Li(110) would not have to overcome a steep thermodynamic barrier. Another interesting possibility is shown in Figure 5.7(f): for the Ti(111)/Li(111) system, as the Li loading shrinks, there is an increase in both the electron transfer rates as well as in the thermodynamic driving force opposing Li deposition. It is not immediately evident whether this trade-off is favorable for fast Li stripping reactions, and a more in-depth investigation between the thermodynamics and kinetics of SOC dependent electrochemical reactions at the interfaces between electrolytes and both current collectors and electrodes is necessary to further unravel optimal materials design for high performance battery cells.

In particular, for a full comprehension of current output at low SOC, several parts are needed. In this work, only the anode side was considered, and, as described above, not fully: the relationship between

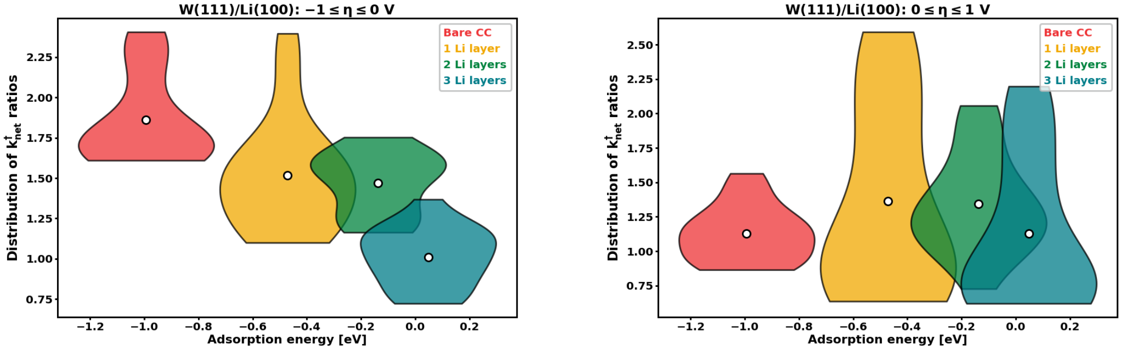

(a) Relationship between reduction-dominated $k^{\dagger}_{net}$ ratios and Δg_{ads} for W(111)/Li(100)

(b) Relationship between oxidation-dominated $k^{\dagger}_{net}$ ratios and Δg_{ads} for W(111)/Li(100)

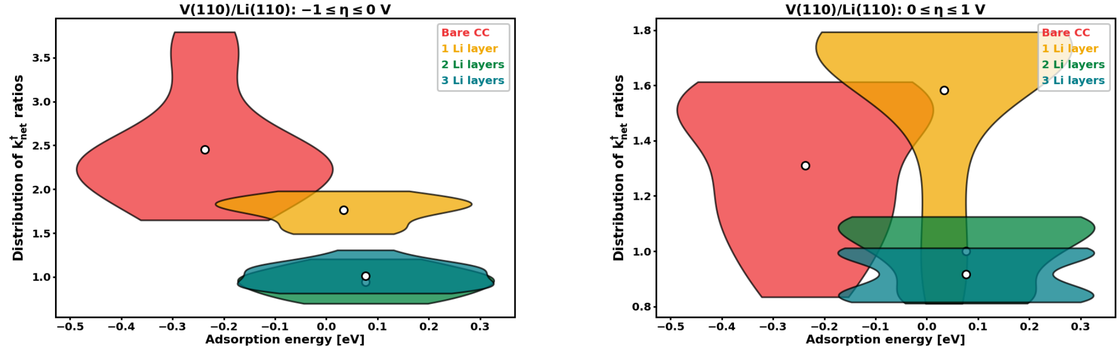

(c) Relationship between reduction-dominated $k^{\dagger}_{net}$ ratios and Δg_{ads} for V(110)/Li(110)

(d) Relationship between oxidation-dominated $k^{\dagger}_{net}$ ratios and Δg_{ads} for V(110)/Li(110)

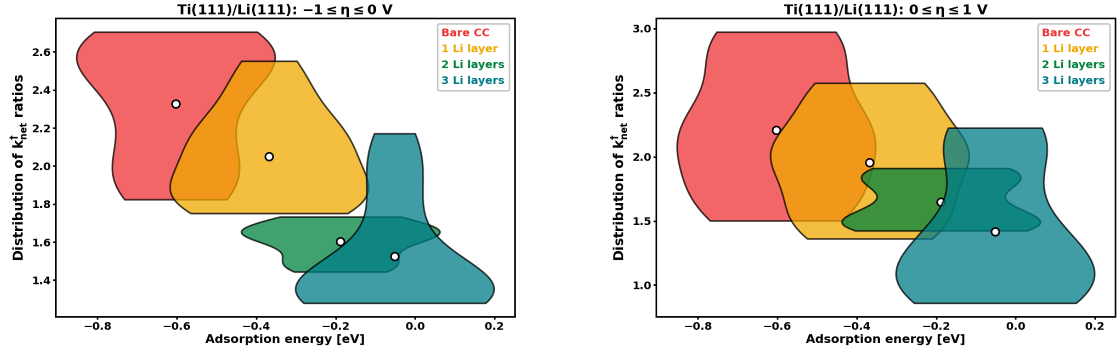

(e) Relationship between reduction-dominated $k^{\dagger}_{net}$ ratios and Δg_{ads} for Ti(111)/Li(111)

(f) Relationship between oxidation-dominated $k^{\dagger}_{net}$ ratios and Δg_{ads} for Ti(111)/Li(111)

Figure 5.7: Distribution of $k^{\dagger}_{net}$ ratios compared to adsorption energy Δg_{ads} for several of the interfaces considered, for negative and positive values of the overpotential η. Positive η denotes a reaction dominated by oxidation, while negative η corresponds to a reduction-dominated reaction.

adsorption thermodynamics, electron transfer kinetics, and electrolyte solvation structure needs to be better understood. The same can be said about electrochemical reactions on the surface of the cathode: while there have been numerous studies on the thermodynamics of Li intercalation and bulk diffusion, phenomena at the cathode/electrolyte interface remain elusive from both a thermodynamic and kinetic perspective, and should be investigated under the same light as for the anode.

5.2 Empowering Aqueous Alkaline Batteries Through Interface Design

While Li-ion based batteries are a staple in energy storage, as well as constitute the most promising avenue for electrification of more challenging sectors such as aviation, alkaline cells still account for 80% of all batteries manufactured in the US. [136] Nickel hydroxide $\mathrm{Ni(OH)_2}$ is widely used as the positive electrode, with the following half-reaction:

$$\mathrm{Ni(OH)_2 + OH^-(aq) \rightleftharpoons NiOOH + H_2O + e^-}$$

Layered 2D materials similar to β-$\mathrm{Ni(OH)_2}$ are particularly attractive due to their crystal structures having large surface areas, allowing for more contact with the aqueous electrolyte and thus enhancing the total current output of the battery. However, further development of alkaline batteries with this class of materials is hampered by their characteristic low active mass-loading ratio, which lowers their real storage capacity. In order to increase the overall volume energy density of these structures, the use of ultra-thick halogen-doped β-$\mathrm{Ni(OH)_2}$ structures on a conducting substrate has been proposed, as shown in Figure 5.8. These new structures $\mathrm{NiM}_x\mathrm{(OH)}_{2-x}$ (M=F, Cl, Br, or I) were shown to increase the total mass loading of the traditional β-$\mathrm{Ni(OH)_2}$ by an order of magnitude.

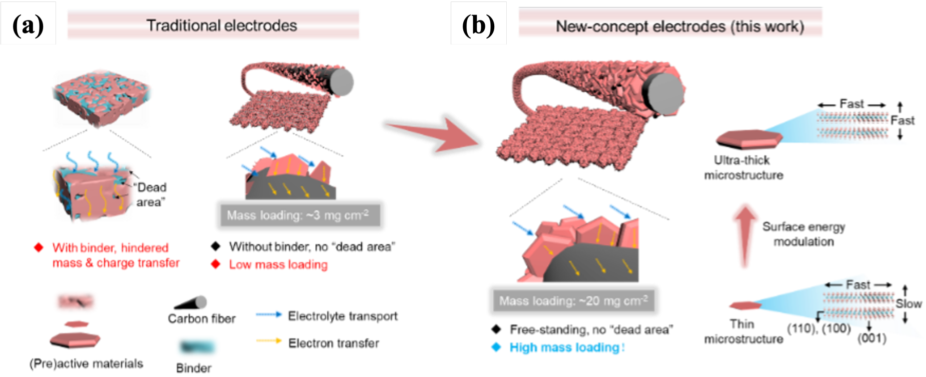

Figure 5.8: Schematic illustration for **(a)** the traditional and **(b)** the new-concept electrodes

To understand how halogen doping can aid in particle design, DFT calculations were performed on bulk and surface structures of several $\mathrm{NiM}_x\mathrm{(OH)}_{2-x}$ materials. The plot of surface energies shown in Figure 5.9 helps explain why fluorine-doping generates thicker crystals: for pure β-$\mathrm{Ni(OH)_2}$, the surface energy of the

(001) facet is negligible (its negative value, while nonphysical, can be explained by a variety of factors, such as choice of functional, Hubbard correction value, size of the simulated structure, among others), and thus its crystals develop needle-like thin structures; for F-doped systems, the energy of this facet is the lowest, but still considerable, and thus crystals grow as thick disk-like structures.

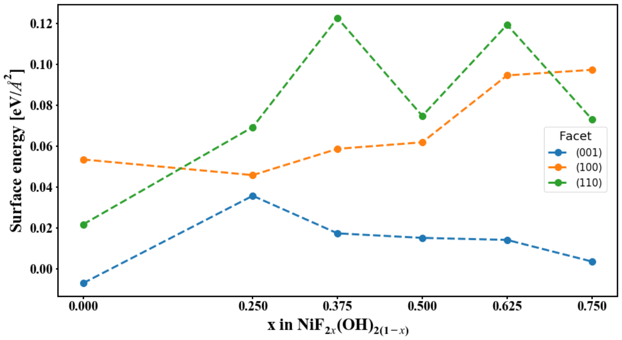

Figure 5.9: Calculated surface energies of NiF$_x$(OH)$_{2-x}$ for the (001), (100), and (110) facets.

An important caveat to note, however, is that structure tuning through doping does not come without downsides. Doping of β-Ni(OH)$_2$ with halogens other than F, namely, chlorine (Cl), bromine (Br), and iodine (I), is limited. A common decomposition reaction for these compounds is given by:

$$\mathrm{NiM_{2x}(OH)_{2(1-x)}} \longrightarrow \mathrm{(1\text{-}x)Ni(OH)_2 + xNiM_2}$$

When the enthalpy change (ΔH) associated with this reaction is positive, the composition NiM$_x$(OH)$_{2-x}$ is stable. However, negative values of ΔH indicate an unstable product that has a thermodynamic driving force to decompose. For F-dopant, a wide range of doping concentrations yields stable materials. However, for the other halogens, only small doping concentrations are stable, and higher doping concentrations lead to decomposition of the doped nickel hydroxide, as shown in Figure 5.10.

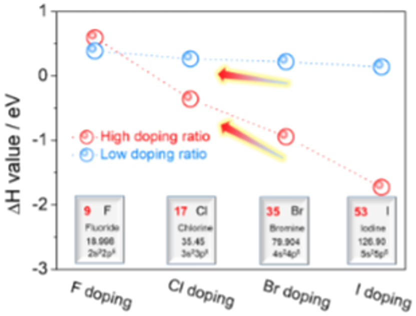

Figure 5.10: Decomposition enthalpies for halogen doped β-Ni(OH)$_2$ Low doping ratios correspond to $x = 1/12$, and high ratios correspond to $x = 2/3$. Units of ΔH reported in eV per Ni atom involved in the decomposition reaction.

This work emphasizes the "double-edged sword" character of interface engineering. While *a priori* halogen doping appears to help modify the structure of β-Ni(OH)$_2$ in a way to improve its mass loading ratio and thus total capacity thanks to doping-dependant surface energies, limitations regarding stability of newly made materials can pose challenging obstacles for property optimization. As alluded to in the introduction to Chapter 3, in order to avoid drawbacks and to perfect interface design, further investigations similar to those presented in this Chapter are required.

5.3 Summary and Conclusions

This Chapter explores the effects of interfaces on kinetics of electrochemical reactions, with a focus on the performance of different current collectors at a low state-of-charge anode-free battery configuration. The methods developed can also be used to understand faceting control in anode-free batteries, as lithium can grow in different directions at different rates during the plating process. Incorporation of adsorption-desorption kinetics into the model would provide a more comprehensive approach for studying overall plating and stripping kinetics. Furthermore, interface engineering is also shown to have significant importance for other applications beyond Li-metal and Li-ion batteries, including state-of-the-art alkaline batteries and supercapacitors. However, it is also demonstrated that engineering of interfaces can have unexpected shortcomings, thus emphasizing that interface design must be performed in a cautious and exhaustive fashion.

Chapter 6

Conclusion and Outlook

The topics covered in this thesis emphasize the importance of physical phenomena on lower dimensional structures, ranging from 2D atomic monolayers to 2.5D interfaces. From opening possibilities in the fields of photovoltaics to being a critical enabler of Li-metal batteries, such material structures serve as confirmation of Nobel laureate Richard Feynman's statement that "there is plenty of room at the bottom." This Chapter briefly summarizes the conclusions from other chapters, as well as discusses ways in which the work presented here can aid in further exploring materials at the nano-scale.

6.1 The Growing Role of Machine Learning in Materials Science

In Appendix B, we evaluated the accuracy and precision of CGCNNs for predicting properties of 2D atomic monolayers for applications in photovoltaics and in creating of mechanically robust composites. CGCNNs were shown to be less computationally expensive than traditional *ab-initio* methods while retaining the same level of accuracy. Design principles extracted from model predictions are able to both capture well-accepted field-expertise and to identify new promising avenues for material development. This work is just one example of how machine learning (ML) methods have demonstrated their usefulness in materials science. Here, we discuss the promise of ML methods and how to leverage them for several applications.

6.1.1 Common Machine Learning Applications

While ML could one day help the scientific community discover "new physics," that would happen first in an indirect manner: by significantly increasing the speed at which high-accuracy calculations can be performed, ML methods allow scientists to collect and analyse data at a much faster pace than previously possible. There are two main ways in which ML methods are currently employed in computational materials science.

The first is as a property predictor: given a collection of materials, trained ML models can predict, for each structure, several properties of interest at a negligible time compared to traditional first-principles calculations. While this application of ML is very useful at predicting properties, such as stiffness tensor components, that require several DFT calculations, one of its main shortcomings is the fact that it needs relaxed structures as inputs: *ab-initio* relaxation is the main bottleneck for property prediction. This challenge can also be overcome with ML methods, such as Bayesian optimization. [137]

The second most common application of ML can also help tackle this issue, but tends to be more limited and not adequate for single-model relaxation of materials with high variance in composition and structure. Instead, its principal use is to investigate structures whose sizes make them intractable for first-principles calculations. ML interatomic potentials (MLIAPs) have been demonstrated to reach DFT-level accuracy when predicting energies and forces between atoms; a very recent example being a graph-based universal neural network capable of relaxing even hypothetical crystals and predicting their relative stability. [138] Once trained, the computational cost of MLIAPs scales linearly with the number of atoms (N) in the system under investigation, while first-principles methods usually scale as $\mathcal{O}(N^3)$. Therefore, MLIAPs can reach high-levels of accuracy at unprecedented scales.

6.2 The Importance of Interfaces

In Chapters 3, 4, and 5, the impact of several different types of interfaces on material performance was investigated. We demonstrated how to engineer interfaces in a polymer composite in a way to prevent dendrite growth, explored the enhanced ionic conductivity caused by SEI interfaces, predicted how interfaces between Li and solid ion conductors can influence surface morphology and void formation, evaluated the performance of several current collector materials from a kinetics perspective, and studied surface and particle shape modulation through doping. The importance of better understanding such types of structures is undeniable: it is a requirement of the more sophisticated interface design needed to ensure drawback-free optimal material performance.

6.2.1 Grain Boundaries: A Challenging Mystery

Most crystalline materials, including solid electrolytes, are polycrystalline — they are structured as a collection of crystals/grains at different orientations. The interfaces between two crystals of the same material is called a grain boundary (GB), and it is known to significantly dictate macroscale material properties. For example, thanks to the ability of GBS of pinning dislocations, materials with smaller grain sizes, and thus, denser GB networks, have a higher yield stress, a phenomenon described by the Hall-Petch relationship.

In battery materials, the role of GBs is not as clear, and active investigation of these structures is still ongoing. For instance, GBs have been shown to influence dendrite growth, but the mechanism through which this happens is unknown: some argue it is through mechanics [139], others claim it is through electron leakage. [140] GBs can also impact ion diffusivity and concentration, [139] but these effects can vary depending on material and GB structure.

From a computational standpoint, a variety of reasons make GBs particularly challenging to investigate. First, in any material, a variety of different GB structures can be present, from tilt to twist to neither of these, from coincidence site lattices to random, from values of Σ ranging from 3 to unbounded numbers. Additionally, in a single GB, even for single element materials, there can be an assortment of different phases (complexions) present, which can be ordered or disordered, or have different structures and compositions, to name a few. [121] Moreover, for proper computational modeling of GBs, the atomic structures needed are much larger than bulk unit cells, thus rendering first-principles methods usually not viable for this task.

As discussed in Section 6.1.1, methods powered by ML, in particular MLIAPs, can be a promising solution to this problem. They can provide *ab-initio* accuracy at the scales that are relevant for the study and understanding of GB structures and complexions, as well as other relevant properties, such as species diffusivity coefficients, mechanical response and GB mobility, to name a few.

6.2.2 Dynamics of Point Defects

Point defects play an essential part in battery operation. The concentration of charged point defects is especially susceptible to the Fermi level of the material and to the spatially varying Galvani potential, as shown in Appendix I. As discussed in Section 3.2, their dynamics and diffusion pathways can be significantly impacted by interfaces, especially in inhomogeneous battery components made up of small grains of sizes no larger than a couple of nanometers. This is in part explained by the space-charge layers in the vicinity of interfaces between different materials. In order to better engineer artificial SEI layers to enhance ionic conductivity, it is necessary to understand how this 3D material mosaic can affect carrier concentration. This could be done by combining first-principles calculations with meso-scale modeling, as discussed at length in Section I.2.

6.3 Other Low Dimensional Structures

Chapter 2 and Appendix B highlight the relevance of low dimensional (2-2.5D) materials for several applications. Modern sophisticated experimental techniques, capable of isolating atomic monolayers and building structures with a pre-defined layer count, have opened completely new possibilities for material design. In the past, these materials have been mostly neglected due to their experimental infeasibility. Therefore, there is much to study and understand. Calculations of all possible Moiré patterns and heterostructure combinations cannot be accomplished by traditional techniques, due to both the sizes of twisted structures as well as to the lack of classical force fields that have been fine-tuned to this particular application. Once again, ML methods have the opportunity to really make an impact in this field.

Appendix A

List of Publications

The † symbol indicates co-first authorship.

Google Scholar link

- C. Fu†, **V. Venturi**†, J. Kim†, Z. Ahmad, A. W. Ells, V. Viswanathan, B. A. Helms. *Universal Chemomechanical Design Rules for Solid-Ion Conductors to Prevent Dendrite Formation in Lithium Metal Batteries*, Nature Materials (2020) DOI: 10.1038/s41563-020-0655-2 [8]
- **V. Venturi**, H. L. Parks, Z. Ahmad, V. Viswanathan *Machine learning enabled discovery of application dependent design principles for two-dimensional materials*, Machine Learning: Science and Technology (2020) DOI: 10.1088/2632-2153/aba002 [141]
- Z. Ahmad, **V. Venturi**, H. Hafiz, V. Viswanathan. *Interfaces in Solid Electrolyte Interphase: Implications for Lithium-Ion Batteries*, The Journal of Physical Chemistry C (2021) DOI: 10.1021/acs.jpcc.1c00867 [100]
- **V. Venturi**, V. Viswanathan *Modeling of Lithium Intercalation in Twisted Bilayer Graphene*, Journal of The Electrochemical Society (2021) DOI: 10.1149/1945-7111/ac1315 [142]
- Z. Ahmad, **V. Venturi**, S. Sripad, V. Viswanathan, *Chemomechanics: friend or foe of the 'AND problem' of solid-state batteries?*, Current Opinion in Solid State & Materials Science (2021) DOI: 10.1016/j.cossms.2022.101002 [51]
- **V. Venturi**, V. Viswanathan. *Thermodynamic Analysis of Initial Steps for Void Formation at Lithium/ Solid Electrolyte Interphase Interfaces* ACS Energy Letters (2022) DOI: 10.1021/acsenergylett.2c00550 [122]

- V. Raj, **V. Venturi**, V. R Kankanallu, B. Kuiri, V. Viswanathan, N. P. B. Aetukuri, *Direct correlation between void formation and lithium dendrite growth in solid-state electrolytes with interlayers*, Nature Materials (2022) DOI: 10.1038/s41563-022-01264-8 [110]

Appendix B

Design Rules for Two-dimensional Materials

Owing to their unique electronic, mechanical, chemical, optoelectronic and magnetic properties, [52, 53, 54, 55] two-dimensional (2D) materials have become an enticing candidate for use in energy applications. For instance, thanks to exfoliation, 2D materials provide a new way of tuning properties, such as band gaps, of their 3D counterparts, [143] as is the case with 2D perovskites, which have shown great promise for photovoltaics applications. [144] Moreover, MXenes have been investigated for applications in water purification, battery electrodes, catalysis, lubrication, among others. [145, 146, 147] Due to their relative mechanical strength compared to other 2D materials, MXenes also show potential for uses in protective coatings, composites and membranes. [148] A schematic of some of these applications is illustrated in Figure B.1.

The innumerable different 2D structure prototypes and atom combinations to populate their sites mean that a purely conventional exploratory computational approach based on expensive first-principles calculations is unlikely to identify materials for desired applications in a time-efficient manner. For example, MXenes have the form $\mathrm{M}_{n+1}\,\mathrm{X}_n\,\mathrm{T}_x$, where M indicates a metal, X is either carbon (C) or nitrogen (N), and T are different possible terminations, such as fluorine (F), oxygen (O), or a hydroxil group (OH). In a case where there are m different metal possibilities and t different termination group possibilities, the amount of different theoretical structures explodes combinatorially, with an upper bound of $\sim 2^n m^{n+1} t^x$. For instance, the number of MXene structures with only two layers of either C or N ($n = 2$), with three termination groups ($t = 3$) and 10 metals ($m = 10$) to choose from is of $35,000$, but, by simply doubling the amount of metallic elements to consider ($m = 20$), this number becomes $280,000$. Fortunately, thanks to the recent generation of substantial volumes of materials data, [149] data-driven techniques, such as machine-learning (ML), offer a new avenue to deal with this problem. Such methods have demonstrated to be capable of advancing our fundamental understanding of materials [150], as well as to perform large scale computational

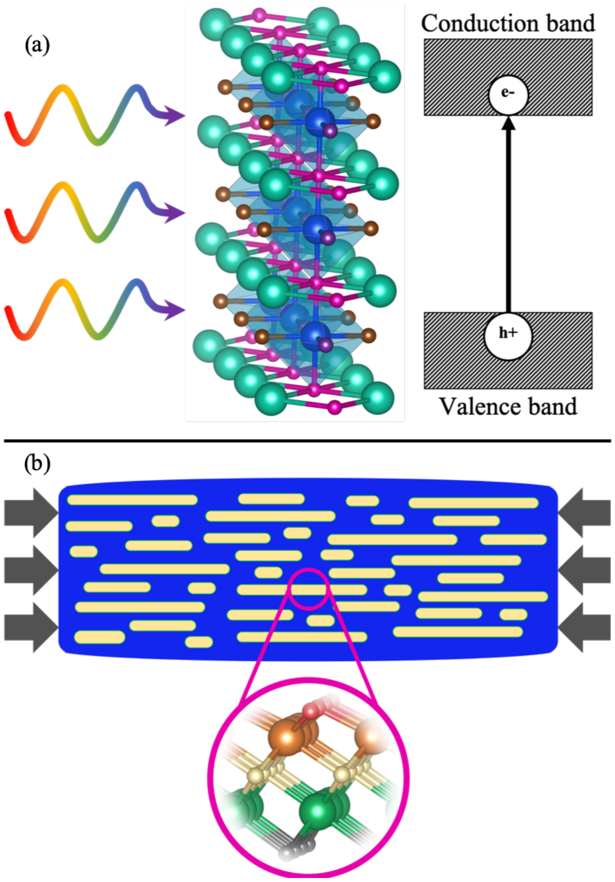

Figure B.1: Illustration of 2D materials applications: (a) 2D perovskites whose bandgaps can be the range of 1.5-3 eV have been demonstrating promise in the field of photovoltaics, ; (b) MXenes can be used in composites to increase their mechanical strength, here indicated by the material's response to an external mechanical stress (in grey). [141]

screening through the development of accurate structure-property relationships. [151, 152, 153, 154, 155] ML methods are able to circumvent the use of first-principles calculations and thus reduce the computational costs of traditionally time-consuming material discovery and optimization. [156, 157, 158].

Graph convolution based machine learning models have shown promising generalization capability for predicting the properties of crystals and molecules. [141, 154, 159, 160, 161] These methods encode the structure of a material as a graph based on the position and coordination of atoms, thus bypassing the use of carefully engineered structural features, and enabling them to be used in a variety of applications. In this Appendix, crystal graph convolutional neural networks (CGCNN) are extended to study materials with planar periodicity. Using 100 different, randomly generated training sets, an ensemble of CGCNN models were trained to predict thermodynamic, mechanical, and electronic properties. The ensemble of neural networks has errors comparable to those from highly accurate first-principles calculations, such as density functional theory (DFT), as discussed in Appendix C. This ensemble is used to survey $\sim 45,000$ 2D monolayer materials with focus on mechanically strong MXenes ($c_{11}, c_{22} \geq 175$ N/m) and on perovskites whose band gaps fall within an acceptable range ($[1.5, 3]$ eV) for solar cell applications. These two applications are quite different from each other, further proving the generalizability of CGCNN model predictions.

B.1 Machine Learning Methods

B.1.1 Databases

Computational data and material structures used in this work originated from (1) the Computational 2D Materials Database [162] (C2DB), (2) a database of hybrid organic-inorganic perovskites generated by Kim *et al.* [163] (HOIP), (3) a database of cubic perovskites generated by Castelli *et al.* [164] (Castelli), and (4) a database of 2D MXenes generated by Rajan *et al.* [165] (aNANt). All four databases contain results from DFT calculations, but training of the CGCNN models was performed using only values from the C2DB database. The structures from the other three databases were used in the screening process after model training.

As of August 2019, C2DB consisted of over 3500 structural, thermodynamic, elastic, electronic, magnetic, and optical properties calculated using density functional theory (DFT), coupled with the Perdew, Burke, and Ernzerhof (PBE) exchange correlation functional [94] in the projector augmented wave (PAW) code GPAW. [73] The material structures were combinatorially generated from a series of prototypes that differ in space group, stoichiometry, and thickness. Examples of such prototypes include BN (space group P$\bar{3}$m2), BiI_3 (P$\bar{3}$m1), or PbSe (P4/mmm). The most important properties for screening 2D MXenes and perovskites are the heat of formation; bandgap; and the c_{11}, c_{12}, and c_{22} components of the elastic tensor. The CGCNN models trained on C2DB data were used to predict these properties of approximately $20,000$ 2D perovskites and $25,000$ 2D MXenes. Perovskite structures (ABX_3) were taken from the HOIP dataset [163] (1,346 structures) and the Castelli database [164] (19,000 cubic structures), all generated combinatorially. A total of 135 prototypes, obtained using the minima-hopping method outlined by Goedecker [166], were optimized using a combination of molecular dynamics simulations and DFT calculations, coupled with the vdW-DF2 exchange correlation functional [167] as implemented in the Vienna *Ab Initio* Simulation Package(VASP) [168], and then used to create the HOIP database. For these ABX_3 perovskite prototypes, A is one of 16 organic cations, B is one of {Ge, Pb, Sn}, and X is one of {F, Cl, Br, I}. The cubic perovskites in the Castelli database have A and B as each one of 52 different metals and X_3 as one of 7 different anion groups. They were optimized using the RPBE exchange correlation functional [169] as implemented in GPAW. [73] Both HOIP and Castelli databases contain only 3D bulk structures, which were computationally exfoliated to create corresponding (001) monolayers used for screening. The 2D MXenes structures are taken from the aNANt database [165], which contains 23,870 combinatorially-generated five-layer MXene structures of the form T-M-X-M'-T' (that is, the T/T' occupy the outermost layers of the structure), where T and T' are each one of 14 termination functional groups, M and M' are each one of 11 early transition metals, and X is one of {C, N}. These structures were optimized using the PBE exchange correlation functional [94] in VASP. [168]

B.1.2 Model Training

Screening of the $\sim 20,000$ perovskites and $\sim 24,000$ MXenes 2D monolayer structures, as well as discovery of the underlying design principles for their respective applications, requires a technique that can calculate properties with the accuracy levels of DFT, but at a much lower computational cost. The Crystal Graph Convolutional Neural Network (CGCNN) framework [159] was used as a surrogate technique for predicting material properties. This method has the accuracy of DFT calculations (discussed in Appendix C) but at a fraction of the associated computational cost: while computing the c_{11} coefficient for one structure using DFT can take up to 500 CPU hours, trained CGCNNs can predict the same property for roughly 25,000 structures in under 20 CPU minutes. This framework has been successfully used in several applications, from selecting solid electrolyte materials [154] to screening catalysts [170]. The foundation of the CGCNN is an undirected multigraph representation of the crystal structure, in which nodes represent atoms by their respective features, and edges encode interatomic bond distances [159]. Iterative convolution layers update atomic feature vectors based on neighbor information, as further explained in Appendix E. A simplified schematic of a CGCNN can be seen in Figure B.2.

After optimization (discussed in Appendix D), ensembles of 100 CGCNN models, each trained on a random set of 70% of the C2DB data, were used to predict, for all perovskites and MXenes, the properties of interest: band gap, $\log(c_{11})$, $\log(c_{22})$, c_{12}, conduction band minimum (CBM), valence band maximum (VBM), and heat of formation (H_{form}).

B.2 Results and Discussion

B.2.1 Structure Screening

Evaluation of the accuracy of the ensemble of 100 models was done by predicting the properties of the all the structures in the C2DB database. The results for the ensemble predictions of some of the main properties is shown in the parity plots shown in Figure B.3. An analysis of uncertainty quantification of the models, as well as an outlier investigation, can be found in Appendix C.

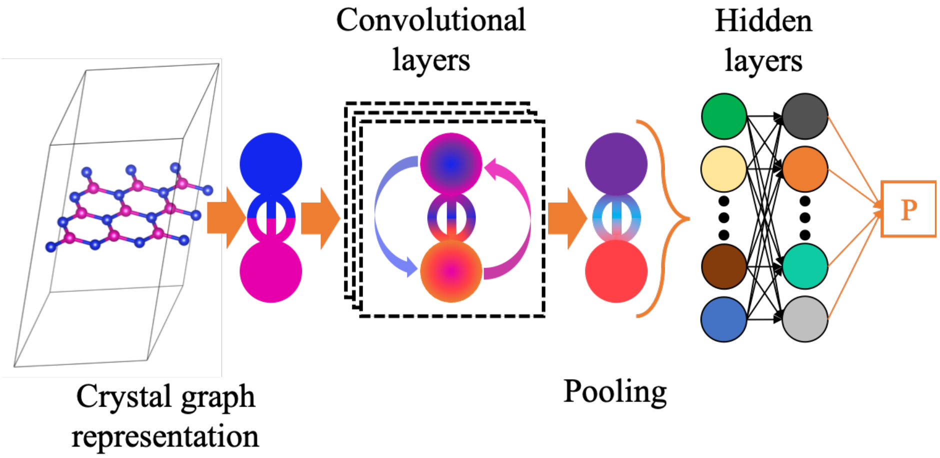

Figure B.2: A simple representation of the CGCNN architecture. The atomic structure is first converted into its crystal graph representation. This graph is then passed as input for the convolutional layers, where the atomic feature vectors are updated based on neighbor information and bond lengths. Next, a pooling function is employed to produce an overall vector representation of the crystal, guaranteeing invariance with respect to number of primitive unit cells used in the creation of the original structure. Finally, a set of fully connected hidden layers maps the simplified vector-represented crystal structure to the property of interest.

As discussed previously, MXenes were surveyed in search of structures that are strong mechanically, with both $c_{11}, c_{22} \geq 175$ N/m, thus exceeding those of graphene oxide [148], while perovskites were scanned for bandgaps that fall in the range $[1.5, 3]$ eV, appropriate for solar cell applications. Since these structures must be stable, as well as synthesizable, the filtering procedure included the additional requirement that $H_{form} \leq -2$ eV/atom for MXenes and inorganic perovskites, and $H_{form} \leq -0.5$ eV/atom for hybrid organic-inorganic perovskites. The difference in treatment for the latter stems from the fact that hybrid perovskites are known to be relatively less stable than their inorganic counterparts [171]. The threshold values of H_{form} are equal to the average of the lowest heats of formation of the structures in their respective datasets.

The level of confidence of predictions for a given structure s is measured by its c-value (confidence value), [172] which here represents the fraction of models in the ensemble that predict structure s to be useful for its intended application, based on the aforementioned criterion. It is calculated as:

$$c(s) = \frac{1}{N} \sum_{i=1}^{N} \mathcal{M}_i(s), \tag{B.1}$$

where $N = 100$ is the number of models used and

$$\mathcal{M}_i(s) = \begin{cases} 1 \text{ if the } i\text{th model predicts the given structure } s \text{ to be useful} \\ 0 \text{ otherwise} \end{cases} \tag{B.2}$$

This allows the 2D structures with the highest likelihood of being useful for their applications to be identified, as shown in Table B.1. Since the training sets for the band gap prediction models contained only

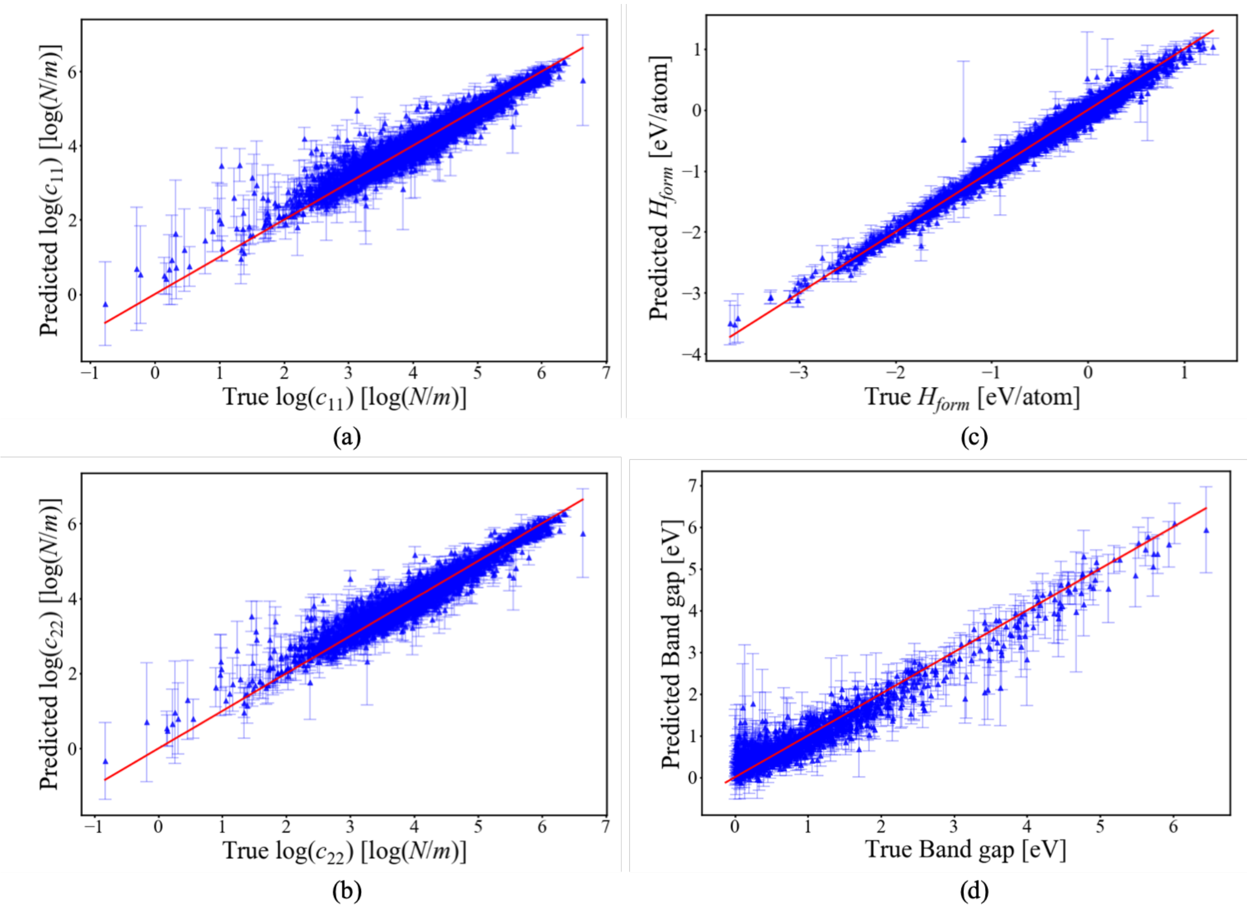

Figure B.3: Comparison of predicted and DFT-calculated (a) log(c_{11}), (b) log(c_{11}), (c) H_{form}, and (d) band gap on C2DB data. The predictions are made using an ensemble of 100 CGCNN models, each trained on randomly selected training data.

materials with non-zero band gap, a further metallic versus insulator filtering, with subsequent update of the c-values, is needed. The reason for this is that, if given a conducting material, these models would predict it to have a positive band gap, since they have only been trained on insulators or semiconductors.

Using the same techniques employed in the generation of the C2DB dataset [162], DFT calculations of the stiffness coefficients were performed for all MXenes with a c-value of 1. All of these structures have both c_{11} and c_{22} greater than 175 N/m. Furthermore, comparing the logarithm of these coefficients with those predicted by the model yields a MAE of 0.117 $\log(N/m)$ for c_{11} and of 0.085 $\log(N/m)$ for c_{22}, with RMSE of 0.128 and 0.093 $\log(N/m)$, respectively.

B.2.2 Identification of Design Principles

To uncover the compositional and structural commonalities of useful candidates, a rigorous methodology was developed to study the design principles that can increase the c-values of different MXene and perovskite

	Structure	c-value	$\langle H_{form} \rangle$ [eV/atom]	$\langle c_{11} \rangle$ [N/m]	$\langle c_{22} \rangle$ [N/m]	$\langle$band gap$\rangle$ [eV]
MXenes	Hf*O-N-Hf*O	1.0	-2.62	273.88	261.60	-
	Sc*O-N-Hf*O	1.0	-2.64	210.15	224.16	-
	Sc*F-N-Hf*O	1.0	-2.63	240.97	220.28	-
	Hf*O-C-Zr*F	1.0	-2.23	266.41	249.99	-
	Hf*O-N-Zr*Cl	1.0	-2.16	211.11	227.78	-
Inorganic Perovskites	$NbZrO_3$; A=Zr, B=Nb	0.98	-2.48	-	-	2.28
	$HfVO_3$; A=Hf, B=V	0.98	-2.33	-	-	2.33
	$MoZrO_3$; A=Zr, B=Mo	0.94	-2.25	-	-	2.38
	$HfNbO_3$; A=Nb, B=Hf	0.94	-2.20	-	-	1.99
	$NbTiO_3$; A=Nb, B=Ti	0.92	-2.18	-	-	2.08
Organic Perovskites	$C_3H_5F_7N_2Sn_2$; A=$C_3H_5N_2$	0.99	-1.21	-	-	2.38
	$C_3H_8F_7NPb_2$; A=C_3H_8N	0.94	-1.13	-	-	2.67
	$C_3H_5F_7N_2Pb_2$; A=$C_3H_5N_2$	0.93	-1.19	-	-	2.63
	$C_2H_7F_7N_2Sn_2$; A=$CH_3C(NH_2)_2$	0.92	-1.37	-	-	2.67
	$CH_5F_7N_2Sn_2$; A=$HC(NH_2)_2$	0.91	-1.60	-	-	2.36

Table B.1: Materials with highest five c-values. For MXenes, '*' indicates a bond between a metallic atom and a termination. For the perovskites, the site occupations have been specified for clarity. Values reported are the mean of the ensemble predictions.

materials. First, for each dataset used, the following functions of the design principle (DP) were established: the subset of all structures satisfying the DP, $\mathcal{D}_{DP} = \{\text{structures that satisfy the DP}\}$; the proportion of the dataset that contains the DP, $P_{DP} = N_{DP}/N_{dataset}$, where $N_{DP} = |\mathcal{D}_{DP}|$ is the cardinality of set $\mathcal{D}_{DP}$ (the number of elements in this set), and $N_{dataset}$ is the total number of structures in the dataset; and the average of c-values of all structures in $\mathcal{D}_{DP}$

$$c_{DP} = \frac{1}{N_{DP}} \sum_{s \in \mathcal{D}_{DP}} c(s), \tag{B.3}$$

which can be interpreted as the chance of an arbitrary trained model predicting that a random structure in $\mathcal{D}_{DP}$ is a useful candidate.

A minimum threshold, c_{cut}, was created to distinguish the best candidate structures from the others. The subset composed of these materials can be expressed as a function of c_{cut} as $\mathcal{B}(c_{cut}) = \{\text{structures with } c\text{-value} \geq c_{cut}\}$. From this definition, it becomes easier to examine how the presence of a specific design rule in a material influences its chance of existing among the best candidates in set $\mathcal{B}(c_{cut})$. For this purpose, more quantities, all functions of c_{cut}, were defined. One of the simplest indicators that a given DP is effective at making a structure useful for the application in a combinatorially generated dataset is the proportion of the set of best candidates $\mathcal{B}$ that is comprised of materials satisfying the DP, $P_{DP|best} = |\mathcal{B} \cap \mathcal{D}_{DP}|/|\mathcal{B}|$, and how it compares with P_{DP}. Additionally, it is helpful to examine the difference between the likelihood of a random material being amongst the best candidates $P_{best|All} = |\mathcal{B}|/N_{dataset}$ and the chance of that happening given that the structure contains the DP, $c_{chanceDP} = P_{best|DP} = |\mathcal{B} \cap \mathcal{D}_{DP}|/|\mathcal{D}_{DP}|$. Besides these quantities, it is also important to measure our confidence in these candidates, members of $\mathcal{B} \cap \mathcal{D}_{DP}$, by averaging their c-values:

$$c_{bestDP} = \frac{1}{|\mathcal{B} \cap \mathcal{D}_{DP}|} \sum_{s \in \mathcal{B} \cap \mathcal{D}_{DP}} c(s). \tag{B.4}$$

Note that, by construction, c_{bestDP} is a monotonically increasing function of c_{cut} while the set $\mathcal{B} \cap \mathcal{D}_{DP}$ is not empty. Finally, although redundant with all previously described measures, we also studied, for completeness, how the elements from $\mathcal{B} \cap \mathcal{D}_{DP}$ contribute to c_{DP}:

$$c_{contribDP} = \frac{\sum\limits_{s \in \mathcal{B} \cap \mathcal{D}_{DP}} c(s)}{\sum\limits_{s' \in \mathcal{D}_{DP}} c(s')} = \frac{|\mathcal{B} \cap \mathcal{D}_{DP}| c_{bestDP}}{|\mathcal{D}_{DP}| c_{DP}} = P_{best|DP} \frac{c_{bestDP}}{c_{DP}}. \tag{B.5}$$

Since the higher the value of the cutoff, the fewer elements are in the set $\mathcal{B} \cap \mathcal{D}_{DP}$, both $c_{contribDP}$ and $c_{chanceDP}$ are monotonically decreasing with c_{cut}. A full dependency of all these variables with the value of the cutoff c_{cut}, for chosen design principles, can be seen in Figures B.4, B.5, and B.6. For all three of the design rules chosen, $P_{DP|best}$ is almost a monotonically increasing function of c_{cut}, indicating that, the more confident one wants to be on the $\mathcal{B}$ set, the more predominant these design principles become in this set. Additionally, prior to the value of c_{cut} for which none of the materials in $\mathcal{B}$ contains the design principles, the chance of finding a member of $\mathcal{B}$ among the set $\mathcal{D}_{DP}$ is of roughly 15% for all three design principles. (Note: values for $c_{cut} = 0$ omitted in the interest of ease of graphical visualization.)

This approach of understanding the effect of design principles is best suited for combinatorially generated datasets. Therefore, it was used to study all of the data mentioned in the Databases Section. A list of all possible design principles using the same combinatorics applied in the creation of the respective datasets was constructed. These design principles were then ordered by highest to lowest $P_{DP|best}/P_{DP}$ ratio at a cutoff value of $c_{cut} = 0.95$ for MXenes, and $c_{cut} = 0.80$ for both inorganic and organic perovskites. The choice for cutoff values was guided by the results from Table B.1: the set of best candidates $\mathcal{B}$ has to be sizeable enough for a meaningful analysis of the design principles. Furthermore, for the MXenes, design rules whose $P_{DP} \leq 0.008\%$ were excluded due to their high specificity. The following interesting equality establishes a relationship between the two most intuitive criteria of gauging the effectiveness of a given DP discussed previously:

$$\frac{P_{DP|best}}{P_{DP}} = \frac{|\mathcal{B} \cap \mathcal{D}_{DP}|}{|\mathcal{B}|} \frac{N_{dataset}}{|\mathcal{D}_{DP}|} = \frac{|\mathcal{B} \cap \mathcal{D}_{DP}|}{|\mathcal{D}_{DP}|} \frac{N_{dataset}}{|\mathcal{B}|} = \frac{P_{best|DP}}{P_{best|All}} \tag{B.6}$$

The results of this analysis are shown in Table B.2. One of the top design principles for MXenes (Figure B.4), inorganic (Figure B.5), and organic perovskites (Figure B.6) were chosen to represent the dependency between the metrics discussed above and the cutoff c_{cut}, which determines the minimum confidence level of the structures in the set of best candidates $\mathcal{B}$.

B.2.3 Analysis of Uncovered Design Principles

The methodology from the previous section was able to identify some known design rules: for example, titanium (Ti) based MXenes tend to have high stiffness coefficients, as suggested by Figure 4 and Table 1 in Anasori *et al.* [173]. Interestingly, however, it also discovered that the other main elements of group 4 of the periodic table, namely, zirconium (Zr) and hafnium (Hf), can increase the mechanical strength of this class of materials, as long as these elements are bonded with oxygen, and the opposite side of the monolayer is either oxygen or fluorine terminated.

Similarly, the model was able to recognize that, in order for hybrid organic-inorganic perovskites to have a band gap in the range of $[1.5, 3]$ eV, the B-sites should be occupied by either lead (Pb) or tin (Sn), a relatively well-known design principle in the photovoltaics community. [174, 175, 176, 177] It also suggests that the organic A-sites should be composed of formamidinium ($HC(NH_2)_2$), imidazolium ($C_3H_5N_2$), or azetidinium (C_3H_8N). Curiously, for these hybrid perovskites, the results suggest that the X-sites be populated by fluorine, rather than the usual iodine. A deeper investigation shows that the reason for this is the enhanced stability of the fluorinated structures: while fluorinated structures have an average band gap of ~ 3 eV and $\langle H_{form} \rangle \approx -1.1$ eV/atom, iodined perovskites have an average band gap of 2.6 eV, but a much higher $\langle H_{form} \rangle \approx -0.3$ eV/atom.

Finally, for purely inorganic perovskites, the analysis proposes that the A-sites be occupied by scandium (Sc), hafnium (Hf), or zirconium (Zr). Analyzing the atomistic features used by the CGCNN model for these elements indicates that all of them have a covalent radius of ~ 170 pm, a first ionization potential in the neighborhood of 640 kJ/mol, and a 1.3 electronegativity in Pauling units. At the same time, the B-sites should be populated with vanadium (V), niobium (Nb), or chromium (Cr), all with atomic radii of ~ 130 pm, first ionization potential of roughly 650 kJ/mol, and an electronegativity of approximately 1.6 in the Pauling scale. Surprisingly, in the field of all-inorganic perovskites for photovoltaics applications, none of these compositions has been deeply investigated; focus has been more directed towards caesium-lead systems ($CsPbX_3$, where X can be I, Br, or Cl) [178], indicating the work presented here may contain new potential directions for further research in this area of science. Figure B.7 depicts a graphical summary of the top design principles uncovered in this work.

The collection of design rules uncovered shows the capability of the developed model to both identify established criteria to attaining material performance, as well as to find new, unexplored avenues for application-focused material discovery, since it can be considered a basis for reverse engineering of 2D structures. Machine learning methods such as CGCNN, coupled with a study of structural and compositional design rules, may open up paths for material innovation in a myriad of fields, including photovoltaics, electro-

	Design principle	c_{DP}	P_{DP} [%]	$P_{DP\|best}$ [%]	$P_{best\|All}$ [%]	$P_{best\|DP}$ [%]	$\frac{P_{DP\|best}}{P_{DP}}$
MXenes	Hf*O-O-N	0.729	0.046	12.069	0.243	63.636	261.897
	Ti*O-O-N	0.683	0.046	10.345	0.243	54.545	224.483
	Hf*O-O	0.560	0.092	18.966	0.243	50.000	205.776
	Zr*O-F-C	0.448	0.046	8.621	0.243	45.455	187.069
	Hf*O-F	0.570	0.092	17.241	0.243	45.455	187.069
Inorganic Perovskites	A=Sc-B=Cr	0.264	0.037	10.526	0.100	28.571	284.632
	A=Zr-B=Sc	0.406	0.037	10.526	0.100	28.571	284.632
	A=Sc-B=V	0.320	0.037	5.263	0.100	14.286	142.316
	A=Sc-B=Nb	0.274	0.037	5.263	0.100	14.286	142.316
	A=Hf-B=V	0.294	0.037	5.263	0.100	14.286	142.316
Organic Perovskites	A=HC(NH_2)$_2$-X=F	0.817	0.446	13.333	2.229	66.667	29.911
	A=$C_3H_5N_2$-X=F	0.790	1.560	43.333	2.229	61.905	27.775
	A=C_3H_8N-X=F	0.629	2.675	30.000	2.229	25.000	11.217
	A=$C_3H_5N_2$-B=Sn	0.282	2.452	26.667	2.229	24.242	10.877
	A=$C_3H_5N_2$-B=Pb	0.255	1.783	16.667	2.229	20.833	9.347

Table B.2: Design principles with five highest values of ratio $P_{DP|best}/P_{DP}$. The cutoff c-values used in computing values displayed for MXenes was c_{cut} = 0.95, and for both inorganic and organic perovskite cases, c_{cut} = 0.80.

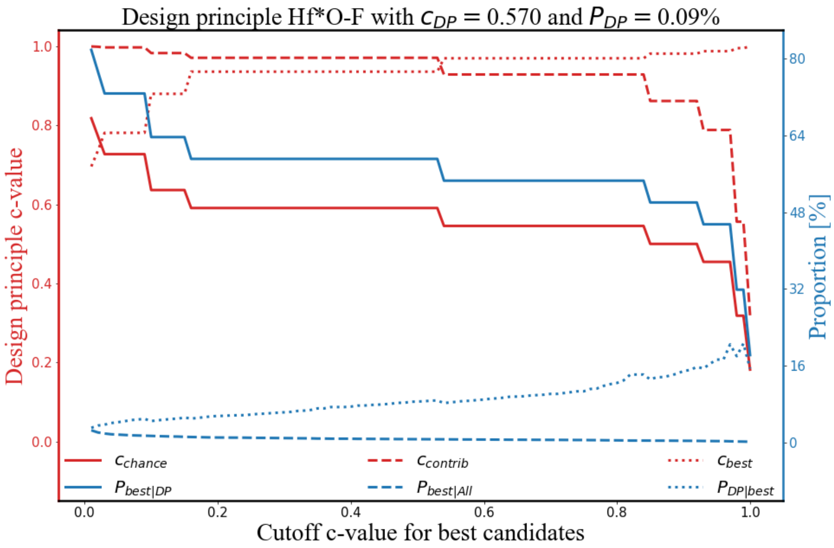

Figure B.4: One of the top design principles for MXenes: hafnium (Hf) bonded with oxygen (O) termination, and with a fluorine (F) termination bonded to any other metal. The likelihood that any arbitrary model predicts that a random material satisfying this DP is a useful candidate is of $\sim 57\%$, as indicated by c_{DP}. Choosing $c_{cut} = 1.0$ shows that the chance of a structure satisfying the DP being among the best candidates is of nearly $c_{chanceDP} = P_{best|DP} \sim 20\%$, and these candiates contribute to approximately 30% of c_{DP}, as shown by $c_{contribDP}$. Note that, for this specific DP, $P_{DP|best}$ almost steadily increase with the value of c_{cut}, indicating that, the more confident we want to be in our set of useful candidates, in general, the more prevalent this DP becomes in this $\mathcal{B}$ set.

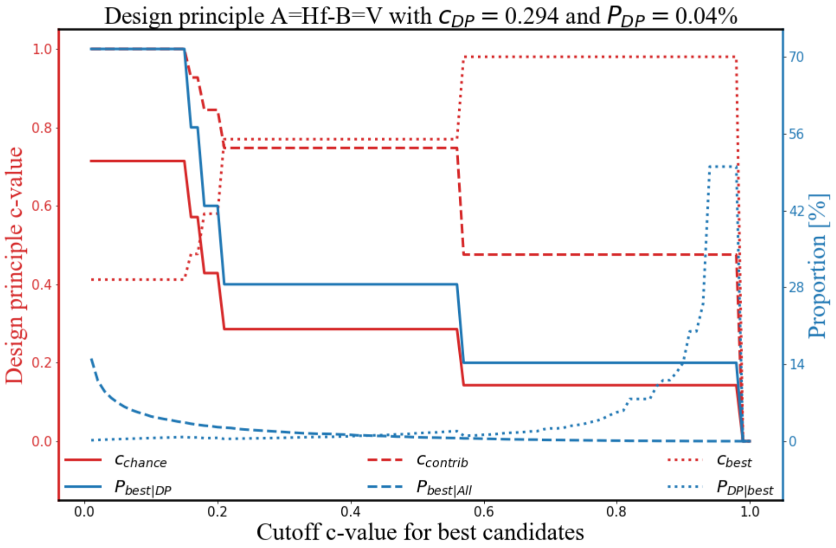

Figure B.5: One of the top design principles for inorganic perovskites: A-site occupied by hafnium (Hf), with vanadium (V) in the B-site. The likelihood that any arbitrary model predicts a random material satisfying this DP is a useful candidate is of $\sim$ 29%, as indicated by c_{DP}. Choosing $c_{cut} = 0.80$ shows that the chance of a structure from set $\mathcal{D}_{DP}$ to be among the best candidates is of $c_{chanceDP} = P_{best|DP} = 14\%$, and these candidates contribute to approximately 50% of c_{DP}, as shown by $c_{contribDP}$. Additionally, for this specific DP, $P_{DP|best}$ almost steadily increases with the value of c_{cut}, indicating that, the more confident we want to be in our set of useful candidates, in general, the more prevalent this DP becomes in this $\mathcal{B}$ set. Finally, an examination of the behavior of c_{best} reveals that, for values of the cutoff $c_{cut} > 0.6$, all of the structures in set $\mathcal{B} \cap \mathcal{D}_{DP}$ have a c-value of nearly 1.0.

chemistry, batteries, mechanically robust materials, among others. In the interest of further accelerating the discovery and screening of more 2D monolayer materials, the code base for this study has been open-sourced on GitHub.

B.3 Summary and Conclusions

Crystal graph convolution neural networks have been extended to describe materials with planar symmetry. This model was used to survey large combinatorially generated datasets of MXene and perovskite materials in search of those with high likelihood of having properties of interest, as determined by the ensemble of trained CGCNN models. From the results of the screening process, underlying molecular design principles were discovered.

Some of the design rules found have already been recognized in the literature and are well-accepted, further demonstrating the robustness of the developed methodology. One such example is identifying hybrid organic-inorganic perovskites with lead or tin as good candidates for solar cell applications [174, 175, 176, 177], while titanium based MXenes as mechanically robust materials [173]. On the other hand, other design

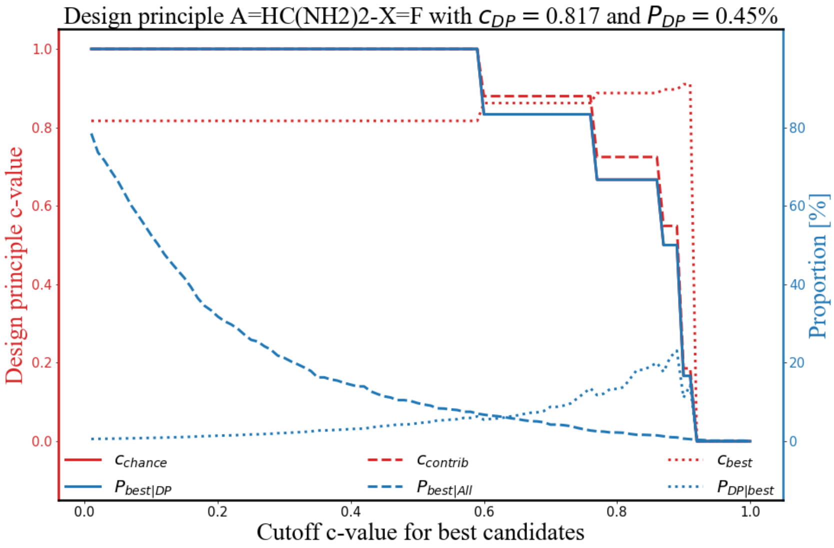

Figure B.6: Top design principle for Khazana perovskites: A-site occupied by formamidinium ($HC(NH_2)_2$), with fluorine (F) in all X-sites. The likelihood that any arbitrary model predicts a random material satisfying this DP is a useful candidate is of $\sim$ 82%, as indicated by c_{DP}. Choosing $c_{cut} = 0.80$ shows that the chance of a structure from set $\mathcal{D}_{DP}$ to be among the best candidates is of $c_{chanceDP} = P_{best|DP} =\sim$ 65%, and these candidates contribute to approximately $\sim$ 70% of c_{DP}, as shown by $c_{contribDP}$.

principles identified could open up new avenues for material exploration. One such design rule is that MXene monolayers with elements from group 4 of the periodic table are likely to have high stiffness coefficients.

Finally, the design rules uncovered can be used as guidance for both experimental and computational testing at different confidence levels. By combining design principles together, as well as by combinatorially populating their unspecified structural sites, datasets of potential high-performance materials can be created. This reverse engineering approach of using design rules as a generative basis can lead to the discovery of even better materials, along with more effective design principles.

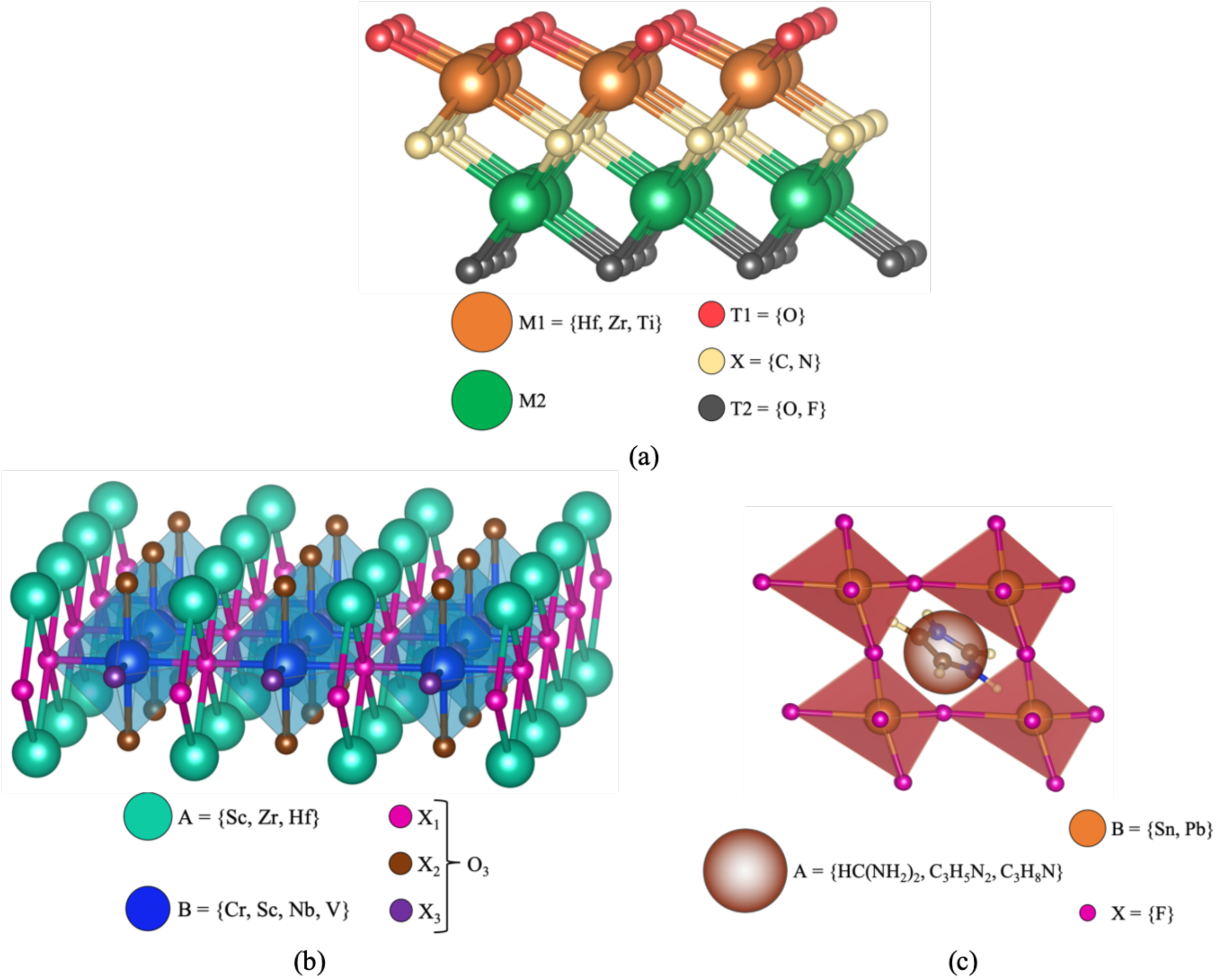

Figure B.7: Summary of uncovered design rules for: (a) MXenes, where hafnium (Hf), zirconium (Zr), or titanium (Ti) must be bonded to an oxygen termination, regardless of the central X component or the metal M2 on the opposite side of the structure, which should have either an oxygen or a fluorine termination; (b) inorganic perovskites, in which the A-site must be occupied by scandium (Sc), zirconium (Zr), or hafnium (Hf), the B-site has to contain chromium (Cr), scandium (Sc), niobium (Nb), or vanadium (V), and, as discussed in the main text, all X-sites should be occupied by oxygen; (c) organic-inorganic hybrid perovskites, where all X-sites must be occupied by fluorine, the B-site can be occupied by either tin (Sn) or lead (Pb), and the A-site possibilities are formamidinium ($HC(NH_2)_2$), imidazolium ($C_3H_5N_2$), and azetidinium (C_3H_8N). Note: in the inorganic perovskite case, even though all X-site occupations should be the same, we represented them by different colors for completeness, since changing the value of c_{cut} used in the analysis allows for other possibilities where all three distinct types of X-sites can be populated by a different atom.

Appendix C

CGCNN Ensemble Performance

In order to measure the performance of the CGCNN model ensenble, it is useful to apply some of the metrics introduced by Kuleshov et al. [179] and Tran et al. [180], namely, calibration and sharpness, besides mean absolute error (MAE) and root mean square error (RMSE).

In their work, the authors create the concept of a calibration plot, which compares, for each predicted data point, the standard deviation of the ensemble predictions (y-axis), and the residual between the mean of the predictions and the true value of the data point – the mean error of the predictions (x-axis). In the regions where the observed estimation interval is greater than the expected interval (green), the model ensemble is called underconfident, since the true value falls within the error bars of the ensemble prediction. On the other hand, when the observed estimation interval is smaller than the expected interval (red), the model is called overconfident, since the standard deviation of the ensemble predictions does not encompass the true data value. The calibration plot for the 100 model ensemble trained to predict conduction band maximum is shown in Figure C.1.

However, measuring calibration is not sufficient for effective uncertainty quantification. For instance, a properly calibrated model with large uncertainty estimates is not as useful as a similarly calibrated model with smaller uncertainties. Thus, the concept of sharpness is introduced: the sharper the model, the smaller its prediction standard deviations. Alternatively, sharpness can be understood as a measure of the precision of the model (while MAEand RMSE take the role of accuracy); the smaller its value, the more precise the model is. This metric is measured in the following manner [180]:

$$sharpness = \sqrt{\frac{1}{N_{dataset}} \sum_{structure} Var[\mathcal{M}(structure)]}$$

Figure C.2 illustrates histograms of the mean prediction errors (blue) and ensemble standard deviations (red) of the CGCNN models trained over band gap data. The values of prediction mean absolute error

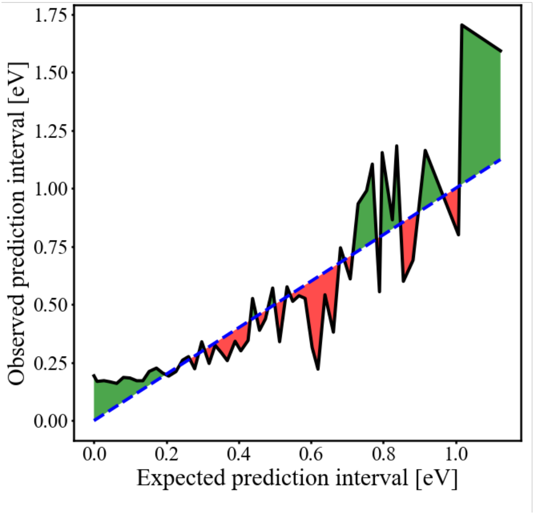

Figure C.1: Calibration plot [179, 180] of CGCNN ensemble CBM prediction. In general, the ensemble of model predictions captures the true values of CBM within one standard deviation.

(MAE) and root mean square error (RMSE), as well as ensemble sharpness, are also represented. Table C.1 contains some of these metrics for all predicted properties. Taking as example band gap and heat of formation predictions, the approach in this work performs better than some first-principle simulations: for band gap, the accepted DFT errors are between 0.25 and 0.4 eV [181, 182], while both CGCNN MAE and sharpness fall on the lower end of this range; for H_{form}, DFT errors are of usually 0.1 eV/atom [159], while all CGCNNs' uncertainty metrics are below this value by a safe margin.

CGCNN is a direction-agnostic framework for machine learning and since the material stiffness only depends on the relative positions of the atoms in the crystal, it can be used to predict the elastic constants as seen from the low MAE and RMSE (Table C.1). In order to avoid overweighing elastic constants of very stiff materials, and since c_{11} and c_{22} are always positive, regression was performed over the logarithm of these quantities.

Property	MAE	RMSE	Sharpness	Unit
$\log(c_{11})$	0.182	0.263	0.188	$\log(N/m)$
c_{12}	8.241	12.497	14.079	N/m
$\log(c_{22})$	0.174	0.250	0.172	$\log(N/m)$
CBM	0.193	0.264	0.310	eV
VBM	0.180	0.251	0.286	eV
Band gap	0.231	0.311	0.278	eV
H_{form}	0.066	0.090	0.072	eV/atom
Speed of sound x	385.703	552.147	366.810	m/s
Speed of sound y	372.015	548.619	351.624	m/s

Table C.1: Metrics for uncertainty quantification of model ensembles

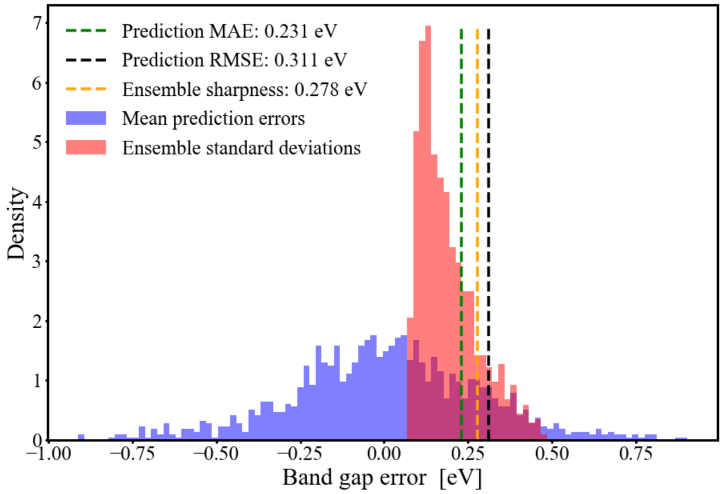

Figure C.2: Histograms of errors on band gap prediction and of standard deviation of ensemble predictions.

Indirectly related to the ensemble performance are its outliers. For each property of interest, structures whose mean prediction error was more than two standard deviations away from the average of all residuals, that is, those who would be at the trailing ends of the blue distribution on Figure C.2, were classified as outliers. These structures were categorized by their prototypes in the C2DB dataset, allowing for a comparison between outlier prototype distribution and the prototype distribution in the entire dataset, as shown in Figure C.3. For all properties, the outlier prototype distribution somewhat follows the data distribution: the prototypes with higher representation in the data also have higher representation among the outliers. While that is true in general, there exist, however, a few prototypes that deviate from this rule, which can be seen by normalizing the number of outliers in each prototype bin by the total number of structures of said prototype in the data, as Figure C.4 shows. In doing so, it was possible to determine the most problematic prototypes for each property. Some trends emerged from this analysis: for nearly all mechanical properties (namely, c_{11}, c_{22}, and speed of sound on x and y directions), the FeSe prototype proved to be the one with highest ratio of outliers ($\sim 16\%$), while, for electronic properties (CBM, VBM, and band gap), "Other" prototypes were always among the five prototypes with highest outlier percentage. The latter is not particularly surprising, since "Other" contains all prototypes with little representation among the data, which makes learning their behavior more difficult for a neural network.

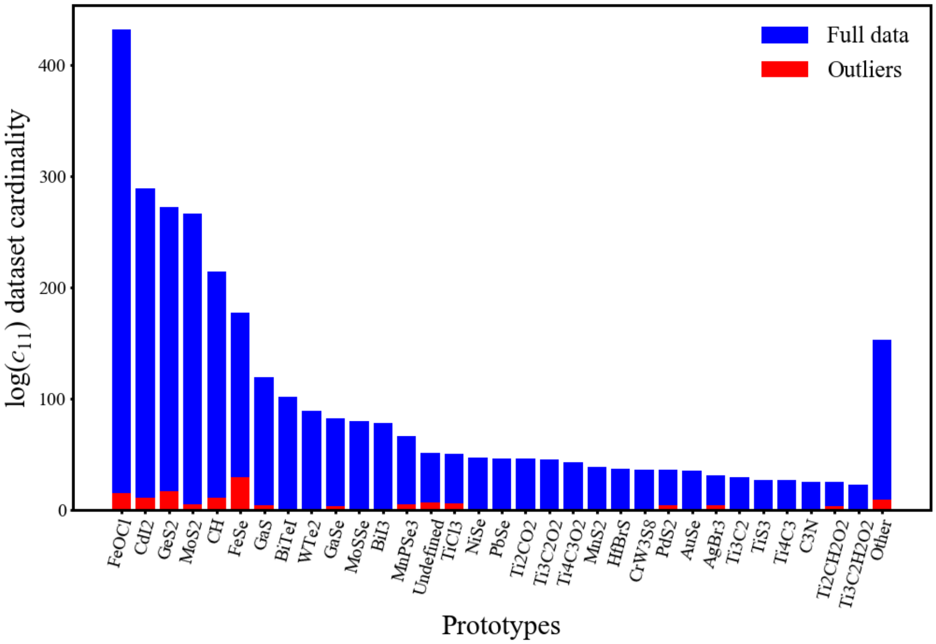

Figure C.3: Distribution of C2DB structures by prototype for log(c_{11}). All prototypes whose total representation accounts for less than 5% of the entire C2DB dataset are binned together under the label "Other".

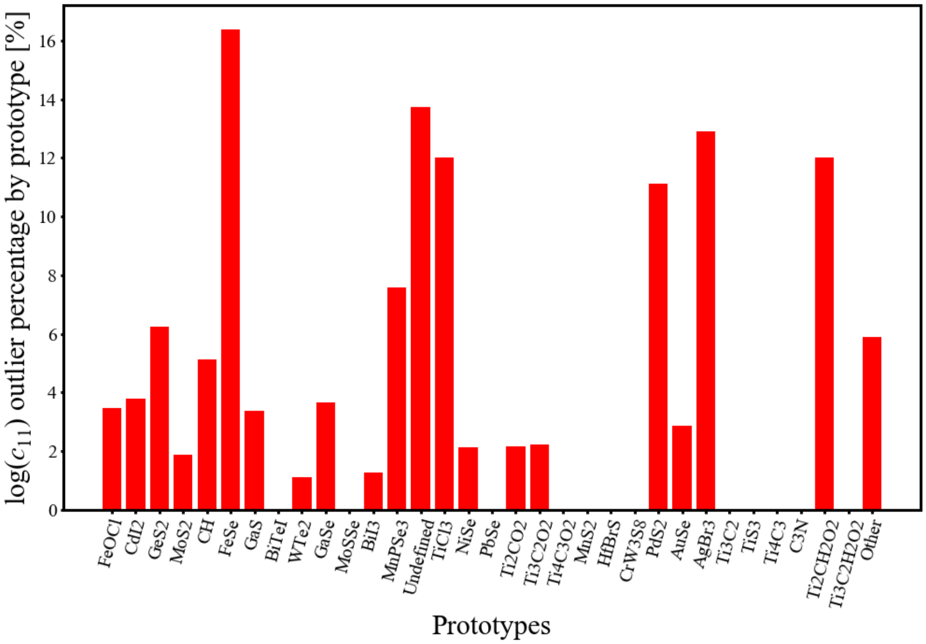

Figure C.4: Percentage of log(c_{11}) outliers by prototype. For most mechanical properties, FeSe is the prototype with highest ratio of outliers.

Appendix D

CGCNN Optimization

A 70:15:15 training:validation:test split ratio for the heat of formation property (H_{form}) on the C2DB database was used to optimize the CGCNN architecture, including number of convolution and hidden layers, learning rate, and number of epochs to be used in training. The models' performances were evaluated as shown in Figure D.1, where, while keeping all other hyperparameters fixed, learning rates of 0.1, 0.01, 0.001, 0.001 were used for training, and, of those, the one that yielded the best model performance was chosen. The number of epochs and of both convolution and hidden layers were optimized in a similar manner. Different possibilities of pooling functions (mean, max, and min) were also tested, as shown in Figure D.2. The final architecture used in the models was composed of 2 convolution layers and 1 hidden layer post-pooling. The networks were trained with a learning rate of 0.01 and a mean pooling function over 300 epochs.

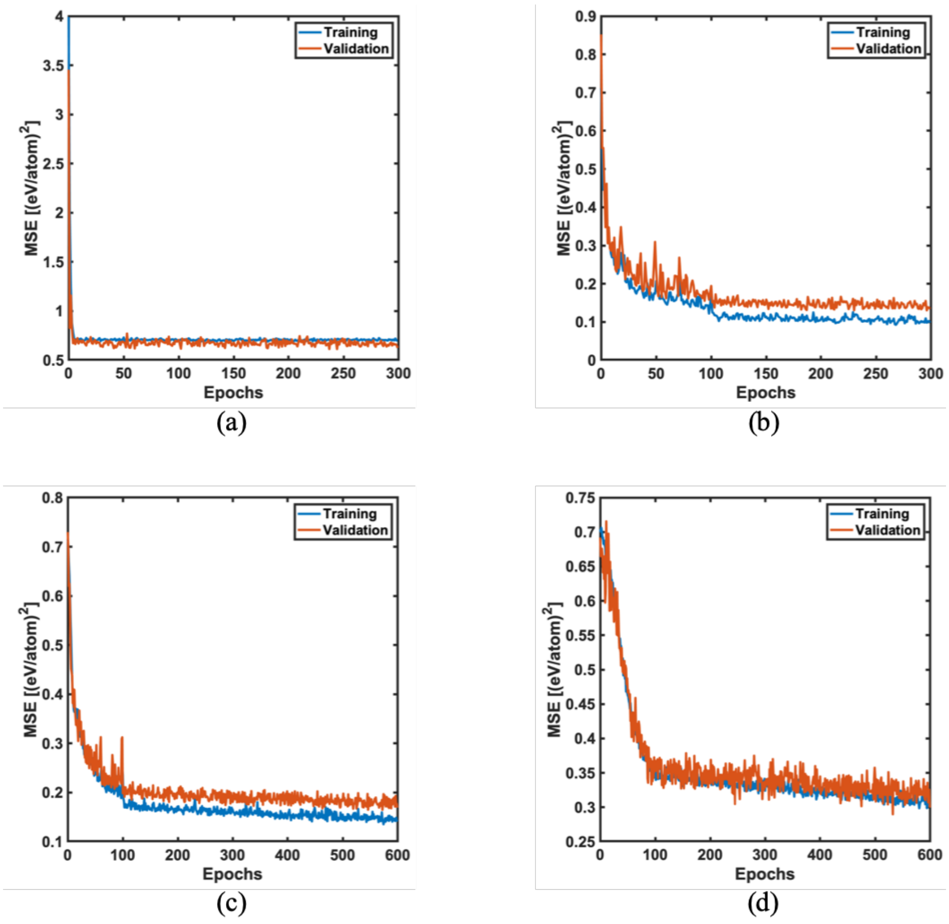

(a) (b)

(c) (d)

Figure D.1: Mean square error (MAE) of H_{form} predictions during training for learning rates of (a) 0.1, (b) 0.01, (c) 0.001, and (d) 0.0001. The lowest errors are obtained with a learning rate of 0.01.

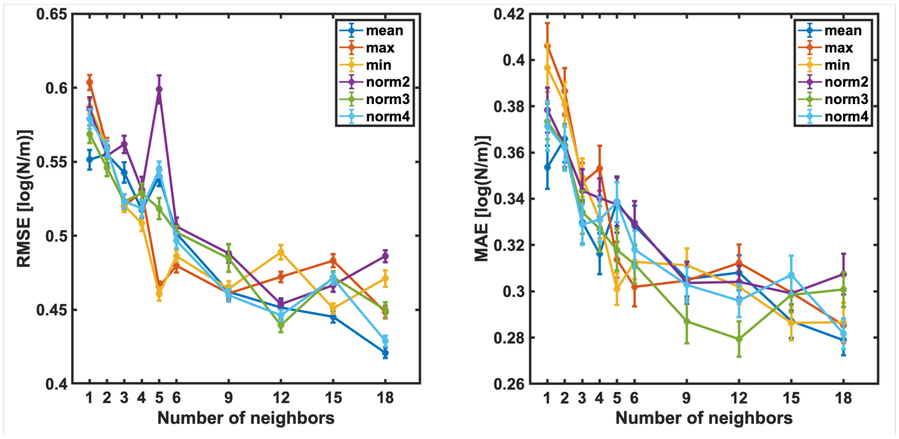

Figure D.2: Evaluation of how pooling functions, as well as number of neighbors used in convolution operations affect RMSE and MAE in $\log(c_{11})$ prediction. We also implemented higher order norm functions as pooling operators. Plots like these were used to evaluate the prediction performance of models using different number of convolution layers, hidden layers, epochs, number of neighbors used in convolution operations, pooling functions, among others.

Appendix E

Graph Convolution Description

The core of CGCNN is in the representation of a crystal structure as an undirected graph $\mathcal{G}$, with a set of nodes V and edges U. Each node $v_i \in V$ corresponds to an atom in the crystal structure, and is represented by the atom's feature vector, including properties such as group number, period number, electronegativity, number of valence electrons, among others. Similarly, each edge $u_{(i,j)_k} \in U$ corresponds to a bond in the crystal structure between atoms i and j, and is represented by a bond feature vector. Here, the subscript k indicates the possibility of there being multiple bonds between atoms i and j. The atomistic feature vectors at convolution step t are denoted by $v_i^{(t)}$, and the bond vectors by $u_{(i,j)}^{(t)}$. From convolution layer t to $t+1$, the atomistic feature vectors are updated in the following manner:

$$v_i^{(t+1)} = v_i^{(t)} + \sum_{j,k} \sigma\left(z_{(i,j)_k}^{(t)} \cdot W_f^{(t)} + b_f^{(t)}\right) \odot g\left(z_{(i,j)_k}^{(t)} \cdot W_s^{(t)} + b_s^{(t)}\right),$$

where $z_{(i,j)_k}^{(t)} = v_i^{(t)} \oplus v_j^{(t)} \oplus u_{(i,j)_k}$ ($\oplus$ indicating concatenation between vectors), σ is a sigmoid function, $\odot$ denotes element wise multiplication, g is a nonlinear activation function, and the $W_f^{(t)}$, $W_s^{(t)}$ and $b_f^{(t)}$, $b_s^{(t)}$ are the weights and biases of the convolutional operation from layer t to layer $t+1$.

Appendix F

Understanding The Basics of Density Functional Theory (DFT)

In this Appendix, an overview of Denstiy Functional Theory (DFT) is provided. One of the most established computational techniques within the realms of Condensed Matter Physics and Materials Science, DFT is capable of predicting material properties based solely on the constituent atomic species and their relative positions.

F.1 Multi-body Problem Setup

The energetics and dynamics of atomic nuclei and their accompanying electrons are well described by the non-relativistic Schrodinger equation.

$$\hat{H}\Psi = i\frac{\partial}{\partial t}\Psi \tag{F.1}$$

where Ψ is the many body wavefunction and $\hat{H}$ is the time dependent Hamiltonian of the system containing M nuclei and N electrons. It is given by:

$$\begin{aligned}\hat{H} = -\sum_{i=1}^{N}\frac{\hbar^2}{2m_e}\nabla_i^2 - \sum_{A=1}^{M}\frac{\hbar^2}{2M_A}\nabla_A^2 - \sum_{i=1}^{N}\sum_{A=1}^{M}\frac{1}{4\pi\epsilon_0}\frac{q_e^2 Z_A}{r_{iA}} + \\ + \sum_{i=1}^{N}\sum_{j>i}^{N}\frac{1}{4\pi\epsilon_0}\frac{q_e^2}{r_{ij}} + \sum_{A=1}^{M}\sum_{B>A}^{M}\frac{1}{4\pi\epsilon_0}\frac{q_e^2 Z_A Z_B}{R_{AB}}.\end{aligned} \tag{F.2}$$

Here, indices i and j run account for all electrons in the system, and indices A and B denote all nuclei. The first two terms of this Hamiltonian describe the kinetic energy of the electrons and the nuclei, respectively. The remaining terms account for the electrostatic interactions, in order, between electrons and nuclei, electrons and other electrons, and nuclei and other nuclei. Since atomic nuclei contain orders of magnitude more mass than electrons, these nuclei move much slower than the electrons. Therefore, the Born-Oppenheimer approximation, which assumes nuclei positions to be stationary, can be used to simplify the previous expression of the Hamiltonian. Under this formalism, the properties of a material or molecule stem from a series of electronic structure solutions to the electron-only time independent Schrödinger equation given by $H_e\Psi = E_e\Psi$. Here, the simplified Hamiltonian can be expressed as:

$$\hat{H}_e = -\sum_{i=1}^{N} \frac{\hbar^2}{2m_e}\nabla_i^2 - \sum_{i=1}^{N}\sum_{A=1}^{M} \frac{1}{4\pi\epsilon_0}\frac{q_e^2 Z_A}{r_{iA}} + \sum_{i=1}^{N}\sum_{j>i}^{N} \frac{1}{4\pi\epsilon_0}\frac{q_e^2}{r_{ij}}. \tag{F.3}$$

The total energy of the system is now given by $E_{tot} = E_e + E_n$, where the nuclear energy E_n is given by the electrostatic nuclear interaction energy. As this Hamiltonian is uniquely defined by the external potential generated by the ions, the ground state of the system must also be uniquely determined by this external potential. In practice, solving for this ground state and the corresponding electronic wavefunctions of a many electron system in an external potential is intractable and an alternative approach is needed.

F.2 Kohn-Sham Equations

In 1964, Hohenberg and Kohn were able to successfully reduce the dimensionality of the problem from 3N dimensions to just 3 dimensions by mapping the problem of finding a many-body wavefunction to that of solving for the electron density of an interacting electron system. [183] They showed that the external potential v_{ext} is determined uniquely (up to a constant) by the ground state density of the electrons $n_0(\boldsymbol{r})$. [183] Thus, since the external potential determines the Hamiltonian and the ground state, all physical observables, most importantly the energy, of the ground state can in principle be determined given the ground state electronic density. They also proved that there exists a universal functional of the energy $E[n]$ that is valid for any external potential, v_{ext}. Therefore, for a given external potential, the ground state of the system is determined by the absolute minimum of this functional minimizing over all wavefunctions with density $n(\boldsymbol{r})$:

$$E_0[n] = \min_{\Psi\to n(\boldsymbol{r})} \langle\Psi|\hat{H}|\Psi\rangle = \min_{n(\boldsymbol{r})} E[n(\boldsymbol{r})] \tag{F.4}$$

This means that all that is needed to understand the ground state electronic structure of any atoms, molecule, crystal, or material is the identity and positions of the ions in that material in order to calculate the external potential felt by the electrons. This functional can be broken into two terms, one that is universal to all systems and one that depends on the external potential, and, thus, on the system under investigation.

$$E\left[n(\boldsymbol{r})\right] = F\left[n(\boldsymbol{r})\right] + \int v_{ext}(\boldsymbol{r})n(\boldsymbol{r})d\boldsymbol{r} \tag{F.5}$$

This universal functional, $F\left[n(\boldsymbol{r})\right]$ is not explicitly known but is defined as the minimum of the kinetic energy and electron-electron interaction energy over all wavefunctions of density $n(\boldsymbol{r})$:

$$F\left[n(\boldsymbol{r})\right] = \min_{\Psi \to n(\boldsymbol{r})} \langle \Psi | \hat{T} + \hat{V}_{ee} | \Psi \rangle \tag{F.6}$$

Seemingly, the problem of minimizing over a 3N-dimensional wavefunction Ψ has been transformed to the much easier minimization over 3-dimensional electron density. However, minimizing the universal functional $F\left[n(\boldsymbol{r})\right]$ requires solving a 3N-dimensional problem. In the majority of DFT implementations, the Kohn-Sham method [184] is used. It is based on the replacement of the original many body problem with a fictitious system of non-interacting electrons in an effective potential. Such effective potential must be constructed in a way to ensure the fictitious non-interacting system has the same ground state density as the real interacting system.

In 1928, using a similar approach, Hartree proposed an approximation to the system of interacting particles based on a set of self-consistent single particle equations. [185] Assuming that each electron experiences Coulombic forces with a nucleus (atomic number Z) and interacts with an average electron density $n(\boldsymbol{r})$, the Hartree term can be written as:

$$v_H = -\frac{1}{4\pi\epsilon_0}\frac{q_e Z}{|\boldsymbol{r}|} + \int \frac{1}{4\pi\epsilon_0}\frac{q_e n(\boldsymbol{r}')}{|\boldsymbol{r}-\boldsymbol{r}'|}d\boldsymbol{r}' \tag{F.7}$$

This implies that the ground state can be obtained by self-consistently solving a set of single particle equations, which can be expressed (using the variational principle) as:

$$\left\{\frac{\hbar^2}{2m}\nabla^2 + v_H(\boldsymbol{r})\right\}\psi_i(\boldsymbol{r}) = \epsilon_i\psi_i(\boldsymbol{r}) \tag{F.8}$$

$$n(\boldsymbol{r}) = \sum_i^N |\psi_i(\boldsymbol{r})|^2 \tag{F.9}$$

Despite not being exact, this approximation can be used within the Kohn-Sham formalism if correction terms are added. Rewriting Eq. F.6 for the non-interacting system in an attempt to re-establish exactness of Hohenberg and Kohn's original work yields:

$$F[n(\boldsymbol{r})] \equiv T_0[n(\boldsymbol{r})] + \frac{1}{2}\int \frac{1}{4\pi\epsilon_0}\frac{q_e^2 n(\boldsymbol{r})n(\boldsymbol{r}')}{|\boldsymbol{r}-\boldsymbol{r}'|}d\boldsymbol{r}d\boldsymbol{r}' + E_{xc} \tag{F.10}$$

where the first two terms are the kinetic energy of the non-interacting system and the Hartree potential. The last term is the exchange-correlation energy, which corresponds to the remaining quantum mechanical energy difference between the exact functional $F[n(\boldsymbol{r})]$ of the interacting system and that of the Hatree-like treatment of the fictitious non-interacting system. The value of this exchange correlation-energy functional is not known exactly. Therefore, the accuracy of any DFT calculation depends largely on the approximation used for this term. The full energy to be minimized is now given by:

$$E = T_0[n(\boldsymbol{r})] + \int v_{ext}(\boldsymbol{r})n(\boldsymbol{r})d\boldsymbol{r} + \frac{1}{2}\int\int \frac{n(\boldsymbol{r})n(\boldsymbol{r'})}{|\boldsymbol{r}-\boldsymbol{r}'|}d\boldsymbol{r}d\boldsymbol{r'} + E_{xc}[n(\boldsymbol{r})] \tag{F.11}$$

Rewriting the exchange-correlation energy as $E_{xc}[n(\boldsymbol{r})] = \int n(\boldsymbol{r})\epsilon_{xc}d\boldsymbol{r}$ leads to the Kohn-Sham Equations, [184] which are solved self consistently:

$$\left\{\frac{1}{2}\nabla^2 + v_{ext}(\boldsymbol{r}) + \int \frac{n(\boldsymbol{r'})}{|\boldsymbol{r}-\boldsymbol{r'}|} + \frac{\delta\epsilon_{xc}}{\delta n}\right\}\psi_i(\boldsymbol{r}) = \epsilon_i\psi_i(\boldsymbol{r}) \tag{F.12}$$

$$n(\boldsymbol{r}) = \sum_i^N |\psi_i(\boldsymbol{r})|^2 \tag{F.13}$$

$$E = \sum_i^N \epsilon_i \tag{F.14}$$

For spin-polarized calculations, The Kohn-Sham equations are solved separately for the spin-up and spin-down wavefunctions:

$$\left\{\frac{1}{2}\nabla^2 + V(\boldsymbol{r}) + \sum_\alpha \int \frac{n_{\alpha\alpha}(\boldsymbol{r'})}{|\boldsymbol{r}-\boldsymbol{r'}|} + \frac{\delta\epsilon_{xc}}{\delta n}\right\}\begin{pmatrix}\phi_i^{(+)}(\boldsymbol{r})\\ \phi_i^{(-)}(\boldsymbol{r})\end{pmatrix} = \epsilon_i\begin{pmatrix}\phi_i^{(+)}(\boldsymbol{r})\\ \phi_i^{(-)}(\boldsymbol{r})\end{pmatrix} \tag{F.15}$$

$$n_{\alpha\beta}(\boldsymbol{r}) = \sum_i^N \phi_i^{*\alpha}(\boldsymbol{r})\phi_i^{\beta}(\boldsymbol{r}) \tag{F.16}$$

where α, and β can be $(+)$ or $(-)$. If the system has collinear spin, its magnetization is given by [186]

$$M_{\text{spin}} = \int (n^{(+)}(\boldsymbol{r}) - n^{(-)}(\boldsymbol{r}))d\boldsymbol{r} \tag{F.17}$$

F.3 Exchange Correlation Functionals

For time-independent solutions to the non-relativistic Schrodinger equation, the Kohn-Sham formalism presented in the previous section is exact within the Born-Oppenheimer approximation. This has only been accomplished by defining the exchange correlation energy to be the universal function that accounts for all physical terms not already already included in the previous terms and that properly corrects the kinetic energy from that of the non-interacting fictitious system to that of the real many electron system. Different approximations to this exchange-correlation term have allowed for reasonably accurate predictions at varying, yet viable, computational costs.

In their original work, Kohn and Sham assumed the exchange-correlation functional to have a quasi-local form. According to this approximation, now known as the local density approximation (LDA), the exchange-correlation at every point is that of a homogeneous electron gas (HEG) of the same density. Letting ϵ_{xc}^{HEG} be the exchange-correlation energy per electron in a HEG of density n,

$$E_{xc}^{LDA}[n(\boldsymbol{r})] = \int n(\boldsymbol{r})\epsilon_{xc}^{HEG}\left[n(\boldsymbol{r})\right] d\boldsymbol{r} \tag{F.18}$$

While $\epsilon_{xc}^{HEG}[n(\boldsymbol{r})]$ is unique, several different parameterizations of LDA have been proposed. [187, 188, 189, 190] In spite of its simplicity, the LDA exchange-correlation functional has been shown to predict ionization energies of atoms, dissociation energies of molecules, and cohesive energy of solids in many cases within 10% error. It can also accurately predict structure geometries within 1% error. [191] It is particularly accurate for elemental metal systems, since the nearly-free electrons in these materials resemble a slowly varying electron gas.

In order to more accurately estimate the exchange-correlation energy, the gradient of the electron density should also be accounted for. This is done through the generalized gradient approximation (GGA) as follows:

$$E_{x}^{GGA}(n, \nabla n) = \int \epsilon_{xc}\left[n, \nabla n\right] d\boldsymbol{r} \tag{F.19}$$

Since the is no unique way to include the gradient dependence, there exist several different versions of GGA exchange-correlation functionals. Some of the most commonly used are PBE [94], RPBE [169], and PW91 [192].

Compared to LDA, GGA-based functionals have better performance when used to predict properties of materials with more localized electrons including transition metal complexes, surfaces, and interfaces. However, these functionals are still quasi-local. Additional improvements of energies and structures can be achieved by adding an explicit non-local van der Waals density function (vdW-DF) kernel for the correlation energy:

$$E_c^{nl} = \int\int n(\boldsymbol{r})\phi(\boldsymbol{r}, \boldsymbol{r'})n(\boldsymbol{r'})d\boldsymbol{r}d\boldsymbol{r'} \tag{F.20}$$

The full correlation energy is now given by

$$E_c[n] = E_c^0[n] + E_c^{nl}[n] \tag{F.21}$$

Several non-local kernels have been developed with success, including DF [193], DF2 [194], vdW-DF-cx [195], and optPBE-vdW [196].

Appendix G

Introduction to The Nudged Elastic Band (NEB) Method

The Nudged Elastic Band (NEB) method is an algorithm used to find a minimum energy pathway (MEP) between two energy minima in a potential energy landscape – in other words, it can be used for identifying saddle points of a complex energy landscape. The NEB method has many applications in *ab initio* studies of atomic systems, as a physical system will follow the MEP when it transitions between two energy minima. Here, we briefly review the theory behind the NEB method, as well as show simple example implementations for two distinct analytical functions.

G.1 Minimum Energy Pathway (MEP) and Saddle Point

The rate of a chemical reaction is directly related to its activation energy. This barrier is calculated by comparing the energy of the initial and final stages of the reaction – which are local minima of a multi-dimensional potential energy landscape – with the energies of the intermediate transition states. As the system evolves from reactants to products, it follows the Minimum Energy Pathway (MEP), which passes through the saddle points of the aforementioned potential energy landscape. Therefore, any problem where the dynamics of a transition is relevant requires the computation of the MEP and saddle points. For example, if one is interested in calculating the ionic conductivity of a specific species in a given material, it is essential to compute a diffusion barrier, as well as to understand the possible pathways through which diffusion can occur.

G.2 Plain Elastic Band (PEB) Method

A precursor to the NEB method is the Plain Elastic Band (PEB) algorithm. The PEB method discretizes the path between the given initial and final stages of a transition into a number of nodes/images determined by the user. Throughout this Appendix, the terms “node" and “image" will be used interchangeably to denote the current configuration of the system as it transitions from reactants (initial stage) to products (final stage). At each iteration of the algorithm, each image is evolved in a way to approach the MEP based on two factors: its current position on the potential landscape, and the relative position of its neighbor images. Updating the position of a given image (i-th node, for simplicity) requires the calculation of the fictitious force it experiences:

$$\vec{F}_i = -\vec{\nabla} V(\vec{R}_i) + \vec{F}_i^s. \tag{G.1}$$

Here $-\vec{\nabla} V(\vec{R}_i)$ describes the force the i-th image (with system positions $\vec{R}_i$) experiences due to the potential landscape, which contributes to the minimization of the energy of the image in question. The $\vec{F}_i^s$ term indicates a spring force due to the adjacent nodes. Springs are added to prevent the images from “equilibrating" back to the local minima given by the initial and final stages. In the PEB method, the spring forces are given by:

$$\vec{F}_i^s = k_{i+1}\left(\vec{R}_{i+1} - \vec{R}_i\right) - k_i\left(\vec{R}_i - \vec{R}_{i-1}\right). \tag{G.2}$$

Though intuitive, the PEB method has shortcomings that prevent it from always fully capturing the MEP. These issues can be seen in Figures G.1(a) and G.1(b): when the true MEP is curved at the saddle point, the path between the PEB nodes tends to “cut the corner" and fails to find the most important point in the MEP, that which determines the energy barrier of a transition – the saddle point. Figure G.1(a) represents one of the two reasons for this to happen: at the saddle point (and its vicinities), the potential forces are zero (or negligible), but, since the MEP is curved, one of the components of the spring forces points in the vertical direction, while the other points in the horizontal direction, thus pushing a node that is at the saddle point away from it. One may naively think that reducing the spring constants (as to diminish their effect on nodes close to the saddle point) would remedy this issue. That is not the case, however, as shown in Figure G.1(b), where the springs are less stiff than those in Figure G.1(a). In this example, as the PEB images approach the saddle point, they get pushed away from it by the potential landscape, which is now stronger than the springs that were added specifically to prevent the images from “sliding" down in the MEP towards the minima. Since it is impossible to know the optimal spring constants to be used *a priori*, the PEB corner cutting issue severely hinders this method’s utility.[197]

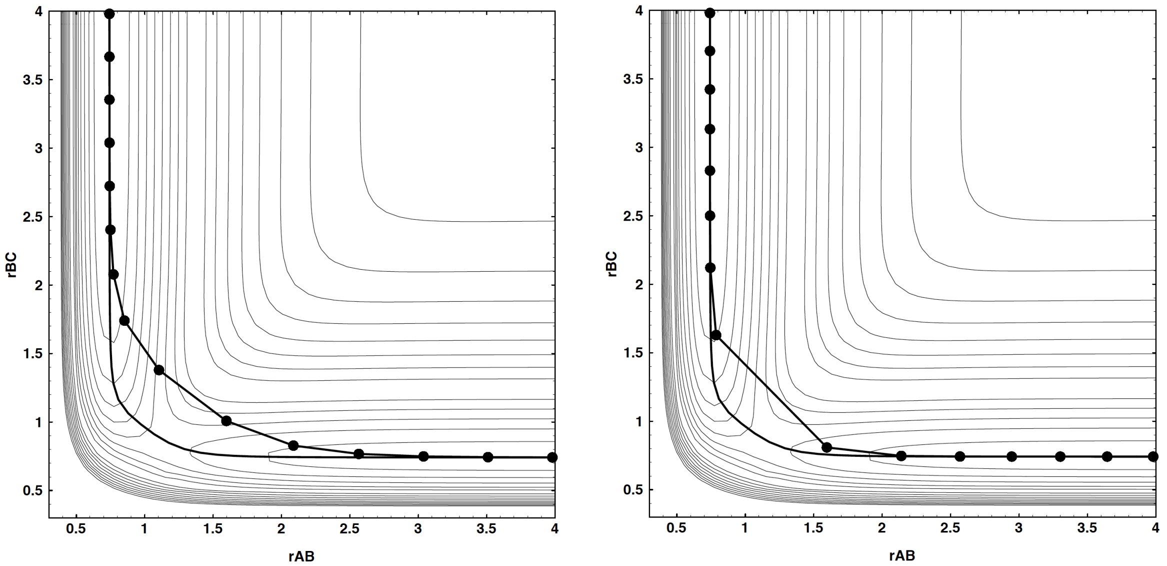

(a) Stiff spring constants push PEB images away from the saddle point due to the lack of a potential force.

(b) Soft spring constants allow the potential forces to slide PEB images along the MEP, away from the saddle point.

Figure G.1: Examples of corner cutting caused by PEB method when the spring constants are (a) too stiff, or (b) too soft. Since these are just toy examples, there is no meaning, nor units, associated with the axes [197].

G.3 NEB Origins: "nudging" of forces

G.3.1 Naive NEB

The previous section identifies two main reasons responsible for the failures of the PEB method: namely, the stiff spring forces that push images away from the saddle point, acting orthogonally to the curved MEP; and the potential forces that cause images to slide down away from the saddle point because they are parallel to the MEP. A possible solution that addresses both of these problems is "nudging" the forces on the images by considering only the component of the potential force that is normal to the MEP, and the component of the spring force that is parallel to the MEP. The Nudged Elastic Band (NEB) method is born. The new expression for the net force acting on the i-th node at a given iteration becomes

$$\vec{F}_i = -\vec{\nabla} V(\vec{R}_i)|_{\perp} + \vec{F}_i^s|_{\parallel}, \tag{G.3}$$

where

$$\vec{\nabla} V(\vec{R}_i)|_{\perp} = \vec{\nabla} V(\vec{R}_i) - \left[\vec{\nabla} V(\vec{R}_i) \cdot \hat{\tau}_{\parallel}^{(i)}\right] \hat{\tau}_{\parallel}^{(i)}, \tag{G.4}$$

$$\vec{F}_i^s|_{\parallel} = \left[\vec{F}_i^s \cdot \hat{\tau}_{\parallel}^{(i)}\right] \hat{\tau}_{\parallel}^{(i)}, \tag{G.5}$$

and $\hat{\tau}_{\|}$ is a unit vector tangent to the path of images. Naively, one would define this vector as

$$\begin{aligned} \vec{\tau}_{\|}^{(i)} &= \frac{\vec{R}_i - \vec{R}_{i-1}}{|\vec{R}_i - \vec{R}_{i-1}|} + \frac{\vec{R}_{i+1} - \vec{R}_i}{|\vec{R}_{i+1} - \vec{R}_i|}, \\ \hat{\tau}_{\|}^{(i)} &= \frac{\vec{\tau}_{\|}^{(i)}}{|\vec{\tau}_{\|}^{(i)}|} = \hat{\tau}_i. \end{aligned} \tag{G.6}$$

From this, we can rewrite the spring force component acting on the i-th image as

$$\vec{F}_i^s|_{\|} = k\left[\left(\vec{R}_{i+1} - \vec{R}_i\right) - \left(\vec{R}_i - \vec{R}_{i-1}\right)\right] \cdot \hat{\tau}_i \hat{\tau}_i. \tag{G.7}$$

This method, however, also has its drawbacks: the formation of kinks, which can be seen in Figure G.2(a). Let us study what is happening in this specific case by looking at the highlighted kink. In yellow, we draw the tangent to the path (since both neighboring images are equidistant from the node in question, the tangent to the path is in the direction that connects the two of them). In purple, we draw the potential force, which pushes the node closer to the nearby minimum. Note that this force is nearly parallel to the tangent to the path, so its component that is orthogonal to $\hat{\tau}_i$ is negligible. In green, we can see the spring forces. A simple visual inspection shows that the net spring force is practically orthogonal to $\hat{\tau}_i$, so its parallel component to this vector is insignificant. Therefore, when kinks are formed, this version of the NEB method is not able to “straighten" them out back into the MEP.

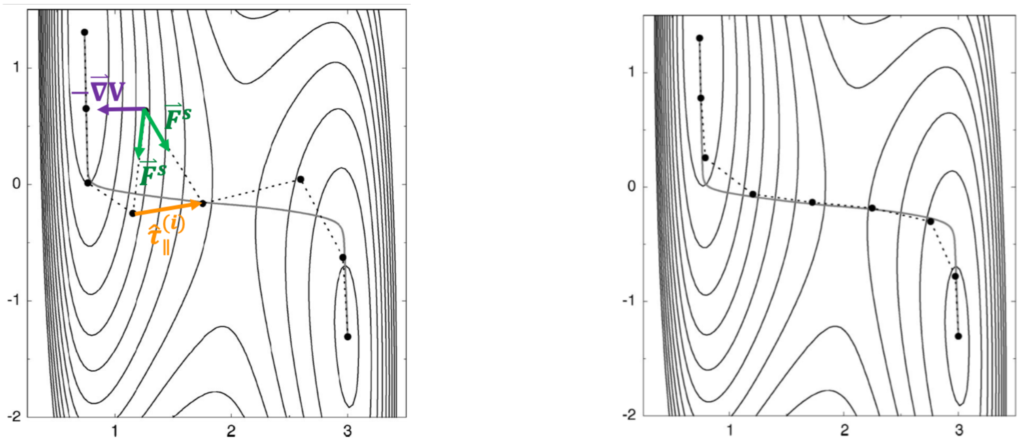

(a) Formation of kinks on the naive implementation of the NEB method.

(b) Kinks are smoothed out in the improved implementation of the NEB method.

Figure G.2: Examples of the (a) naive and (b) improved implementations of the NEB method. The new definition of $\hat{\tau}_i$ allows the NEB method to properly capture the MEP without kinks [197].

G.3.2 Improved Nudged Elastic Band

A solution to address the formation of kinks discussed in the previous section is to redefine the tangent to the path vector. [197] Since the mathematical reasoning for this is very involved, and beyond the scope of this thesis, we will explain only the intuition behind it. In general, the most important point of the MEP is the saddle point, which is the point of maximum energy within the MEP. Therefore, it is more logical to define the tangent of the path as the vector that points to the image of higher energy, as a way of trying to bias the evolution of the path towards the saddle point. This new formulation $\hat{\tau}_i$ can be expressed as

$$\vec{\tau}_i = \begin{cases} \vec{\tau}_i^{+} = \vec{R}_{i+1} - \vec{R}_i & \text{if } V_{i+1} > V_i > V_{i-1} \\ \vec{\tau}_i^{-} = \vec{R}_i - \vec{R}_{i-1} & \text{if } V_{i+1} < V_i < V_{i-1} \\ \vec{\tau}_i^{+} \Delta V_i^{\max} + \vec{\tau}_i^{i} \Delta V_i^{\min} & \text{if } V_{i+1} > V_{i-1} \\ \vec{\tau}_i^{+} \Delta V_i^{\min} + \vec{\tau}_i^{i} \Delta V_i^{\max} & \text{if } V_{i+1} < V_{i-1}, \end{cases} \tag{G.8}$$

where

$$\Delta V_i^{\max / \min} = \max / \min \left(|V_{i+1} - V_i|, |V_i - V_{i-1}| \right). \tag{G.9}$$

This new definition requires a modification on the definition of the spring forces:

$$\vec{F}_i|_{\parallel} = k \left(|\vec{R}_{i+1} - \vec{R}_i| - |\vec{R}_i - \vec{R}_{i-1}| \right) \cdot \hat{\tau}_i. \tag{G.10}$$

Note that, in this scenario, the spring forces act only to keep the intermediate nodes separate, and, thus, the choice of spring constant k is arbitrary. Finally, using this redefined $\hat{\tau}_i$ formulation on the same system shown in Figure G.2(a), we get the improved results in Figure G.2(b).

G.3.3 System Evolution - velocity Verlet

So far, we have discussed how the NEB method computes the fictitious forces each image experiences at each iteration of the algorithm. In this section, we will review one of the methods that can be used for evolving the system iteratively (that is, how to update the positions of each image given the forces they feel).

One of the most intuitive ways of evolving the system is by using a modified velocity Verlet algorithm. [198] Before we go into the details of this method, let us imagine that, at each iteration, each image has a certain velocity, which describes how fast it is traversing the high-dimensional energy landscape towards the MEP at the given iteration. These velocities are used to updated the position of the nodes, and then they are updated based on the forces the nodes feel.

To better understand this process, let us imagine we are trying to update the position and velocity of the i-th image given its current position, velocity, and forces. First, we compute the component of the velocity that is parallel to the force. If this component points in the same direction as the force, we assign it to be the current velocity vector (as debated in the previous section, we are mostly interested in moving the nodes along $\hat{\tau}_i$). Otherwise, the velocity is set to zero. The reasoning behind this is as follows: if the velocity and the force point in opposite directions, the node has overshot the MEP, and needs to be brought back towards the MEP. These are the main modifications to the velocity Verlet algorithm. The next step is to update the position of the image using a standard second order Taylor expansion. Finally, the velocity is updated using the trapezoidal integration technique (since we already have the new position of the node, $\vec{R}_i^{\text{new}}$, the new net force $\vec{F}_i^{\text{new}}$ can easily be computed). This process is shown algebraically on the set of Equations G.11 below. In these equations, Δt and m are variables related to the integration step: for instance, the smaller the Δt (for a fixed m), the longer it will take for the algorithm to reach convergence, but the more accurate the final guess for the MEP will be.

$$\begin{aligned}
\vec{v}_i &= \begin{cases} \left(\vec{v}_i \cdot \vec{F}_i\right) \cdot \hat{\tau}_i & \text{if } \vec{v}_i \cdot \vec{F}_i > 0 \\ 0 & \text{otherwise} \end{cases} \\
\vec{R}_i^{\text{new}} &= \vec{R}_i + \Delta t \vec{v}_i + \frac{(\Delta t)^2 \vec{F}_i}{2m} \\
\vec{v}_i^{\text{new}} &= \vec{v}_i + \frac{\vec{F}_i + \vec{F}_i^{\text{new}}}{2m}.
\end{aligned} \tag{G.11}$$

One additional note is that there are other ways to evolve the system of nodes. One such method is the Broyden–Fletcher–Goldfarb–Shanno (BFGS) algorithm, which is very similar to a gradient descent-based method that performs a line optimization. This algorithm is more accurate than the modified velocity Verlet technique from above, but it is more computationally expensive, since it requires the computation of double derivatives.

G.4 Computational Details

We implemented the improved Nudged Elastic Band algorithm from section G.3.2 in both Python and MATLAB. The system is updated using the modified velocity Verlet update rule from section G.3.3. While there exist a few different criteria that could be used to determine whether convergence has been reached, one of the most common is to check if the magnitude of the forces experienced by all intermediate nodes is less than a user-input tolerance Γ:

$$|\vec{F}_i| < \Gamma, \forall i \in \{\text{intermediate images}\}_i$$

where $\vec{F}_i$ is defined in Equation G.3 and Γ is the tolerance. For the analytical functions in section G.5 we used a tolerance of 0.5, $m = 10$, and a velocity Verlet time step of $\Delta t = 0.01$. It's worth noting that the convergence is strongly affected by the Δt value. Finding the MEP for the analytical functions with $\Delta t = 0.07$, for example, required two orders of magnitude fewer iterations for convergence compared to calculations using $\Delta t = 0.01$.

In general, the MEP between two energy minima will be unknown because determining the true MEP requires knowledge of the entire potential energy surface. For atomic systems in, say, a density functional theory calculation, it is too computationally expensive to confirm that the MEP from an NEB calculation is indeed the global MEP. However, for low-dimensional analytical functions, it is possible to visualize the entire potential energy surface and confirm that the MEP has indeed been found. In section G.5, an implementation of the NEB algorithm is used with two examples of low-dimensional functions.

G.5 Example with Analytical Functions

In this section, an implementation of the NEB algorithm was applied to toy systems consisting of single particles traversing a known 2D potential energy landscape (i.e., the potential energy of the particle at a point (x, y) is modeled by a known function $f(x, y)$). Figure G.3(a) shows several intermediate paths found by the NEB implementation as it searches for the MEP. The initial and final states of the particle are $\vec{R}_i = (0.5, 1.5)$ and $\vec{R}_f = (1.5, 0.4)$, respectively. We chose to use five intermediate images between the initial and final states. The potential energy for the particle is given by the function

$$f_1(x, y) = \cos(2\pi x) + 2\cos(2\pi y).$$

We chose the initial path given to the NEB algorithm to be a linear interpolation of the initial and final states, which is shown in Figure G.3(a) in cyan. Figure G.3(a) also shows multiple paths at different velocity Verlet iterations. 30,678 iterations were required to reach force convergence based on a tolerance of 0.3 (arbitrary units). The initial path passes very closely to a local maximum, but as the number of velocity Verlet iterations increases the images fall away from this maximum. The path in black (15,000 iterations) is not converged to the tolerance of 0.3, but subsequent paths vary little from this path. One interesting feature in comparing the magenta (10,000 iterations) to the black (15,000 iterations and essentially converged) paths is that the magenta path has a node at about $(0.8, 0.4)$, while the same node in the black path is above the magenta node. This is due to the velocity of this image causing it to "overshoot" during convergence. Our algorithm correctly captures the MEP with the black (15,000 iteration) path, as it passes over two saddle points, at around $(0.5, 1)$ and $(1, 0.5)$, and avoids the maximum at the center of figure G.3(a).

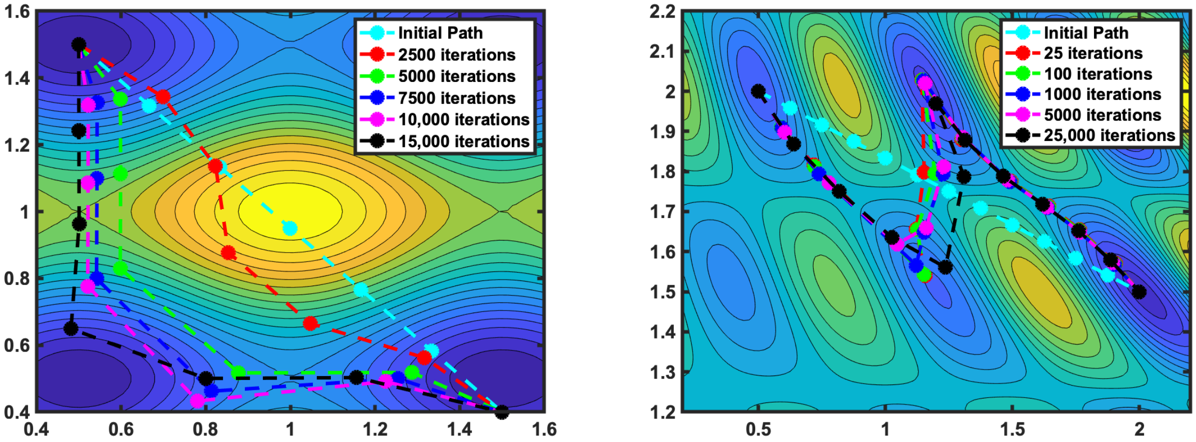

(a) Intermediate paths determined by the NEB algorithm for f_1, with the diffusing particle at initial and final positions $\vec{R}_i = (0.5, 1.5)$ and $\vec{R}_f = (1.5, 0.4)$.

(b) Intermediate paths determined by the NEB algorithm for f_2, with the diffusing particle at initial and final positions $\vec{R}_i = (0.5, 2)$ and $\vec{R}_f = (2, 1.5)$, respectively.

Figure G.3: The NEB method applied to a single particle diffusing on two different potential energy surfaces. The potential energy surfaces are represented with contour plots. Particle energy on the potential energy surface increases with brighter colors (e.g., yellow indicates higher energy than blue).

Figure G.3(b) shows the initial, intermediate, and final paths for the potential energy surface described by the function

$$f_2(x, y) = (x^2 + y^2)\sin[\pi(x + y + xy)].$$

The initial path was chosen to be a series of 11 linearly interpolated images for the particle between the initial state $\vec{R}_i = (0.5, 2)$ and the final state $\vec{R}_f = (2, 1.5)$. 34,631 iterations were required to reach convergence based on a tolerance of 0.3. The intermediate paths for this potential energy surface change significantly with few iterations ($\sim$ 100 iterations), but the use of the velocity Verlet method necessitates a large number of iterations for convergence to the MEP. One interesting feature of the MEP it predicts is that the particle visits local minima instead of travelling along the horizontal line at $y \approx 1.75$ that connects the saddle points, even though these saddle points are all captured in the predicted MEP. The intermediate minima are analogous to intermediates in a chemical reaction. [198, 199] For example, exothermic (i.e., thermodynamically favorable) reactions occur in several downhill steps rather than in one step. These intermediate states are local minima in energy which the system visits briefly before continuing to the reaction minimum (i.e., the reaction products). Minima like the ones on the MEP in Figure G.3(b), then, could be an indication of potentially overlooked or physically important intermediate states that should be investigated further. The best procedure for doing this would be to run several NEB calculations, one for each plausible pair of local minima, as to increase resolution at each of the saddle points.

These examples indicate that the NEB method can qualitatively and quantitatively captured the MEP for these types of simple systems. Applying it to a system of atoms is conceptually very similar: the only difference being the dimension of the space of the energy landscape; instead of a single particle in 2D, the problem now involves several particles in 3D.

Appendix H

Lithium Electrode Sub-Assembly Details

An analysis of the dependence of the LiF surface vacancy hopping barrier on the vacancy concentration was performed in order to optimize the size of the simulation cell with respect to the computational costs required by first-principles calculations. The results of this optimization are shown in Figure H.1, and indicated that an 8% concentration is sufficient for highly-accurate analysis of Li^+ motion in LiF@PIM composite.

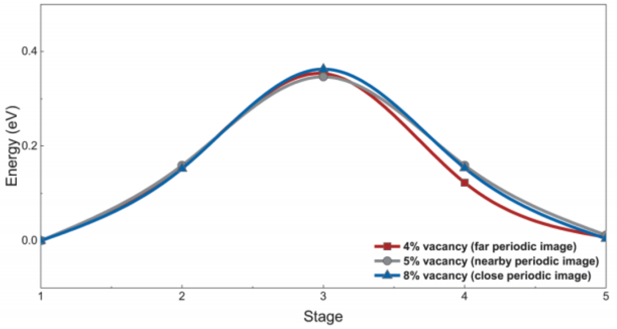

Figure H.1: Periodic image effects on activation energy of hopping on LiF surface. The NEB method is used to calculate the activation barrier along with the required number of supercells to achieve the desired Li vacancy concentrations of 4, 5, and 8%. The analysis shows that the activation energy is converged to within 10 meV at a Li vacancy concentration of 8%.

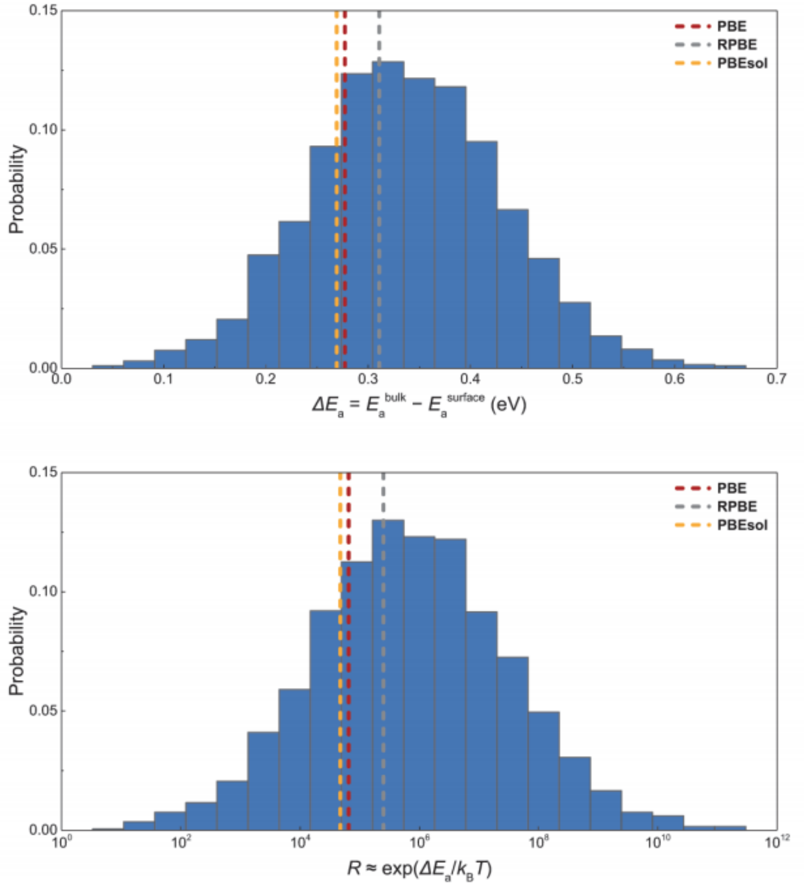

Figure H.2: Probability distribution of the difference in activation energy of Li hopping between bulk and surface of LiF. The difference $\Delta E_a = E_a^{bulk} - E_a^{surf}$ is shown in a histogram corresponding to the calculation performed using an ensemble of exchange-correlation functionals. The ratio of ionic conductivity $R \approx \exp\left(\Delta E_a / k_B T\right)$ in each system at 300 K is also shown as a histogram. The values for specific exchange correlation functionals (PBE, revised PBE, and PBEsol) are marked with dashed lines. The figure shows bulk ionic conduction in LiF is insignificant compared to surface.

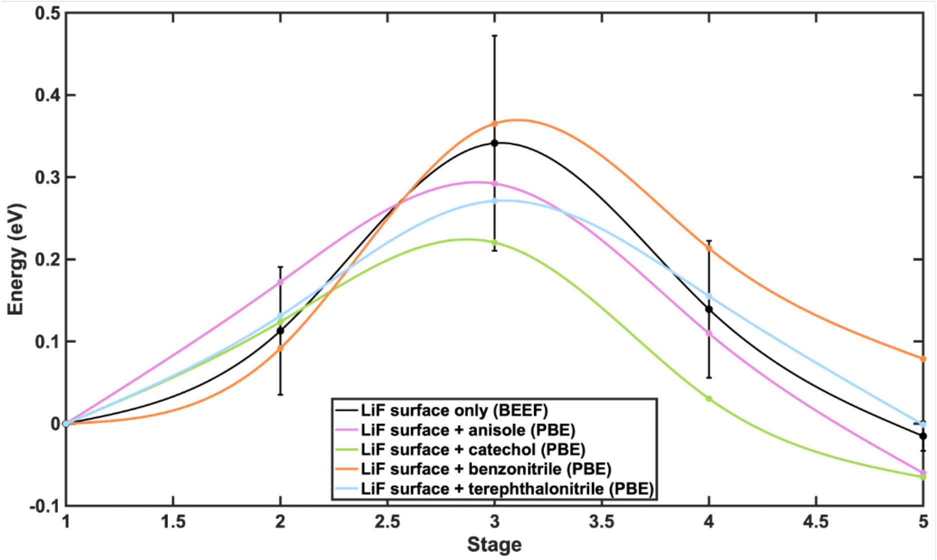

Figure H.3: Effect of PIM-representative molecules on energy landscape of migrating Li^+ along LiF (100) surface facet.

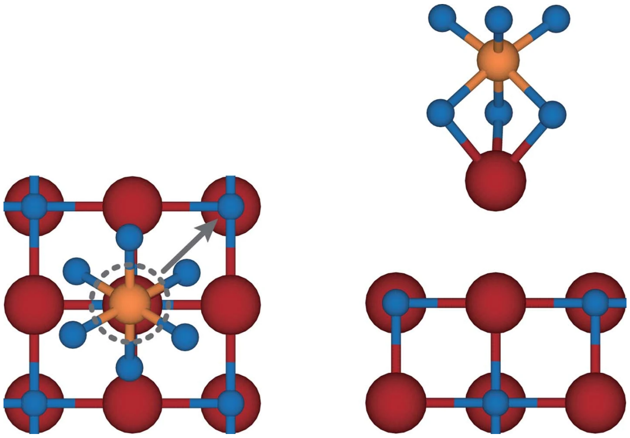

Figure H.4: Ion migration along LiF surface modeled by adsorbed $LiPF_6$.

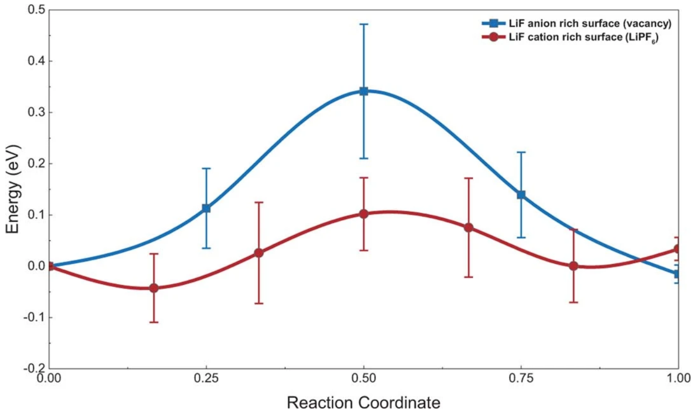

Figure H.5: Minimum energy pathways for Li^+ motion on both anion and cation-rich LiF surfaces obtained from nudged elastic band (NEB) simulations using the BEEF-vdW functional. The hopping barrier for the cation-rich system was calculated to be 0.14 ± 0.07 eV.

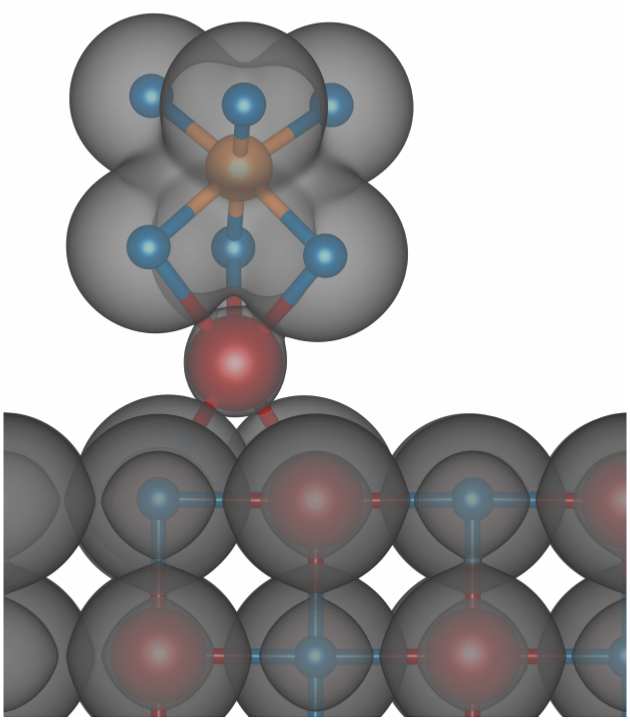

Figure H.6: Visual representation of Bader charge isosurfaces of the cation-rich system. The total molar volume ratio calculated for this system was 0.18, placing it in the dendrite-suppressing stability regime

Appendix I

Impacts of the Space Charge Layer

As discussed in section 1.2.2, most electrolytes are unstable to the anodes reducing capabilities and decompose to form the SEI. Due to the inhomogenous nature of this thin film (Figure 1.3), it becomes critical to find design principles for multiphase solid ion conductors, either artificially created or naturally generated at the electrode-electrolyte interface. It has already been shown that current tradeoffs associated with property optimization can be avoided by careful use of phase boundaries through the creation of space charge regions, [200] confinement, ion adsorption, among others. For example, Li-ion conductivity in the two-phase system LiI/Al_2O_3 is anomalously high compared to the same value in either individual phase, [85] an effect explained by the formation of space charge regions, which cause Li-ions to migrate to the interface with Al_2O_3, thus generating additional Li^+ vacancies in LiI.

Recent studies [93] have further elucidated the role of space charge layers in enhancing the ionic conductivity by investigating the synergistic behavior between two SEI phases, LiF and Li_2CO_3. As shown in Fig. I.1, Li ions migrate from LiF to Li_2CO_3, resulting in the generation of interstitial Li in Li_2CO_3, responsible for enhanced conduction, a phenomenon explained by the Nernst-Einstein equation, shown in Equation I.1. In it, σ_i is the conductivity of species i, q_i, its charge, D_i is its diffusivity, and n_i is its concentration. The constants F and R are Faraday's constant and the universal gas constant, respectively, with T being the temperature of the system.

$$\sigma_i = \frac{q_i^2 F^2 D_i}{RT} n_i \tag{I.1}$$

This mechanism was also covered in Section 3.2.1. Theoretical considerations regarding the space-charge phenomenon are discussed in this Appendix.

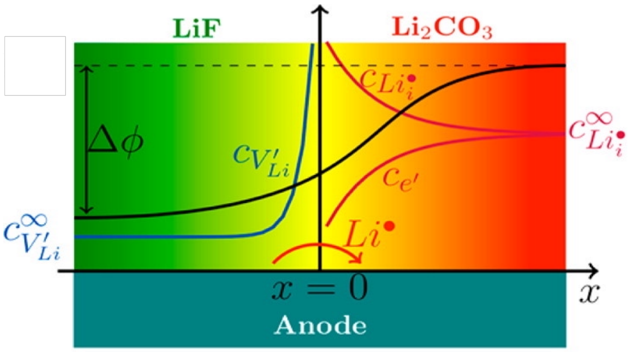

Figure I.1: Defect generation at the LiF/Li_2CO_3 interface. [93]

I.1 Theory of Heterojunctions

The interface of two crystalline semiconductors with different band gaps is called a heterojunction. In equilibrium, the electrochemical potential of the electrons needs to be constant. Therefore, if two phases with different Fermi levels are brought together, electrons will migrate from the one with highest Fermi level to the one with lowest Fermi level. By filling the unoccupied bands of the receiving phase, the migrating electrons raise its Fermi level. At the same time, they lower the Fermi level on the donating material. This electron exchange generates an accumulation of charge at different regions of the junction: the donating phase is positively charged near the interface due to the holes left behind, while the receiving phase becomes negatively charged due to the extra electrons. This local charge imbalance gives rise to an electrical potential ϕ, responsible for the phenomenon called band bending, discussed below.

For wide band gap ($E_G \gg k_BT \approx 0.0258$ eV at room temperature) semiconductors and insulators, the number of electrons in the conduction band (n_C) and holes in the valence band (p_V) can be calculated with the following relationship:

$$n_C(\vec{r}) = N_C(\vec{r}) \exp\left[-\beta(E_C(\vec{r}) - e\phi(\vec{r}) - \mu_e)\right], \tag{I.2}$$

$$p_V(\vec{r}) = P_V(\vec{r}) \exp\left[-\beta(\mu_e + e\phi(\vec{r}) - E_V(\vec{r}))\right], \tag{I.3}$$

where $\vec{r}$ is the position in space, $\beta = (k_BT)^{-1}$, μ_e is the constant electron Fermi level, e is the electron elementary charge, ϕ is the electrostatic potential developed, E_C and E_V correspond to the conduction band minimum and valence band maximum, respectively, and vary in space $\vec{r}$ due to the presence of different materials. Additionally,

$$N_C(\vec{r}) = \int_{E_C}^{\infty} g_C(\epsilon) \exp\left[-\beta(\epsilon - E_C)\right] d\epsilon, \tag{I.4}$$

$$P_V(\vec{r}) = \int_{-\infty}^{E_V} g_V(\epsilon) \exp\left[-\beta(E_V - \epsilon)\right] d\epsilon, \tag{I.5}$$

where g_C and g_V are the density of states in the conduction and valence bands, respectively. While further approximations exist for both N_C and P_V, these values can also be obtained directly from DFT calculations. Note that the relations above only hold for wide band gaps, since they rely on the approximations $\exp\left[\beta(\epsilon - \mu_e)\right] \gg 1$ for $\epsilon \geq E_C$ and $\exp\left[\beta(\mu_e - \epsilon)\right] \gg 1$ for $\epsilon \leq E_V$.

Traditionally, the solutions for $n_C(\vec{r})$, $p_V(\vec{r})$, and $\phi(\vec{r})$ are obtained consistently with Poisson's equation:

$$\nabla^2\phi(\vec{r}) = -\frac{4\pi\rho(\vec{r})}{\epsilon(\vec{r})}, \tag{I.6}$$

where ϵ is the dialectric constant of the medium (varying over $\vec{r}$ due to different materials, but assumed constant within each phase), and ρ is the charge density, given by

$$\rho(\vec{r}) = e\left[-n_C(\vec{r}) + p_V(\vec{r})\right] \tag{I.7}$$

The possibility of existence of charged defects, however, adds a layer of complexity over this analysis, since, similar to electrons and holes, the defect concentration impacts the overall charge density ρ, while at the same time relying on both the electron Fermi level and on the electrostatic potential.

I.2 Impact of Charged Defects

For the purposes of Li-ion conductivity through SEI materials, the most relevant defects to be considered are point defects, in particular, Li vacancies and interstitial atoms. Under the dilute limit assumption, the concentration of defects of a given type i can be calculated using

$$n_i(\vec{r}) = S_i(\vec{r}) \exp\left[-\beta E_i^f(\vec{r})\right], \tag{I.8}$$

where S_i is the density of sites where the defect can occur, and E_i^f is the defect formation energy. First-principles based computations of E_i^f rely on the following equation: [201]

$$E_i^f(\vec{r}) = E_{DFT}[X^{q_i}] - \left[E_{DFT}[pristine] + \sum N_i\mu_i - q_i(\mu_e + \Delta\epsilon)\right] + q_i\phi(\vec{r}) \tag{I.9}$$

Here, E_{DFT} is the DFT-calculated energy for a pristine structure and for the one containing the charged defect X^{q_i} with charge q_i. The summation term accounts for the addition ($N_i > 0$) or removal ($N_i < 0$) of species, with μ_i corresponding to the each species chemical potential. The $q_i\mu_e$ term accounts for the fact that the defect must exchange an electron with the overall phase in order to be charged. $\Delta\epsilon$ corresponds to additional corrections to the expression, accounting for a variety of factors such as Coulombic interaction between periodic images of the defect, etc., and its details lie beyond the scope of this work. Note that $n_i(\vec{r})$ has an exponential dependence with the electrostatic potential ϕ. Customarily, the solution for n_i is found by considering all possible charged defects present in a material and adjusting the position of the Fermi level to ensure overall charge neutrality, something that is a requirement for the entire SEI, but not for each individual piece of the SEI mosaic (Figure 1.3).

Incorporating the defect concentrations to the previous expression of charge density (Equation I.7) yields

$$\rho(\vec{r}) = e\left[-n_C(\vec{r}) + p_V(\vec{r})\right] + \sum_i q_i n_i(\vec{r}) \tag{I.10}$$

This formalism allows the investigation of the relationship between heterojunctions present in Li-ion batteries and charged defects — essential for Li-ion transport through the SEI and inorganic solid electrolytes. A way of performing this self-consistent analysis is proposed in Appendix K.

Appendix J

Li-ion Minimum Energy Pathway at LiF-Li_2CO_3 Interface

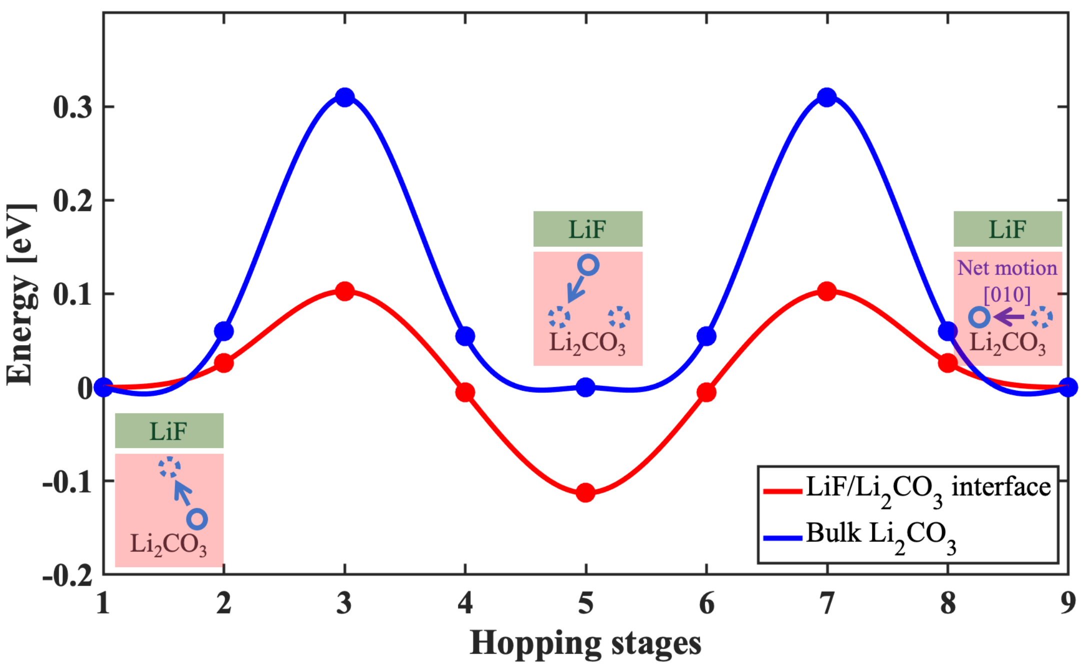

Figure J.1: Minimum energy pathway for lithium migration between two equivalent interstitial sites (stages 1 and 9) in Li_2CO_3 near its interface with LiF (red), and energy landscape for the corresponding motion in bulk Li_2CO_3 (blue). The net total Li^+ motion happens along the [010] direction.

Appendix K

Finite Element Poisson Solver

While there exist several finite element (FE) Poisson solvers in multiple software packages, including, but not limited to, Python, MATLAB, Mathematica, etc., preliminary results suggest these solvers are not sufficiently customizable for the analysis discussed in Section I.2. The following iterative approach appears to be a promising alternative.

The main equation to be solved, Poisson's Equation I.6, can be rewritten as:

$$\nabla^2 \phi + \frac{4\pi}{\epsilon} \rho(\phi) = 0 \tag{K.1}$$

Assume there exists a solution $\mathbf{\Phi}$ that satisfies this equation, as well as all the necessary constraints. If a solution ϕ_i is guessed, its error can be calculated with $\delta\phi_i = \mathbf{\Phi} - \phi_i$. Therefore,

$$\nabla^2(\phi_i + \delta\phi_i) + \frac{4\pi}{\epsilon} \rho(\phi_i + \delta\phi_i) = 0 \tag{K.2}$$

A first-order Taylor expansion on ρ gives:

$$\nabla^2 \delta\phi_i + \frac{4\pi}{\epsilon} \left.\frac{d\rho}{d\phi}\right|_{\phi_i} (\delta\phi_i) = -\nabla^2 \phi_i - \frac{4\pi}{\epsilon} \rho(\phi_i) \tag{K.3}$$

Updating the boundary conditions such that $(\delta\phi_i)|_{\partial\Omega} = (\mathbf{\Phi} - \phi_i)|_{\partial\Omega}$, it should be possible to use standard Poisson solvers to solve for $\delta\phi_i$ until convergence of $\phi_i \to \mathbf{\Phi}$.

Appendix L

Computational Parameter Estimation for Regular Solution Model

In order to estimate the different regular solution parameters needed for the regular solution model, density functional theory (DFT), coupled with the Perdew, Burke, and Ernzerhof (PBE) exchange correlation functional [94] in the projector augmented wave (PAW) code GPAW [73] was employed. The structures used were all slabs of at least 4 layers, with the bottom 2 layers kept fixed as to emulate bulk lithium, and can be seen in Figure L.1. A 10 Å vacuum was applied, alongside a real-space grid spacing of 0.16 Å and a Monkhorst Pack scheme [202] sampling of the Brillouin zone with k-point density of 6 Å^{-1}. All calculations were converged to energy < 0.5 meV and force < 0.05 eV·Å^{-1}.

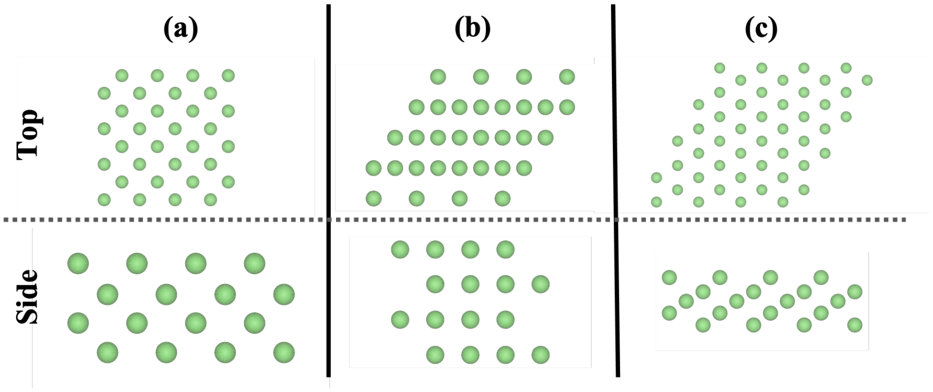

Figure L.1: Top and side views of the structures used to calculate interaction parameters for the **(a)** (100), **(b)** (110), and **(c)** (111) surface facets. All structures had a minimum of 4 layers, and the bottom two layers of each structures were kept fixed to properly emulate bulk lithium. [122]

To estimate the interaction parameters, systems with only one vacancy were created, allowing the evaluation, for each facet, of the value of $\epsilon_{VL} - \epsilon_{LL}$: the difference in energy between the pristine system and that with a vacancy is given by $E_{\text{single vacancy}} - E_{\text{pristine}} = z\,(\epsilon_{VL} - \epsilon_{LL})$. Next, by incorporating a second vacancy neighboring the first one, the value of $\epsilon_{VV} - \epsilon_{LL}$ can be computed: $E_{\text{two vacancies}} - E_{\text{pristine}} = 2(z-1)\,(\epsilon_{VL} - \epsilon_{LL}) + (\epsilon_{VV} - \epsilon_{LL})$. Finally, the calculation of the full interaction parameter can be done with:

$$\Omega = \frac{z}{2}\left[2(\epsilon_{VL} - \epsilon_{LL}) - (\epsilon_{VV} - \epsilon_{LL})\right] = \frac{z}{2}(2\epsilon_{VL} - \epsilon_{VV} - \epsilon_{LL}).$$

Bibliography

[1] J. Dahn and G. M. Ehrlich, in *Linden's Handbook of Batteries*, edited by T. B. Reddy and D. Linden (McGraw Hill Professional, New York, 2011).

[2] S. Sripad and V. Viswanathan, ACS Energy Lett. **2**, 1669 (2017).

[3] W. L. Fredericks, S. Sripad, G. C. Bower, and V. Viswanathan, ACS Energy Lett. **3**, 2989 (2018).

[4] A. H. Epstein and S. M. O'Flarity, J. Propul. Power **35**, 572 (2019).

[5] A. Bills, S. Sripad, W. L. Fredericks, M. Guttenberg, D. Charles, E. Frank, and V. Viswanathan, arXiv preprint arXiv:2008.01527 (2020).

[6] W. Xu, J. Wang, F. Ding, X. Chen, E. Nasybulin, Y. Zhang, and J.-G. Zhang, Energy Environ. Sci. **7**, 513 (2014).

[7] D. Lin, Y. Liu, and Y. Cui, Nat. Nanotechnol. **12**, 194 (2017).

[8] C. Fu, V. Venturi, J. Kim, Z. Ahmad, A. W. Ells, V. Viswanathan, and B. A. Helms, Nat. Mater. **19**, 758 (2020).

[9] A. Bhowmik, I. E. Castelli, J. M. Garcia-Lastra, P. B. Jørgensen, O. Winther, and T. Vegge, Energy Storage Mater **21**, 446 (2019).

[10] A. Sharafi, E. Kazyak, A. L. Davis, S. Yu, T. Thompson, D. J. Siegel, N. P. Dasgupta, and J. Sakamoto, Chem. Mater. **29**, 7961 (2017).

[11] K. S. Exner, ChemElectroChem **4**, 3231 (2017).

[12] M. A. Gialampouki, J. Hashemi, and A. A. Peterson, J Phys Chem C **123**, 20084 (2019).

[13] K. Xu, Chem. Rev. **104**, 4303 (2004).

[14] R. V. Noorden, Nature **507**, 26 (2014).

[15] J. W. Choi and D. Aurbach, Nat. Rev. Mater. **1** (2016).

[16] C. Xu, Z. Ahmad, A. Aryanfar, V. Viswanathan, and J. R. Greer, PNAS **114**, 57 (2017).

[17] X.-B. Cheng, R. Zhang, C.-Z. Zhao, and Q. Zhang, Chem. Rev. **117**, 10403 (2017).

[18] D. Aurbach, B. Markovsky, A. Shechter, Y. Ein-Eli, and H. Cohen, J. Electrochem. Soc. **143**, 3809 (1996).

[19] T. Hirai, I. Yoshimatsu, and J.-i. Yamaki, J. Electrochem. Soc. **141**, 2300 (1994).

[20] F. Ding, W. Xu, G. L. Graff, J. Zhang, M. L. Sushko, X. Chen, Y. Shao, M. H. Engelhard, Z. Nie, J. Xiao, X. Liu, P. V. Sushko, J. Liu, and J.-G. Zhang, J. Am. Chem. Soc. **135**, 4450 (2013).

[21] J. Qian, W. A. Henderson, W. Xu, P. Bhattacharya, M. Engelhard, O. Borodin, and J.-G. Zhang, Nat. Commun. **6**, 6362 (2015).

[22] L. Suo, Y.-S. Hu, H. Li, M. Armand, and L. Chen, Nat. Commun. **4**, 1481 (2013).

[23] Y. Lu, Z. Tu, and L. A. Archer, Nat. Mater. **13**, 961 (2014).

[24] X.-Q. Zhang, X.-B. Cheng, X. Chen, C. Yan, and Q. Zhang, Adv. Funct. Mater. **27**, 1605989 (2017).

[25] D. Wang, W. Zhang, W. Zheng, X. Cui, T. Rojo, and Q. Zhang, Adv. Sci. **4**, 1600168 (2017).

[26] Y. Zhang, J. Qian, W. Xu, S. M. Russell, X. Chen, E. Nasybulin, P. Bhattacharya, M. H. Engelhard, D. Mei, R. Cao, F. Ding, A. V. Cresce, K. Xu, and J.-G. Zhang, Nano Lett. **14**, 6889 (2014).

[27] M. Z. Mayers, J. W. Kaminski, and T. F. Miller, J. Phys. Chem. C **116**, 26214 (2012).

[28] A. Aryanfar, D. Brooks, B. V. Merinov, W. A. Goddard, A. J. Colussi, and M. R. Hoffmann, J. Phys. Chem. Lett. **5**, 1721 (2014).

[29] Q.-C. Liu, J.-J. Xu, S. Yuan, Z.-W. Chang, D. Xu, Y.-B. Yin, L. Li, H.-X. Zhong, Y.-S. Jiang, J.-M. Yan, and X.-B. Zhang, Adv. Mater. **27**, 5241 (2015).

[30] K. Yan, H.-W. Lee, T. Gao, G. Zheng, H. Yao, H. Wang, Z. Lu, Y. Zhou, Z. Liang, Z. Liu, S. Chu, and Y. Cui, Nano Lett. **14**, 6016 (2014).

[31] Y. Liu, D. Lin, P. Y. Yuen, K. Liu, J. Xie, R. H. Dauskardt, and Y. Cui, Adv. Mater. **29**, 1605531 (2017).

[32] R. Khurana, J. L. Schaefer, L. A. Archer, and G. W. Coates, J. Am. Chem. Soc. **136**, 7395 (2014).

[33] G. M. Stone, S. A. Mullin, A. A. Teran, D. T. Hallinan, A. M. Minor, A. Hexemer, and N. P. Balsara, J. Electrochem. Soc. **159**, A222 (2012).

[34] L. Yue, J. Ma, J. Zhang, J. Zhao, S. Dong, Z. Liu, G. Cui, and L. Chen, Energy Storage Mater. **5**, 139 (2016).

[35] J. Janek and W. G. Zeier, Nat Energy **1**, 1 (2016).

[36] Y. Suzuki, K. Kami, K. Watanabe, A. Watanabe, N. Saito, T. Ohnishi, K. Takada, R. Sudo, and N. Imanishi, Solid State Ionics **278**, 172 (2015).

[37] J. Li, C. Ma, M. Chi, C. Liang, and N. J. Dudney, Advanced Energy Materials **5**, 1401408 (2015).

[38] A. Manthiram, X. Yu, and S. Wang, Nat. Rev. Mater. **2**, 16103 (2017).

[39] N. Kamaya, K. Homma, Y. Yamakawa, M. Hirayama, R. Kanno, M. Yonemura, T. Kamiyama, Y. Kato, S. Hama, K. Kawamoto, and A. Mitsui, Nat. Mater. **10**, 682 (2011).

[40] Y. Seino, T. Ota, K. Takada, A. Hayashi, and M. Tatsumisago, Energy Environ. Sci. **7**, 627 (2014).

[41] Y. Zhao and L. L. Daemen, J. Am. Chem. Soc. **134**, 15042 (2012).

[42] Y. Zhang, Y. Zhao, and C. Chen, Phys. Rev. B **87**, 10.1103/physrevb.87.134303 (2013).

[43] V. Thangadurai, H. Kaack, and W. J. F. Weppner, J. Am. Ceram. Soc. **86**, 437 (2003).

[44] R. Murugan, V. Thangadurai, and W. Weppner, Angew. Chem. - Int. Ed. **46**, 7778 (2007).

[45] Z. Ahmad and V. Viswanathan, Phys. Rev. Lett. **119**, 056003 (2017).

[46] C. Monroe and J. Newman, J. Electrochem. Soc. **152**, A396 (2005).

[47] Y. Zhu, X. He, and Y. Mo, ACS Appl. Mater. Interfaces **7**, 23685 (2015).

[48] E. Peled, J. Electrochem. Soc. **126**, 2047 (1979).

[49] E. Peled, D. Golodnitsky, and G. Ardel, J. Electrochem. Soc. **144**, L208 (1997).

[50] M. Winter, Z. Phys. Chem. **223**, 1395 (2009).

[51] Z. Ahmad, V. Venturi, S. Sripad, and V. Viswanathan, Current Opinion in Solid State and Materials Science **26**, 101002 (2022).

[52] K. S. Novoselov, A. Mishchenko, A. Carvalho, and A. H. C. Neto, Science **353**, aac9439 (2016).

[53] X. Zhang, L. Hou, A. Ciesielski, and P. Samorì, Adv. Energy Mater. **6**, 1600671 (2016).

[54] E. Quesnel, F. Roux, F. Emieux, P. Faucherand, E. Kymakis, G. Volonakis, F. Giustino, B. Martín-García, I. Moreels, S. A. Gürsel, A. B. Yurtcan, V. D. Noto, A. Talyzin, I. Baburin, D. Tranca, G. Seifert, L. Crema, G. Speranza, V. Tozzini, P. Bondavalli, G. Pognon, C. Botas, D. Carriazo, G. Singh, T. Rojo, G. Kim, W. Yu, C. P. Grey, and V. Pellegrini, 2D Materials **2**, 030204 (2015).

[55] M. Ge, C. Cao, J. Huang, S. Li, Z. Chen, K.-Q. Zhang, S. S. Al-Deyab, and Y. Lai, J. Mater. Chem. A **4**, 6772 (2016).

[56] A. K. Geim and I. V. Grigorieva, Nature **499**, 419 (2013).

[57] K. Novoselov and A. C. Neto, Phys Scr **2012**, 014006 (2012).

[58] M. S. Whittingham and F. R. Gamble Jr, Materials research bulletin **10**, 363 (1975).

[59] K. Hermann, J. Phys.: Condens. Matter **24**, 314210 (2012).

[60] M. Van Wijk, A. Schuring, M. Katsnelson, and A. Fasolino, 2D Mater. **2**, 034010 (2015).

[61] P. Pochet, B. C. McGuigan, J. Coraux, and H. T. Johnson, Appl. Mater. Today **9**, 240 (2017).

[62] S. Dai, Y. Xiang, and D. J. Srolovitz, Nano letters **16**, 5923 (2016).

[63] Y. Cao, V. Fatemi, S. Fang, K. Watanabe, T. Taniguchi, E. Kaxiras, and P. Jarillo-Herrero, Nature **556**, 43 (2018).

[64] R. Bistritzer and A. H. MacDonald, Proceedings of the National Academy of Sciences **108**, 12233 (2011).

[65] D. T. Larson, I. Fampiou, G. Kim, and E. Kaxiras, J. Phys. Chem. C **122**, 24535 (2018).

[66] D. K. Bediako, M. Rezaee, H. Yoo, D. T. Larson, S. F. Zhao, T. Taniguchi, K. Watanabe, T. L. Brower-Thomas, E. Kaxiras, and P. Kim, Nature **558**, 425 (2018).

[67] J. Lu, P. S. E. Yeo, Y. Zheng, Z. Yang, Q. Bao, C. K. Gan, and K. P. Loh, ACS Nano **6**, 944 (2012).

[68] V. Pande and V. Viswanathan, Phys. Rev. Mater. **2**, 125401 (2018).

[69] M. S. Whittingham, *Intercalation Chemistry* (Elsevier, 2012).

[70] D. T. Larson, S. Carr, G. A. Tritsaris, and E. Kaxiras, Phys. Rev. B **101**, 075407 (2020).

[71] K. Zhang and E. B. Tadmor, J. Mech. Phys. Solids. **112**, 225 (2018).

[72] G. Ceder, M. Aydinol, and A. Kohan, Comput. Mater. Sci. **8**, 161 (1997).

[73] J. Enkovaara, C. Rostgaard, J. J. Mortensen, J. Chen, M. Dułak, L. Ferrighi, J. Gavnholt, C. Glinsvad, V. Haikola, H. Hansen, *et al.*, J. Phys.: Condens. Matter **22**, 253202 (2010).

[74] J. Wellendorff, K. T. Lundgaard, A. Møgelhøj, V. Petzold, D. D. Landis, J. K. Nørskov, T. Bligaard, and K. W. Jacobsen, Phys. Rev. B **85**, 235149 (2012).

[75] Y. Imai and A. Watanabe, J. Alloys Compd. **439**, 258 (2007).

[76] D. DiVincenzo, C. Fuerst, and J. Fischer, Phys. Rev. B **29**, 1115 (1984).

[77] S. Shallcross, S. Sharma, E. Kandelaki, and O. Pankratov, Phys. Rev. B **81**, 165105 (2010).

[78] K. Persson, Y. Hinuma, Y. S. Meng, A. Van der Ven, and G. Ceder, Phys. Rev. B **82**, 125416 (2010).

[79] Y. Okamoto, J. Phys. Chem. C **118**, 16 (2014).

[80] E. Hazrati, G. De Wijs, and G. Brocks, Phys. Rev. B **90**, 155448 (2014).

[81] T. Editors of Britannica, Steel - History, https://www.britannica.com/technology/steel (1999).

[82] C. Monroe and J. Newman, J. Electrochem. Soc. **150**, A1377 (2003).

[83] C. Monroe and J. Newman, J. Electrochem. Soc. **151**, A880 (2004).

[84] K. J. Harry, D. T. Hallinan, D. Y. Parkinson, A. A. Macdowell, and N. P. Balsara, Nat. Mater. **13**, 69 (2014).

[85] C. C. Liang, J. Electrochem. Soc. **120**, 1289 (1973).

[86] S. Wei, Z. Cheng, P. Nath, M. D. Tikekar, G. Li, and L. A. Archer, Sci. Adv. **4**, eaao6243 (2018).

[87] S. Plimpton, Journal of Computational Physics **117**, 1 (1995).

[88] S. L. Mayo, B. D. Olafson, and W. A. Goddard, J. Phys. Chem. **94**, 8897 (1990).

[89] J. Newman and T. W. Chapman, AIChE Journal **19**, 343 (1973).

[90] H. Jonsson, G. Mills, and K. W. Jacobsen, *Classical and Quantum Dynamics in Condensed Phase Simulations: Proceedings of the International School of Physics*, edited by B. J. Berne, G. Ciccotti, and D. F. Coker (World Scientific, 1998).

[91] S. Mallikarjun Sharada, T. Bligaard, A. C. Luntz, G.-J. Kroes, and J. K. Nørskov, J. Phys. Chem. C **121**, 19807 (2017).

[92] R. F. W. Bader, *Atoms in Molecules: A Quantum Theory*, The International Series of Monographs on Chemistry No. 22 (Clarendon Press ; Oxford University Press, Oxford [England] : New York, 1994).

[93] Q. Zhang, J. Pan, P. Lu, Z. Liu, M. W. Verbrugge, B. W. Sheldon, Y.-T. Cheng, Y. Qi, and X. Xiao, Nano Lett. **16**, 2011 (2016).

[94] J. P. Perdew, K. Burke, and M. Ernzerhof, Phys Rev Lett **77**, 3865 (1996).

[95] R. Tran, Z. Xu, B. Radhakrishnan, D. Winston, W. Sun, K. A. Persson, and S. P. Ong, Sci. Data **3**, 160080 (2016).

[96] W. Sun and G. Ceder, Surf. Sci. **617**, 53 (2013).

[97] S. P. Ong, W. D. Richards, A. Jain, G. Hautier, M. Kocher, S. Cholia, D. Gunter, V. L. Chevrier, K. A. Persson, and G. Ceder, Comput. Mater. Sci. **68**, 314 (2013).

[98] A. H. Larsen, J. J. Mortensen, J. Blomqvist, I. E. Castelli, R. Christensen, M. Dułak, J. Friis, M. N. Groves, B. Hammer, C. Hargus, E. D. Hermes, P. C. Jennings, P. B. Jensen, J. Kermode, J. R. Kitchin, E. L. Kolsbjerg, J. Kubal, K. Kaasbjerg, S. Lysgaard, J. B. Maronsson, T. Maxson, T. Olsen, L. Pastewka, A. Peterson, C. Rostgaard, J. Schiøtz, O. Schütt, M. Strange, K. S. Thygesen, T. Vegge, L. Vilhelmsen, M. Walter, Z. Zeng, and K. W. Jacobsen, J. Phys. Condens. Matter **29**, 273002 (2017).

[99] J. Pan, Q. Zhang, X. Xiao, Y.-T. Cheng, and Y. Qi, ACS Appl. Mater. Interfaces **8**, 5687 (2016).

[100] Z. Ahmad, V. Venturi, H. Hafiz, and V. Viswanathan, J. Phys. Chem. C **125**, 11301 (2021).

[101] S. Shi, Y. Qi, H. Li, and L. G. Hector, J. Phys. Chem. C **117**, 8579 (2013).

[102] S. Shi, P. Lu, Z. Liu, Y. Qi, L. G. Hector, H. Li, and S. J. Harris, J. Am. Chem. Soc. **134**, 15476 (2012).

[103] H. Iddir and L. A. Curtiss, J. Phys. Chem. C **114**, 20903 (2010).

[104] M. J. Wang, R. Choudhury, and J. Sakamoto, Joule **3**, 2165 (2019).

[105] K. N. Wood, E. Kazyak, A. F. Chadwick, K.-H. Chen, J.-G. Zhang, K. Thornton, and N. P. Dasgupta, ACS Cent. Sci. **2**, 790 (2016).

[106] Y. S. Cohen, Y. Cohen, and D. Aurbach, J. Phys. Chem. B **104**, 12282 (2000).

[107] F. Shi, A. Pei, D. T. Boyle, J. Xie, X. Yu, X. Zhang, and Y. Cui, Proc Natl Acad Sci U S A **115**, 8529 (2018).

[108] L. Gireaud, S. Grugeon, S. Laruelle, B. Yrieix, and J. M. Tarascon, Electrochemistry Communications **8**, 1639 (2006).

[109] J. Kasemchainan, S. Zekoll, D. Spencer Jolly, Z. Ning, G. O. Hartley, J. Marrow, and P. G. Bruce, Nat. Mater. **18**, 1105 (2019).

[110] V. Raj, V. Venturi, V. R. Kankanallu, B. Kuiri, V. Viswanathan, and N. P. B. Aetukuri, Nat. Mater. , 1 (2022).

[111] T. Krauskopf, H. Hartmann, W. G. Zeier, and J. Janek, ACS Appl. Mater. Interfaces **11**, 14463 (2019).

[112] A. J. Sanchez, E. Kazyak, Y. Chen, J. Lasso, and N. P. Dasgupta, J. Mater. Chem. A 10.1039/D1TA03333F (2021).

[113] A. J. Sanchez, E. Kazyak, Y. Chen, K.-H. Chen, E. R. Pattison, and N. P. Dasgupta, ACS Energy Lett. **5**, 994 (2020).

[114] C.-T. Yang and Y. Qi, Chem. Mater. **33**, 2814 (2021).

[115] M. Yang and Y. Mo, Angewandte Chemie International Edition **60**, 21494 (2021).

[116] H. Yan, K. Tantratian, K. Ellwood, E. T. Harrison, M. Nichols, X. Cui, and L. Chen, Advanced Energy Materials **12**, 2102283 (2022).

[117] H. K. Hardy, Acta Metallurgica **1**, 202 (1953).

[118] J. E. Morral and S. Chen, J. Phase Equilib. Diffus. **38**, 382 (2017).

[119] T. Murakami, S. Ono, M. Tamura, and M. Kurata, J. Phys. Soc. Jpn. **6**, 309 (1951).

[120] G. Barbero, L. R. Evangelista, and I. Lelidis, Journal of Molecular Liquids **327**, 114795 (2021).

[121] P. R. Cantwell, M. Tang, S. J. Dillon, J. Luo, G. S. Rohrer, and M. P. Harmer, Acta Materialia **62**, 1 (2014).

[122] V. Venturi and V. Viswanathan, ACS Energy Lett. , 1953 (2022).

[123] F. Shi, A. Pei, A. Vailionis, J. Xie, B. Liu, J. Zhao, Y. Gong, and Y. Cui, Proc Natl Acad Sci U S A **114**, 12138 (2017).

[124] X. Han, Y. Gong, K. K. Fu, X. He, G. T. Hitz, J. Dai, A. Pearse, B. Liu, H. Wang, G. Rubloff, Y. Mo, V. Thangadurai, E. D. Wachsman, and L. Hu, Nature Mater **16**, 572 (2017).

[125] Y. Lu, X. Huang, Y. Ruan, Q. Wang, R. Kun, J. Yang, and Z. Wen, J. Mater. Chem. A **6**, 18853 (2018).

[126] C. Wang, Y. Gong, B. Liu, K. Fu, Y. Yao, E. Hitz, Y. Li, J. Dai, S. Xu, W. Luo, E. D. Wachsman, and L. Hu, Nano Lett. **17**, 565 (2017).

[127] K. K. Fu, Y. Gong, B. Liu, Y. Zhu, S. Xu, Y. Yao, W. Luo, C. Wang, S. D. Lacey, J. Dai, Y. Chen, Y. Mo, E. Wachsman, and L. Hu, Science Advances **3**, e1601659 (2017).

[128] C. Fiolhais, L. M. Almeida, and C. Henriques, Progress in Surface Science Maria Steslicka Memorial Volume, **74**, 209 (2003).

[129] Z. A. Piazza, M. Ajmalghan, Y. Ferro, and R. D. Kolasinski, Acta Materialia **145**, 388 (2018).

[130] F. J. Q. Cortes, J. A. Lewis, J. Tippens, T. S. Marchese, and M. T. McDowell, J. Electrochem. Soc. **167**, 050502 (2019).

[131] K. N. Wood, M. Noked, and N. P. Dasgupta, ACS Energy Lett. **2**, 664 (2017).

[132] A. Bills, S. Sripad, W. L. Fredericks, M. Singh, and V. Viswanathan, ACS Energy Lett. **5**, 663 (2020).

[133] V. Pande and V. Viswanathan, ACS Energy Lett. **4**, 2952 (2019).

[134] R. Kurchin and V. Viswanathan, J. Chem. Phys. **153**, 134706 (2020).

[135] V. A. Kislenko, S. V. Pavlov, and S. A. Kislenko, Electrochimica Acta **341**, 136011 (2020).

[136] E. Olivetti, J. Gregory, and R. Kirchain, Massachusetts Institute of Technology: Cambridge, MA, USA (2011).

[137] Y. Zuo, M. Qin, C. Chen, W. Ye, X. Li, J. Luo, and S. P. Ong, Materials Today **51**, 126 (2021).

[138] C. Chen and S. P. Ong, A Universal Graph Deep Learning Interatomic Potential for the Periodic Table (2022).

[139] S. Yu and D. J. Siegel, ACS Appl. Mater. Interfaces **10**, 38151 (2018).

[140] H.-K. Tian, Z. Liu, Y. Ji, L.-Q. Chen, and Y. Qi, Chem. Mater. **31**, 7351 (2019).

[141] V. Venturi, H. L. Parks, Z. Ahmad, and V. Viswanathan, Mach. Learn.: Sci. Technol. **1**, 035015 (2020).

[142] V. Venturi and V. Viswanathan, J. Electrochem. Soc. **168**, 070544 (2021).

[143] N. Mounet, M. Gibertini, P. Schwaller, D. Campi, A. Merkys, A. Marrazzo, T. Sohier, I. E. Castelli, A. Cepellotti, G. Pizzi, and N. Marzari, Nat. Nanotechnol. **13**, 246 (2018).

[144] Z. Xiao, W. Meng, B. Saparov, H.-S. Duan, C. Wang, C. Feng, W. Liao, W. Ke, D. Zhao, J. Wang, D. B. Mitzi, and Y. Yan, J. Phys. Chem. Lett. **7**, 1213 (2016).

[145] J. Pang, R. G. Mendes, A. Bachmatiuk, L. Zhao, H. Q. Ta, T. Gemming, H. Liu, Z. Liu, and M. H. Rummeli, Chem. Soc. Rev. **48**, 72 (2019).

[146] D. Er, J. Li, M. Naguib, Y. Gogotsi, and V. B. Shenoy, ACS Appl. Mater. Interfaces **6**, 11173 (2014).

[147] N. K. Chaudhari, H. Jin, B. Kim, D. S. Baek, S. H. Joo, and K. Lee, J. Mater. Chem. A **5**, 24564 (2017).

[148] A. Lipatov, H. Lu, M. Alhabeb, B. Anasori, A. Gruverman, Y. Gogotsi, and A. Sinitskii, Sci. Adv. **4**, eaat0491 (2018).

[149] L. Himanen, A. Geurts, A. S. Foster, and P. Rinke, Adv. Sci. **6**, 1900808 (2019).

[150] M. Umehara, H. S. Stein, D. Guevarra, P. F. Newhouse, D. A. Boyd, and J. M. Gregoire, npj Comput. Mater. **5**, 10.1038/s41524-019-0172-5 (2019).

[151] C. W. Coley, R. Barzilay, T. S. Jaakkola, W. H. Green, and K. F. Jensen, ACS Cent. Sci. **3**, 434 (2017).

[152] J. D. Evans and F.-X. Coudert, Chem. Mater. **29**, 7833 (2017).

[153] A. D. Sendek, Q. Yang, E. D. Cubuk, K.-A. N. Duerloo, Y. Cui, and E. J. Reed, Energy Environ. Sci. **10**, 306 (2017).

[154] Z. Ahmad, T. Xie, C. Maheshwari, J. C. Grossman, and V. Viswanathan, ACS Cent. Sci. **4**, 996 (2018).

[155] T. Mazaheri, B. Sun, J. Scher-Zagier, A. Thind, D. Magee, P. Ronhovde, T. Lookman, R. Mishra, and Z. Nussinov, Physical Review Materials **3**, 063802 (2019).

[156] G. Pilania, C. Wang, X. Jiang, S. Rajasekaran, and R. Ramprasad, Sci. Rep. **3**, 2810 (2013).

[157] K. Fujimura, A. Seko, Y. Koyama, A. Kuwabara, I. Kishida, K. Shitara, C. A. J. Fisher, H. Moriwake, and I. Tanaka, Adv. Energy Mater. **3**, 980 (2013).

[158] K. Kim, L. Ward, J. He, A. Krishna, A. Agrawal, and C. Wolverton, Phys. Rev. Materials **2**, 123801 (2018).

[159] T. Xie and J. C. Grossman, Phys. Rev. Lett. **120**, 145301 (2018).

[160] K. T. Schütt, H. E. Sauceda, P.-J. Kindermans, A. Tkatchenko, and K.-R. Müller, J. Chem. Phys. **148**, 241722 (2018).

[161] C. Chen, W. Ye, Y. Zuo, C. Zheng, and S. P. Ong, Chem. Mater. **31**, 3564 (2019).

[162] S. Haastrup, M. Strange, M. Pandey, T. Deilmann, P. S. Schmidt, N. F. Hinsche, M. N. Gjerding, D. Torelli, P. M. Larsen, A. C. Riis-Jensen, J. Gath, K. W. Jacobsen, J. J. Mortensen, T. Olsen, and K. S. Thygesen, 2D Materials **5**, 042002 (2018).

[163] C. Kim, T. D. Huan, S. Krishnan, and R. Ramprasad, Sci. Data **4**, 170057 (2017).

[164] I. E. Castelli, D. D. Landis, K. S. Thygesen, S. Dahl, I. Chorkendorff, T. F. Jaramillo, and K. W. Jacobsen, Energy Environ. Sci. **5**, 9034 (2012).

[165] A. C. Rajan, A. Mishra, S. Satsangi, R. Vaish, H. Mizuseki, K.-R. Lee, and A. K. Singh, Chem. Mater. **30**, 4031 (2018).

[166] S. Goedecker, J. Chem. Phys. **120**, 9911 (2004).

[167] É. D. Murray, K. Lee, and D. C. Langreth, Journal of Chemical Theory and Computation **5**, 2754 (2009).

[168] G. Kresse and J. Furthmüller, Comput. Mater. Sci. **6**, 15 (1996).

[169] B. Hammer, L. B. Hansen, and J. K. Nørskov, Physical Review B **59**, 7413 (1999).

[170] S. Back, J. Yoon, N. Tian, W. Zhong, K. Tran, and Z. W. Ulissi, J. Phys. Chem. Lett. **10**, 4401 (2019).

[171] L. Meng, J. You, and Y. Yang, Nat. Commun. **9**, 1 (2018).

[172] G. Houchins and V. Viswanathan, Phys. Rev. B **96**, 134426 (2017).

[173] B. Anasori, M. R. Lukatskaya, and Y. Gogotsi, Nat. Rev. Mater. **2**, 10.1038/natrevmats.2016.98 (2017).

[174] F. Hao, C. C. Stoumpos, D. H. Cao, R. P. Chang, and M. G. Kanatzidis, Nat. Photonics **8**, 489 (2014).

[175] N. K. Noel, S. D. Stranks, A. Abate, C. Wehrenfennig, S. Guarnera, A.-A. Haghighirad, A. Sadhanala, G. E. Eperon, S. K. Pathak, M. B. Johnston, A. Petrozza, L. M. Herz, and H. J. Snaith, Energy Environ. Sci. **7**, 3061 (2014).

[176] Z. Yi, N. H. Ladi, X. Shai, H. Li, Y. Shen, and M. Wang, Nanoscale Adv. **1**, 1276 (2019).

[177] A. Toshniwal and V. Kheraj, Sol. Energy **149**, 54 (2017).

[178] N. A. N. Ouedraogo, Y. Chen, Y. Y. Xiao, Q. Meng, C. B. Han, H. Yan, and Y. Zhang, Nano Energy **67**, 104249 (2020).

[179] V. Kuleshov, N. Fenner, and S. Ermon, in *Proceedings of the 35th International Conference on Machine Learning*, Proceedings of Machine Learning Research, Vol. 80, edited by J. Dy and A. Krause (PMLR, Stockholmsmässan, Stockholm Sweden, 2018) pp. 2796–2804.

[180] K. Tran, W. Neiswanger, J. Yoon, E. Xing, and Z. W. Ulissi, arXiv:1912.10066 (2019).

[181] J. M. Crowley, J. Tahir-Kheli, and W. A. Goddard, J. Phys. Chem. Lett. **7**, 1198 (2016).

[182] J. E. Moussa, P. A. Schultz, and J. R. Chelikowsky, J. Chem. Phys. **136**, 204117 (2012).

[183] P. Hohenberg and W. Kohn, Phys. Rev. **136**, B864 (1964).

[184] W. Kohn and L. J. Sham, Physical review **140**, A1133 (1965).

[185] D. Hartree, in *Math. Proc. Camb. Philos. Soc*, Vol. 24 (Cambridge University Press, 1928) pp. 89–110.

[186] J. C. Stoddart and P. Hanks, J. Phys. C: Solid State Phys. **10**, 3167 (1977).

[187] J. P. Perdew and A. Zunger, Physical Review B **23**, 5048 (1981).

[188] D. M. Ceperley and B. J. Alder, Physical Review Letters **45**, 566 (1980).

[189] S. H. Vosko, L. Wilk, and M. Nusair, Canadian Journal of physics **58**, 1200 (1980).

[190] J. P. Perdew and Y. Wang, Physical review B **45**, 13244 (1992).

[191] W. Kohn, Reviews of Modern Physics **71**, 1253 (1999).

[192] Y. Wang and J. P. Perdew, Physical Review B **44**, 13298 (1991).

[193] M. Dion, H. Rydberg, E. Schröder, D. C. Langreth, and B. I. Lundqvist, Physical Rev. Lett. **92**, 246401 (2004).

[194] K. Lee, É. D. Murray, L. Kong, B. I. Lundqvist, and D. C. Langreth, Physical Review B **82**, 081101 (2010).

[195] K. Berland and P. Hyldgaard, Physical Review B **89**, 035412 (2014).

[196] J. Klimes, D. R. Bowler, and A. Michaelides, Journal of Physics: Condensed Matter **22**, 022201 (2009).

[197] G. Henkelman and H. Jónsson, J. Chem. Phys. **113**, 9978 (2000).

[198] H. J?nsson, G. Mills, and K. W. Jacobsen, in *Classical and Quantum Dynamics in Condensed Phase Simulations* (WORLD SCIENTIFIC, 1998) pp. 385–404.

[199] G. Henkelman, G. Jóhannesson, and H. Jónsson, in *Theoretical Methods in Condensed Phase Chemistry*, Vol. 5, edited by S. D. Schwartz (Kluwer Academic Publishers, Dordrecht, 2002) pp. 269–302.

[200] J. Maier, Prog. Solid State Chem. **23**, 171 (1995).

[201] M. W. Swift, J. W. Swift, and Y. Qi, Nat Comput Sci **1**, 212 (2021).

[202] H. J. Monkhorst and J. D. Pack, Phys. Rev. B **13**, 5188 (1976).